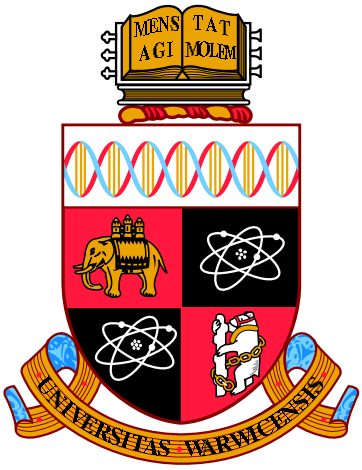

A Bio-mimicking Aeroelastic Energy Harvester

by

Sam W. Tucker Harvey

Thesis

Submitted to the University of Warwick

for the degree of

Doctor of Philosophy

School of Engineering

April 2020

Contents

List of Tables

List of Figures

Acknowledgments

Over the course of my PhD I am grateful to have received support from many amazing people, however foremost I must thank my supervisors Petr and Igor. They have made the PhD experience much greater than anything I had anticipated and helped to develop my thinking with a broadness and rigor which I will carry forward into an academic career. My time at Warwick has been exciting and unique and for much of that I am grateful to them.

I would also like to thank all of my friends and colleagues from the Department of Engineering, especially the Luncheon Society, for making PhD life such an enjoyable experience. I am fortunate to be part of such a supportive group of friends and I am sure that the four years would have been much harder without them.

My parents Louise and Rhodri have been tremendously understanding and supportive throughout the period of my PhD and for that I am hugely grateful. I must also thank my brother Harry, not only for his support, but for the many skatepark sessions that helped me escape my work and find space to think. Life would be much less interesting without riding bicycles and riding together the last few years has been awesome.

I am endlessly grateful for the unwavering support of my partner Bethan, who has helped me through the most difficult and challenging times of my PhD. Her caring nature and boundless love have flattened the road when I thought it impassable.

Declarations

This thesis is submitted to the University of Warwick in support of my application for the degree of Doctor of Philosophy. It has been composed by myself and has not been submitted in any previous application for any degree. The work presented was carried out in full by the author. Parts of this thesis have been published by the author and are detailed in the list of publications.

Publications

The following scientific publications have been published on the basis of the work presented in this thesis

- Tucker Harvey, S., Khovanov I. A. and Denissenko P. (2019). A galloping energy harvester with flow attachment. Applied Physics Letters, 114(10).
- Tucker Harvey, S., Khovanov, I. A., Murai, Y., and Denissenko, P. (2020). Characterisation of aeroelastic harvester efficiency by measuring transient growth of oscillations. Applied Energy, 268(December 2019):115014.

Abstract

The deployment of small autonomous electrical devices is set to revolutionise many industries with applications from wearable devices to structural monitoring of bridges. However, current developments of small autonomous electrical devices are limited by the restrictions of energy storage, such as finite lifespan and environmental impact. Energy harvesters aim to solve this problem by converting energy from readily available ambient sources. The work presented in this thesis relates to the development of an alternative geometry for an aeroelastic energy harvester, which was initially inspired by the trembling of aspen leaves in barely noticeable winds. The geometry, known as the curved-blade, forms oscillations due to the galloping instability, which can be exploited for energy harvesting. The dynamics of a prototype device are investigated resulting in the discovery of two distinct branches of oscillations separated significantly in amplitude. Flow visualisations demonstrate the flow to become attached in the higher amplitude branch, allowing the curved-blade to act similarly to an aerofoil, rather than the bluff bodies which have most commonly been studied. This regime presents the opportunity of improved harvesting efficiencies. To aid in the further investigation of the device, a method is developed which enables the energy harvesting performance to be characterised from the free oscillation transient. The method avoids the implementation and optimisation of a transduction mechanism and could be applied to many other energy generating devices. The method was applied to curved-blades of varying curvatures and the optimal curvature range found to coincide with the range in which the flow becomes attached, illustrating that the attachment of the flow acts to enhance the performance. Additionally, the cyclic formation and shedding of a leading edge vortex was observed, however further work is required to investigate whether these unsteady flow structures are beneficial to performance.

Nomenclature

Nonlinear Dynamics

μ	Bifurcation parameter	
ω	Frequency of oscillator	$\mathrm{rad\,s^{-1}}$
ϕ	Phase of oscillator	rad
A	Amplitude of oscillator	m
T	Oscillation period	s
t	Time	s

General Fluid Dynamics

η	Fluid dynamic viscosity	$\mathrm{Pa\,s}$
$\mathbf{g}$	Gravitation acceleration vector	$\mathrm{m\,s^{-2}}$
$\mathbf{u}$	Flow velocity vector field	$\mathrm{m\,s^{-1}}$
Fr	Froude number	
Re	Reynolds number	
St	Strouhal number	
Ω	Characteristic flow frequency	Hz
ρ	Fluid density	$\mathrm{Kg\,m^{-3}}$
L	Characteristic lengthscale	m
P	Pressure field	Pa
U	Characteristic flow velocity	$\mathrm{m\,s^{-1}}$

U_∞	Freestream flow velocity	$\mathrm{m\,s^{-1}}$

Aerodynamics

α	Angle of attack	rad
Γ_{lev}	Circulation relating to leading edge vortex	$\mathrm{m^2\,s^{-1}}$
Γ_b	Bound circulation around body	$\mathrm{m^2\,s^{-1}}$
Γ_w	Circulation relating to wake vortices	$\mathrm{m^2\,s^{-1}}$
λ^*	Wavelength ratio	
ϕ_{vf}	Phase of vortex forcing	rad
υ	Ratio of aerodynamic to inertial force	
a_i	i_{th} polynomial coefficient of polynomial approximation of C_y	
C_{vf}	Amplitude of vortex forcing	N
C_d	Drag coefficient	
C_l	Lift coefficient	
C_p	Coefficient of performance	
C_y	Aerodynamic force coefficient in y direction	
f_{vf}	Frequency of vortex forcing	Hz
F_n	Aerodynamic force in n direction	N
M_p	Pitching moment	Nm
U^*	Reduced velocity	
U_{tsr}	Tip speed ratio amplitude	
u_{tsr}	Tip speed ratio	

Geometric Parameters

γ	Curved blade half arc angle	rad
Ch	Curved blade chord length	m
A_{swept}	Swept area	$\mathrm{m^2}$

A_f	Curved blade frontal area	m^2
AR	Aspect ratio	
b	Offset between blade centre of mass and end of cantilever	m
D	Cylinder diameter	m
l_b	Cantilever beam length	m
R	Curved blade base circle radius	m
S	Curved blade span	m
t_b	Cantilever beam width	m
th	Curved blade section thickness	m
w_b	Cantilever beam width	m
x_α	Dimensionless offset of flutter rotation axis	

Inertial Properties

I_{ij}	i, j component of inertia matrix	$\mathrm{Kg\,m}^2$
I_p	Aerofoil moment of inertia around point P	$\mathrm{Kg\,m}^2$
m	Mass of tip geometry	Kg
m^*	Mass ratio	
m_{eff}	Effective mass of tip geometry	Kg
m_f	Fixture mass	Kg

Structural

ω_n	Natural frequency	Hz
ζ	Damping ratio	
C_{damp}	Damping coefficient	$\mathrm{N\,s\,m}^{-1}$
d_α	Pitch damping coefficient in flutter	$\mathrm{Nm\,s\,rad}^{-1}$
d_h	Plunge damping coefficient in flutter	$\mathrm{N\,s\,m}^{-1}$
E	Elastic modulus	Pa

I	Second moment of area	m^4
K_α	Pitch stiffness in flutter	$\mathrm{Nm\,rad}^{-1}$
K_{beam}	Effective stiffness of cantilever beam	$\mathrm{N\,m}^{-1}$
K_h	Plunge stiffness in flutter	$\mathrm{N\,m}^{-1}$
Kinematic Variables		
ψ	Maximum slope angle of cantilever beam	rad
A_n	Oscillation amplitude of variable n	
h	Aerofoil height in flutter	m
R_{eff}	Effective radius of rotation of tip geometry	m
x, y, z	Displacement of body centre of mass in i, j, k coordinate system	m
System Energies		
$\eta_{\mathrm{eff\,max}}$	Maximum efficiency of energy transfer	
η_{eff}	Efficiency of energy transfer	
E_{cap}	Energy stored within harvesting circuit capacitor	J
E_{tot}	Total energy of galloping oscillator	J
P_{elec}	Power flow due to electromechanical interaction	W
P_{harv}	Power harvested	W
P_f	Power flow due to fluid structure interaction	W
Electrical		
ϕ_v	Voltage phase difference	rad
θ	Electromechanical coupling coefficient	$\mathrm{N\,W}^{-1}$
C_{piez}	Capacitance of piezoelectric	F
P	Harvested power	W
R_l	Load resistor resistance	Ω
V	Generated voltage across load resistor	V

Other

ϵ	Performance prediction error	W
ω_w	Wavelet frequency	$\mathrm{rad\,s^{-1}}$
f_s	Sampling frequency	Hz

1

Introduction

1.1 An Overview of Energy Harvesting

Energy is a critical commodity in the modern era with global annual consumption surpassing 520 Exajoules in 2018 [18] and projected to increase by around a third by 2040 [17]. As climate change is now one of the greatest challenges faced by the human race, developing clean and renewable energy production has become a vital focus. Yet, at a much smaller scale than large scale energy production, the ability to transform energy in the environment into a useful form has again become a critical and limiting challenge. The growth of autonomous electrical devices and sensors and their application in sensors networks is likely to revolutionise many industries with applications from roadway engineering [84, 40] to wearable devices [93, 77], however current advances are limited by the drawbacks of batteries and other energy storage devices [41]. Energy harvesting technologies aim to provide a solution to this problem by scavenging energy from the environment.

With a broad range of applications, it is likely that no single energy source can be considered as optimal for all cases, but rather the best energy source is application specific. Numerous energy source have been considered including thermal energy [22, 59, 110], solar energy [63, 55], mechanical vibration [99, 94, 36] and fluid flow [106, 42]. Additionally, the combination of different energy sources into a single device has also been shown to be an effective approach, with examples including the combination of fluid flow and mechanical vibration [25, 107] or fluid flow and solar energy [85].

Aeroelastic energy harvesters utilise the dynamic responses of structures subjected

to fluid flow to transform the kinetic energy in the flow into a useful form. These devices can broadly be distinguished by the aerodynamic phenomenon by which they operate, namely the flutter of aerofoils [105], vortex-induced vibrations [82] and the galloping instability of prismatic sections [1]. Figure 1.1 illustrates a comparison of these phenomena. For each phenomenon a typical device is illustrated, which is composed of a body mounted to the end of a cantilever beam and positioned such that the oscillation of the body occurs in a direction perpendicular to the freestream flow direction. In the case of the flutter of aerofoils, the coupling of two or more modes of vibration leads to an instability which can result in the catastrophic growth of oscillations [103]. In its most simple form it can be considered with the coupling of the vertical and rotational displacement of a two-dimensional aerofoil section, commonly known as the plunge and pitch degrees of freedom, as illustrated in Figure 1.1. Vortex-induced vibrations occur when the predominant frequency of unsteady vortex shedding from the body is close to the natural frequency of the structure, resulting in resonant oscillations. The formation of galloping oscillations requires only a single degree of freedom similarly to vortex-induced oscillations and contrary to the flutter of aerofoils. However, with galloping oscillations, the steady aerodynamic forces produce the nonlinearity which causes the formation of self-sustained oscillations, rather than unsteady shedding of vortices.

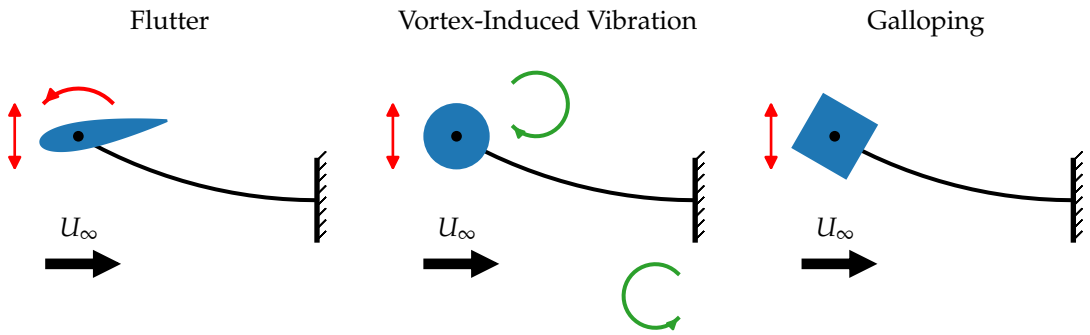

Figure 1.1: Illustration of typical aeroelastic energy harvesting devices. The red arrows illustrate the motion of the bodies, while the freestream flow direction is indicated by U_∞.

As the mechanism by which many aeroelastic energy harvesters operate is through fundamentally nonlinear phenomena we begin with an exploration of nonlinear dynamics. Following this some of the basic aerodynamic concepts which underpin the fluid-structure interaction are introduced. Finally a more detailed overview of each of the aeroelastic phenomenon is presented alongside some more recent advances.

1.2 Limit Cycles and Their Bifurcations

All aeroelastic energy harvesters which are self-excited, meaning that oscillations are maintained without external periodic forcing, rely on the formulation of limit cycles. A limit cycle can be defined as an isolated closed trajectory in the state space. Trajectories close to the limit cycle will either spiral towards or away from the limit cycle depending on whether it is stable, unstable or half-stable [87]. Figure 1.3 demonstrates different types of limit cycle in two-dimensional state space. In the example case the state of the oscillator is entirely defined by the variable y and its time derivative $\dot{y}$ and hence the system is two-dimensional. The red line illustrates the location of the limit cycle, while the black lines demonstrate individual trajectories with the arrows showing the direction of their evolution in time. A single equilibrium position exists at $y = 0$, $\dot{y} = 0$ and is represented by the marker positioned on the origin of the plots. This equilibrium can either be stable or unstable, illustrated by either a filled or unfilled marker respectively. In the case of the stable limit cycle, trajectories outside of the limit cycle are attracted towards it and as they evolve in time will tend to follow its trajectory. Within the limit cycle the equilibrium is unstable and trajectories are pulled outwards while tending towards the limit cycle trajectory. In the unstable case the situation is reversed, with trajectories outside of the limit cycle being pushed further from it as they progress in time, while inside the cycle trajectories tend towards a stable equilibium. Finally a half-stable case can be considered to occur when trajectories within the cycle will evolve away from it over time, while trajectories outside with tend towards it as the evolve.

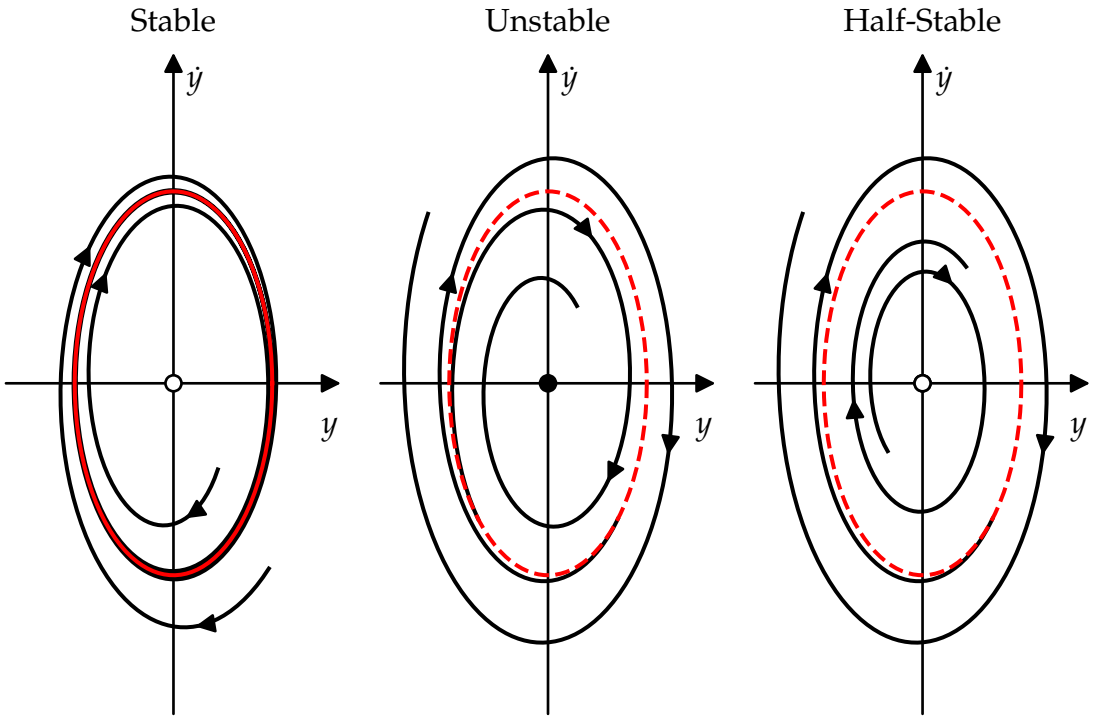

Figure 1.2: Limit cycles with different stabilities in a two-dimensional state space. The red trajectory illustrates the location of the limit cycle with solid lines representing stable cycles, whereas unstable and half-stable limit cycles are shown by dashed lines. Stable and unstable equilibria are illustrated by filled and unfilled circles respectively. The black lines demonstrate the evolution of trajectories with different initial conditions.

The formulation of limit cycles from a stable equilibrium point when a parameter is varied can occur by a Hopf bifurcation [60]. With regard to aeroelastic energy harvesters, this parameter is typically flow velocity, however here we use a general parameter denoted by μ. Hence, when μ is increased beyond a critical point, the stable equilibrium loses stability and periodic oscillations occur. Hopf bifurcations can be either supercritical or subcritical. In the subcritical case the limit cycle exists before the bifurcation and is unstable, whereas in the supercritical case a stable limit cycle forms after the bifurcation. This is illustrated in Figure 1.3.

(*a*) Subcritical Hopf Bifurcation

(*b*) Supercritical Hopf Bifurcation

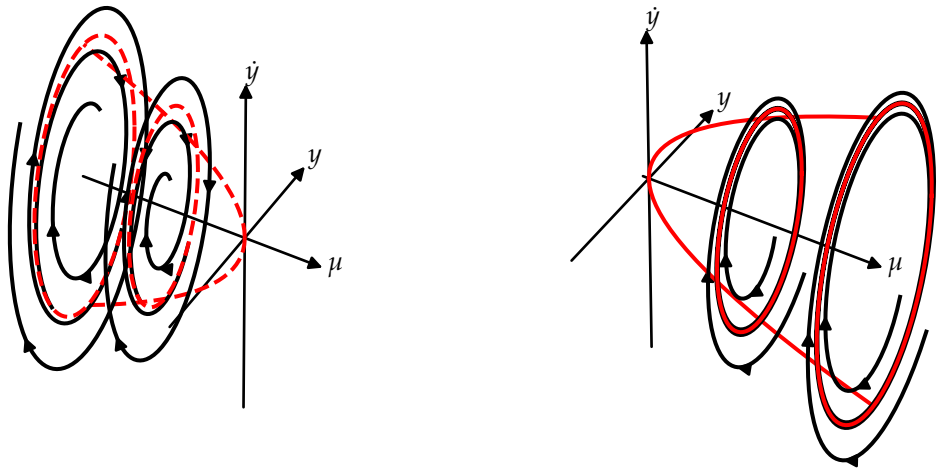

Figure 1.3: Comparison of supercritical and subcritical Hopf Bifurcations. In the subcritical case an unstable limit cycle exists around a stable equilibrium before the bifurcation, which annihilates with the equilibrium at the bifurcation point, in this example at $\mu = 0$. In the supercritical case a stable limit grows from the equilibrium after the bifurcation and exists around an unstable equilibrium.

A further bifurcation which can occur with limit cycles is known as the saddle-node bifurcation of cycles or fold bifurcation [87]. In this bifurcation a pair of limit cycles coalesce and annihilate. In contrast to the Hopf bifurcation, where the oscillation amplitude grows from a small value, in the fold bifurcation the cycle has an amplitude at the point at which annihilation or birth occurs. The bifurcation can be illustrated by an example system represented in phase - amplitude form as

$$\begin{aligned} \dot{A} &= \mu A + A^3 - A^5, \\ \dot{\phi} &= \omega, \end{aligned} \tag{1.1}$$

where A and ϕ denote the amplitude and phase of an oscillator respectively, and ω is the oscillation frequency. Varying the parameter μ results in the occurrence of a saddle-node bifurcation. The relationship between the phase - amplitude representation of the oscillator and its cartesian representation is illustrated in Figure 1.4.

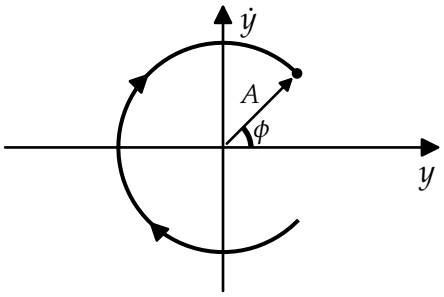

Figure 1.4: Phase - amplitude representation of trajectory in two-dimensional state space.

Figure 1.5 illustrates the saddle-node bifurcation occurring as the parameter μ is increased. Initially, when $\mu = -0.27$, all oscillations decay onto a single stable equilibrium at $r = 0$. Increasing the parameter μ to -0.25 leads to the amplitude potential touching the A axis. This repeated root corresponds to the birth of a half-stable limit cycle at this ampltude. As μ is further increased the half-stable cycle immediately splits into an unstable and stable limit cycle moving in opposite directions along the A axis.

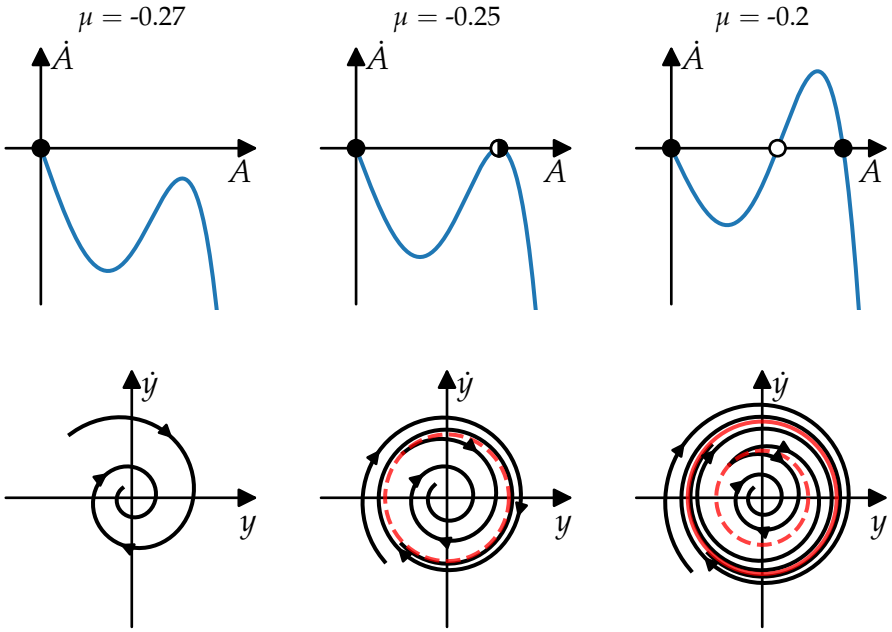

Figure 1.5: Illustration of saddle-node bifurcation of limit cycles. The top row of subplots demonstrates the amplitude potential. Filled, half-filled and empty circles denote stable, half-stable and unstable limit cycles or equilibria respectively. As parameter μ is increased an unstable and stable limit cycle are created at a nonzero amplitude, occurring first as a half-stable cycle with the repeated root in the amplitude potential at $\mu = -0.25$.

1.3 Steady and Unsteady Aerodynamics

The fluid flow around an aeroelastic energy harvester plays a principle role in defining its dynamics and can typically be described by the Navier-Stokes equations. As in the operating regime of the vast majority of flow energy harvesters compressible effects are negligible, the incompressible form of the equations is applicable. The incompressible Navier-Stokes equations are comprised of an expression of mass continuity and momentum conservation and are commonly written as

$$\nabla \cdot \mathbf{u} = 0, \tag{1.2}$$

$$\rho \frac{D\mathbf{u}}{Dt} = -\nabla P + \eta \nabla^2 \mathbf{u} + \rho \mathbf{g}, \tag{1.3}$$

where $\mathbf{u}$ denotes the velocity field, P is the pressure field, ρ defines the fluid density, while η is the dynamic viscosity and $\mathbf{g}$ denotes acceleration due to gravity. As shown in [11], the momentum equation can be represented in dimensionless form by the definition of the dimensionless variables

$$x_i^* = \frac{x_i}{L}, \quad t^* = \Omega t, \quad u_j^* = \frac{u_j}{U}, \quad P^* = \frac{(P - P_\infty)}{\rho U^2}, \quad g_j^* = \frac{g_j}{g}, \tag{1.4}$$

where Ω, L and U denote the characteristic frequency, length-scale and velocity of the flow. This yields

$$St \frac{\partial \mathbf{u}^*}{\partial t} + (\mathbf{u}^* \cdot \nabla^*)\mathbf{u}^* = -\nabla^* P^* + Fr\mathbf{g}^* + Re\nabla^{*2}\mathbf{u}^*, \tag{1.5}$$

where St, Fr and Re are the Strouhal number, Froude number and Reynolds number respectively which can be defined as

$$St = \frac{\Omega L}{U}, \quad Fr = \frac{gl}{U^2}, \quad Re = \frac{\rho U l}{\eta}. \tag{1.6}$$

The Strouhal number describes the importance of unsteady acceleration in the flow. This is of particular importance when the characteristic timescale of the flow is close to a key timescale of the considered system, such as the oscillation period of an aeroelastic energy harvester. The Froude number describes the ratio of the gravitational forces to the flow inertia. For most aeroelastic energy harvesters, no free fluid surface is present and hence the Froude number is not of importance. The Reynolds number is the ratio of the inertial to viscous forces within the fluid and is critical in the onset of turbulence and significance of viscous forces.

When compared to large scale energy production with wind turbines, the scale of

devices aimed at harvesting energy for small electrical devices is much smaller. This results in the devices operating in a low Reynolds number, laminar regime. Figure 1.6 demonstrates the maximum lift coefficient obtained by aerofoils at a wide range of Reynolds numbers, which can broadly be considered as a performance metric for a flow energy harvester. At high Reynolds number, high lift coefficients can be produced as flow remains attached at relatively severe pressure gradients. However, at low Reynolds number where the boundary layer is laminar, the flow separates at lesser adverse pressure gradients and hence smaller angles of attack, limiting the maximum lift coefficient [30]. However, when the flow in unsteady in nature, structures form which allow the aerofoil to generate significantly higher maximum lift coefficients. These structures, which include the leading and trailing edge vortices, have become the topic of a wide level of interest due to their presence in low Reynolds number flapping flight [31, 72]. In this small-scale flight regime, which includes the flight of hovering insects and small birds, the formation of the unsteady leading edge vortex provides a lift enhancement which can make flight possible.

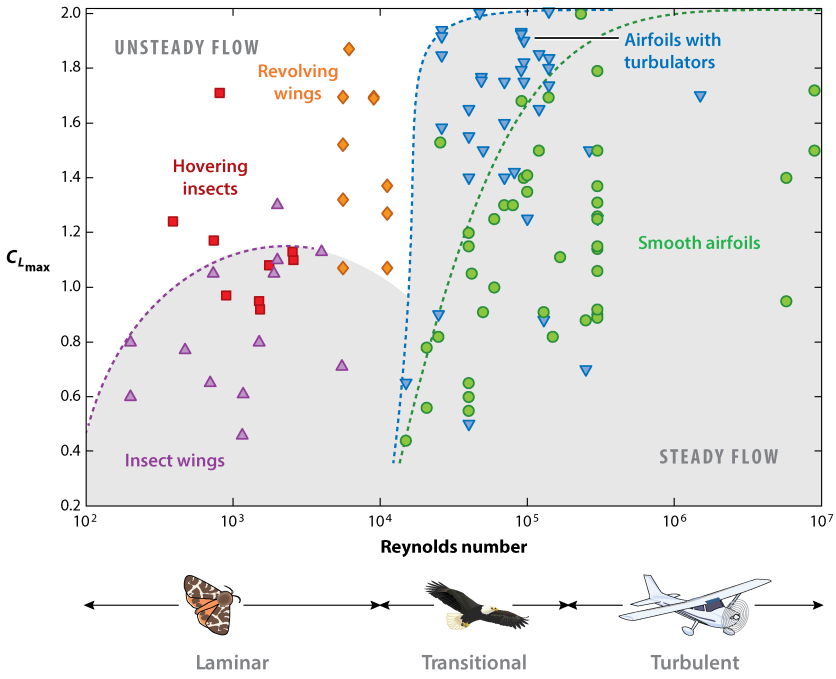

Figure 1.6: Maximum lift coefficient versus Reynolds number [56].

1.4 Flutter of Aerofoil Cross Sections

Although the flutter of aerofoils has long been established as a largely hazardous phenomenon in aerospace [92, 109, 23], its consideration as a means of harvesting energy from

fluid flow is relatively recent. Early developments of flutter in this context include the experimental investigation of Anton et al [9], which yielded a proof of concept energy harvesting device for an unmanned air vehicle and the study of Erturk et al [32], which considered the application of macro-fiber composite piezoceramics (MFC) to a flow-excited morphing aerofoil energy harvester.

Theoertical description of such devices followed only slightly later. Bryant and Garcia [20] proposed a model based on the distributed consideration of a wing mounted to a cantilever beam. The equations in this case were derived by the application of Lagrange's equation to the Euler-Bernoulli bimorph beam. The Rayleigh-Ritz modal summation method was then applied to allow the continuous system to be represented as a systems of ordinary differential equations, while the unsteady aerodynamics were represented by the model of Peters et al [81]. Although considering the distributed nature of the system is likely to provide more accurate modelling results, considerable insight can be gained from simplistic lumped-parameter models. Erturk et al considered the two degree of freedom lumped-parameter wing-section model with piezoelectric coupling to the plunge degree of freedom [33]. The resulting system of equations can be written as

$$\begin{aligned} (m+m_f)\,\ddot{h} + mx_\alpha b\ddot{\alpha} + k_h h - \frac{\theta V}{l} &= -F_l, \\ mx_\alpha b\ddot{h} + I_p\ddot{\alpha} + d_\alpha\dot{\alpha} + k_\alpha\alpha &= M_p, \\ C_{\text{piez}}\dot{V} + \frac{V}{R_l} + \theta\dot{h} &= 0. \end{aligned} \tag{1.7}$$

The first two equations describe the dynamics of the pitch and plunge degrees of freedom where the pitch and plunge displacements are denoted by α and h respectively, while the third equation describes the harvesting circuit and V represents the voltage generated in the piezoelectric element. The airfoil mass per length is denoted by m, while m_f accounts for the fixture mass per length and I_p is the moment of inertia per length about point P. The semichord length is represented by b and x_α is the dimensionless offset of the rotational axes at point P to the centroid at point C, which can be seen to define the inertial coupling between the first two equations. The stiffness in the pitch and plunge degrees of freedom are denoted by k_α and k_h respectively and their structural damping coefficients are represented by d_h and d_α. Figure 1.7 demonstrates the two degree of freedom aerofoil system described by the model.

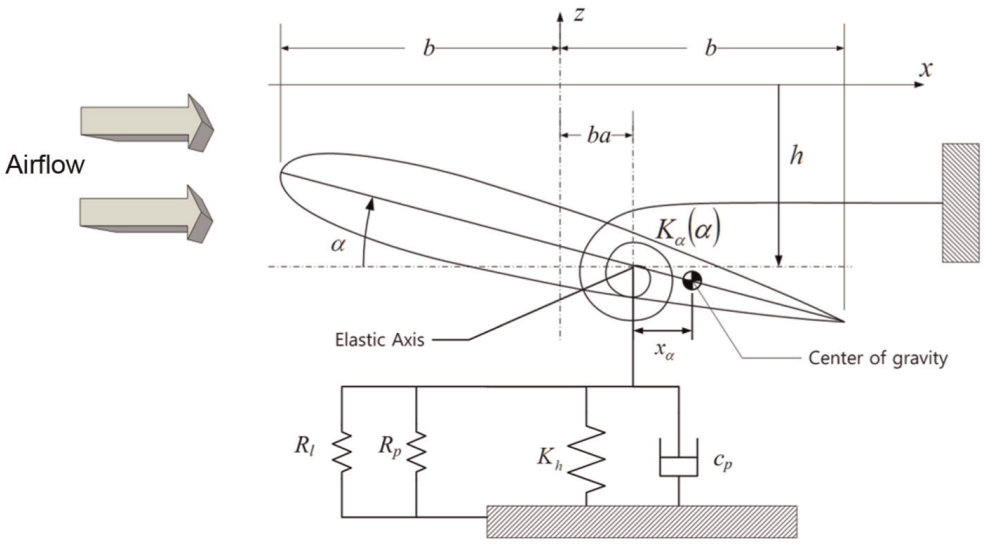

Figure 1.7: Typical construction of flutter based energy harvester [12].

In the third equation, R_l is the load resistance and C_{piez} is the equivalent capacitance of the piezoceramic layers, while θ denotes the electromechanical coupling coefficient. The external aerodynamic forces and moments are presented on the right hand side of the first and second equation with F_l representing the lift force and M_p the pitching moment. Theodorsen's unsteady thin airfoil theory [91] was applied to represent the aerodynamic terms. The model was demonstrated by experimental validation to be an accurate representation of a prototype device in the regime close to the flutter boundary and an optimal load resistance for maximising the output power identified.

The stiffness in both the pitch and plunge degrees of freedom, as well as their respective mechanical damping terms can be seen to be linear in nature. Furthermore, with Theodorsen's linear approximation of the unsteady aerodynamic terms, all remaining terms in the system are linear and hence the aeroelastic responses are limited to convergence to a stable equilibrium below the flutter speed, unbounded growth of oscillation amplitude above the flutter speed and neutrally stable oscillations at the flutter speed [12]. The inability of these linear models to form limit cycles restricts their application to energy harvesting. One solution to this is the introduction of structural nonlinearity.

The influence of introducing additional structural nonlinearity to the linear aerofoil flutter model has also been the subject of numerous studies, including that of Bae and Inman [12]. Their study utilised the lumped-parameter model in the form of Equation

1.7, with either cubic hardening or free-play nonlinearity applied to the pitch degree of freedom. The free-play nonlinearity was found to allow the formation of stable limit cycle oscillations below the flutter speed, while cubic hardening caused them to occur at flow velocities greater than it. These limit cycle oscillations provided the opportunity to assess the energy harvesting capability.

Further to the addition of structural nonlinearity, by consideration of the nonlinear aerodynamic effect due to aerofoil stall, which occurs as the oscillation amplitude becomes large, limit cycles can form. This was demonstrated by Abdelkefi et al [4, 3] with the application of a quasistatic nonlinear representation of the lift force and pitching moment. The occurrence of both subcritical and supercritical Hopf bifurcations were demonstrated, while parameters were chosen to avoid the subcritical case due to its sudden growth in amplitude. Furthermore, a secondary supercritical Hopf bifurcation was found to exist, resulting in the prospect of quasiperiodic and chaotic motion. These complex responses were found to lead to a drop in harvested power.

1.5 Vortex-Induced Vibrations

Vortex-induced vibrations have long been investigated as a phenomenon in fluid dynamics due to their numerous appearances in practical engineering problems [101]. When the wake of a structure becomes unstable, it can result in the shedding of vortices and a consequent unsteady forcing on the structure. If the dominant frequency of the forcing is close to the natural frequency of the structure, resonant oscillations can occur. The wake mode is critical in determining the unsteady forces generated on the structure and hence the dynamics of its oscillation.

By driving the oscillation amplitude and frequency of a circular cylinder with a computer controlled system in a tow tank, Williamson and Roshko [102] assembled a map of the regimes of different wake modes as illustrated in Figure 1.8. The map is presented in terms of amplitude ratio and wavelength ratio, which are defined as $A^* = \frac{A}{D}$ and $\lambda^* = \frac{U_\infty T}{D}$ respectively, where A denotes the displacement amplitude of the cylinder, D is the cylinder diameter, U_∞ denotes the freestream flow velocity and T is the oscillation time period. The different types of wake modes are denoted by '2S', which represents two single vortices shed per oscillation cycle of the cylinder, '2P', which defines a mode in which 2 pairs of counter-rotating vorticies are shed per cycle and 'P+S' which denotes a mode in which a pair vortices and a single vortex are shed per cycle. In the case of low mass ratios, when the mass of displaced water is significant relative to the mass of the structure, the highest amplitude branch of free oscillations corresponds to a '2P' wake mode.

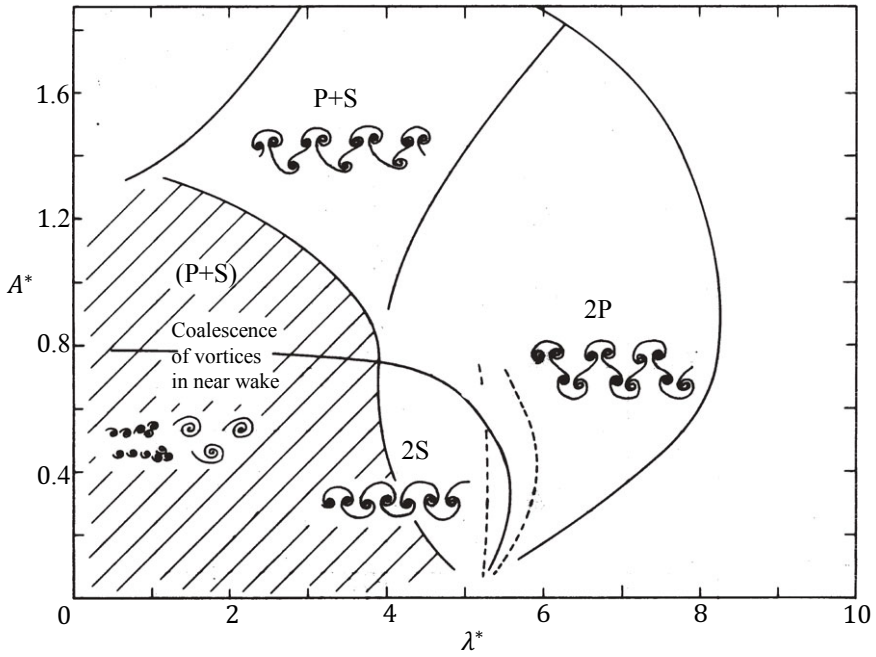

Figure 1.8: Map of vortex shedding regimes [102]. $\lambda^* = \frac{U_\infty T}{D}$ denotes the wavelength ratio, where U_∞ is the freestream flow velocity, T is the oscillation period and D is the cylinder diameter. $A^* = \frac{A}{D}$ represents the amplitude ratio, where A is the oscillation amplitude. '2S' represents a mode in which two single vortices are shed per oscillation cycle of opposite vorticity, '2P' defines a mode in which 2 pairs of counter-rotating vorticies are shed per cycle and 'P+S' denotes a mode in which a pair vortices and a single vortex are shed per cycle.

An early mathematical investigation of the prospects of harvesting energy from the vortex-induced vibration of a circular cylinder was made by Barrero-Gil et al [14]. The dynamics of the vibrating structure were described by a single degree of freedom mechanical oscillator, while the aerodynamic forcing was represented by a time dependent sinusoidal forcing term. The system could hence be described by the second-order ordinary differential equation

$$m(\ddot{y} + 2\zeta\omega_n\dot{y} + \omega_n^2 y) = \frac{1}{2}\rho U_\infty^2 D C_{\mathrm{vf}} \sin(2\pi f_{\mathrm{vf}} t + \phi_{\mathrm{vf}}), \tag{1.8}$$

where y denotes the displacement of the cylinder, ζ is the damping ratio per unit length, m is the cylinder mass per unit length and ω_n represents the natural frequency. In the term on the right hand side, which describes the periodic forcing due to the shedding of vortices into the wake, U_∞ denotes the freestream flow velocity, D is the cylinder diameter and C_{vf} defines the amplitude of the vortex forcing, while f_{vf} and ϕ_{vf} represent its frequency and phase. With the use of experimentally measured values for $C_{\mathrm{vf}} \sin\phi_{\mathrm{vf}}$ and $C_{\mathrm{vf}} \cos\phi_{\mathrm{vf}}$

taken from Hover et al [47] and with the assumption of steady-state harmonic oscillations with the shedding frequency and oscillation frequency equal, the effects of the mass ratio, mechanical damping coefficient and Reynolds number on the efficiency of dissipation of fluid energy were evaluated. The analysis demonstrated the existence of an optimal mass-damping parameter for energy harvesting, defined as the product of the mass ratio and damping ratio, where the mass ratio is the ratio of the body density to the fluid density. The mass ratio was also shown to be the most important parameter in the region of reduced velocities close to the peak efficiency.

The mathematical approach developed by Barrero-Gil assumed the frequency of the vortex shedding to be equal to that of the oscillation of the structure. In reality, this locked-in state cannot be obtained at all reduced velocities but only within a range where the natural frequency of the structure and shedding frequency are close. The broadness of this region forms a critical aspect of the design of energy harvesters based on the vortex-induced vibrations as it essentially defines the range of flow velocities in which the device will operate efficiently. A method by which this region can be expanded is by the introduction of nonlinearity into the restoring force. Mackowiski and Williamson [67] investigated the effect of introducing such nonlinearities with a Cyber-Physical Fluid Dynamics approach. The approach involved the augmentation of the restoring force of an experimental structure submerged in a tow tank by computer control, hence allowing the application of arbitrary restoring forces to the submerged body. The results demonstrated that quintic and cubic hardening nonlinearity could significantly widen the range over which a device could operate efficiently, with only a relatively small cost to the peak efficiency.

Nonlinearity in the restoring force can also result in bistability and chaos if it is of the correct form, as has been demonstrated by the simulations of Huynh and Tjahjowidodo [50]. In their work the dynamics of the unsteady wake was represented by an additional wake oscillator equation, rather than the sinusoidal time dependent forcing utilised by Barrero-Gil et al, while the oscillator was again represented as a single degree of freedom mechanical oscillator. This form of the model was developed by Facchinetti et al [35] and modified by Farshidianfar and Dolatabadi [37] and has been shown to provide close correspondence to experimental results. The simulations demonstrated that a bistable restoring force potential was capable of improving power output at low reduced velocities, while chaotic responses were found to relate to worsened performance.

1.6 Galloping of Prismatic Structures

The observation and study of galloping oscillations has a long history [21, 76, 80, 71], although similarly to the flutter of aerofoils, it was considered as a phenomenon to be

avoided in most engineering applications, until its analysis with respect to energy harvesting more recently. Consideration of the instability in relation to the oscillation of transmission lines led Den Hartog to formulate the stability criterion for a galloping oscillator, which is now known as the Den Hartog criterion [27] and can be written as

$$\frac{dF_l}{d\alpha} + F_d < 0, \tag{1.9}$$

where F_l and F_d denote the lift and drag force respectively and α is the angle of attack. The criterion is derived by consideration of the flow velocity and aerodynamic force vectors of a galloping body, which are illustrated in Figure 1.9.

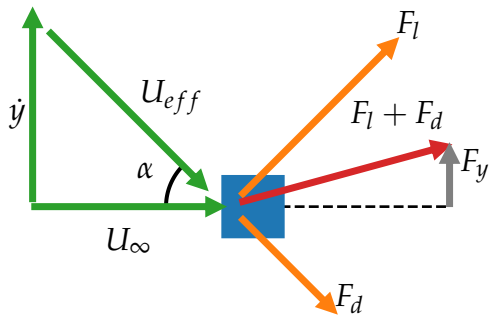

Figure 1.9: Velocity vectors and forces acting on a galloping body. The freestream flow velocity is denoted by U_∞, $\dot{y}$ is the linear velocity of the body and U_{eff} is the subsequent effective flow velocity. The lift force and drag force are represented by F_l and F_d respectively, while the aerodynamic force projected in the y direction is denoted by F_y.

The theoretical description was later developed significantly by Parkinson and Smith with respect to the galloping square-prism [79]. The critical aerodynamic force in the galloping instability is the force in the direction of motion of the body, which is represented by F_y in Figure 1.9. This force can be represented as the projection of the lift and drag forces by

$$F_y = F_l \cos(\alpha) - F_d \sin(\alpha), \tag{1.10}$$

where α is the angle of attack, F_l is the lift force and F_d is the drag force. The force F_y can be non-dimensionalised by

$$C_y = F_y \frac{2}{\rho A_f \left(U_\infty^2 + \dot{y}^2\right)}. \tag{1.11}$$

An early consideration of galloping as a mechanism for harvesting wind energy was made by Barrero-Gill, Alonso and Sanz-Andres [13]. They formulated a lumped-parameter model by applying an additional aerodynamic force to a linear mechanical oscillator

$$m(\ddot{y} + 2\zeta\omega_n\dot{y} + \omega_n^2 y) = F_y = \frac{1}{2}\rho U_\infty^2 D C_y, \tag{1.12}$$

$$C_y = a_1 \frac{\dot{y}}{U} + a_3 \left(\frac{\dot{y}}{U}\right)^3, \tag{1.13}$$

where y denotes the vertical displacement, ζ represents the damping ratio per unit length and ω_n denotes the natural frequency. The aerodynamic force per unit length in the y direction is represented by F_y, while D is the characteristic dimension of the galloping body and m is the body mass per unit length. The aerodynamics were considered as quasistatic and hence the aerodynamic force coefficient C_y was represented by a cubic polynomial with coefficients a_1 and a_3 as presenting in Equation 1.13. In contrast to later investigations, a specific transduction method was not considered, but rather energy harvesting considered as additional damping. By the assumption of weakly nonlinear behaviour, an approximate analytical solution was formulated with the Krylov-Bogoliuvov method [73]. The efficiency of energy transfer from the fluid was defined as the ratio of the available power in the fluid to the extracted power

$$\eta_{\text{eff}} = \frac{P_f}{P_{\text{f,tot}}}, \tag{1.14}$$

where P_f denotes the power transfered from the fluid to the body and P_f is the total power available in the fluid, estimated by $P_{\text{f,tot}} = \rho\frac{U_\infty^3 D}{2}$. The power transfered from the fluid to the body could be evaluated as

$$P_f = \frac{1}{T}\int_0^T F_y \dot{y} dt, \tag{1.15}$$

where T is the oscillation time period. Evaluating the efficiency of energy transfer with the approximate analytical solution then provided the expression

$$\eta_{\text{eff}} = 2a_1\left(\frac{4m^* - a_1 U^*}{3a_3 U^*}\right) + 6a_3\left(\frac{4m^*\zeta - a_1 U^*}{3a_3 U^*}\right)^2, \quad \eta_{\text{eff max}} = -\frac{a_1^2}{6a_3}, \tag{1.16}$$

where m^* is the mass ratio and U^* is the reduced velocity. $\eta_{\text{eff max}}$ denotes the maximum

efficiency found by differentiating the efficiency η_{eff} with respect to reduced velocity and setting to zero. The result demonstrates that in the case of a weakly nonlinear galloping energy harvester with quasistatic aerodynamics represented by a cubic polynomial, the maximum efficiency is only dependent on the cross-section geometry and is independent of the mass and mechanical parameters. The efficiency was evaluated using experimentally determined values of the coefficients a_1 and a_3 taken from [79, 8, 75, 65]. It was found that the D-section geometry provided greater efficiencies than both the square-prism and isosceles triangular geometries.

The transduction mechanism forms a key part of a galloping energy harvester with electromagnetic induction and the piezoelectric effect forming the two most widely considered mechanisms of operation. Abdelkefi, Hajj and Nayfeh [2] evaluated the energy harvesting capability of a galloping energy harvester with the same quasistatic aerodynamic approximation as Barrero-Gill et al with a lumped-parameter model, however rather than representing the harvesting of energy as additional damping, a further ordinary differential equation representing a piezoelectric harvesting circuit was coupled to the equation representing the galloping oscillator. Similarly to the lumped-parameter modelling of flutter based piezoelectric energy harvesters in Equation 1.7, the harvesting circuit consists of a piezoelectric element which is modelled as a voltage source in parallel with a capacitor. To dissipate electrical energy, a load resistor is added in parallel with the piezoelectric element. This resulted in the system of equations

$$\begin{aligned} m(\ddot{y} + 2\zeta\omega_n\dot{y} + \omega_n^2 y) - \frac{\theta}{l}V = F_y = \frac{1}{2}\rho U^2 D C_y, \\ C_p\dot{V} + \frac{V}{R} + \theta\dot{y} = 0, \end{aligned} \tag{1.17}$$

where C_p denotes the capacitance of the piezoelectric element and V is the voltage generated across it, while θ defines the electromechanical coupling and R is the load resistance. The load resistance was found to significantly influence both the onset flow velocity of galloping oscillations and the harvested power, with varying optimal values existing at different flow velocities. Performing the same comparison of tip geometries as Barrero-Gill et al with identical values for the polynomial coefficient a_1 and a_3, the isosceles trangular geometry was found to perform best at low flow velocities, while the D-section produced the most power at higher flow velocities.

Although the quasistatic representation of the aerodynamic force coefficient C_y with a cubic nonlinearity provides a simplistic representation of the galloping phenomenon and allows approximate analytical solutions to be formulated [90], as illustrated by Javed and Abdelkefi [54], it is not always sufficient to accurately represent the dynamics. By fitting experimental data for the aerodynamic coefficient C_y for the square-prism from Parkinson

and Smith [79] with different orders of polynomial, Javad and Abdelkfi demonstrated the order of polynomial selected can significantly impact the type of instability as well as the existence of hysteresis regions.

The modelling considerations of galloping oscillators and energy harvesters which have been presented are all reliant on a quasistatic representation of the aerodynamic behaviour of the body, where the aerodynamic force coefficients are dependent only on the effective angle of attack and not on time. This approximation is valid when the timescale of the oscillation is much greater than the timescale of the unsteady flow structures, however the galloping behaviour can change significantly when this condition is not met and the timescales become close. An example of unsteady aerodynamic effects interfering with the galloping response can be seen in the experimental observations of Mannini et al [68] with a galloping rectangular prism. In their experiments, by varying the mechanical damping, the onset flow velocity of galloping oscillations was moved progressively closer to the flow velocity at which the vortex shedding frequency would be equal to the natural frequency of the structure. Once these velocities became close enough, a branch of high amplitude oscillations appeared to grow from a reduced velocity of $\frac{1}{St}$. The ability of the interference between the unsteady phenomenon of vortex-induced vibrations and the galloping instability provides the opportunity to harvest energy at considerably lower flow velocities. Further experimental investigations in the context of energy harvesting have shown the interference not only to allow energy to be harvested at lower flow velocities, but also to provide a performance enhancement [44, 88].

1.7 Biomimetic Design

The objective of biomimetic design is to find inspiration in biological phenomenon and apply it to developing engineering solutions. This design approach has been utilised in a vast range of applications, from reducing the fluid drag of swimsuits by learning from shark skin dentiles [78, 100], to creating the next generation of autonomous flying robots [28, 53]. Biomimetic design has also been considered in the context of energy harvesting. Wu et al investigated the power extraction performance of a biomimetic energy harvester inspired by flapping flight in ground effect [104]. The proximity of the ground was found to improve the performance of a simulated device by up to 28.6 %. Considering another energy source and inspired by the gently swaying of kelp in waves, Wang et al developed a bio-inspired triboelectric nanogenerator for the harvesting wave energy [98]. The device was found to operate effectively at frequencies as low as 1 Hz.

Biomimetic design can largely be considered as a bidirectional process, with the direction depending on the starting point. If the process begins with an observation of

a biological process and then proceeds to an application to an engineering problem, the process is known as 'solution driven'. In the opposing direction, an engineering problem is first identified and then the biological world searched for analogical model. This is known as a 'problem driven' approach [46].

1.8 The Trembling Aspen Leaf

The geometry for the galloping energy harvester investigated in this thesis was initially inspired by the trembling of Aspen leaves in barely noticeable winds and hence is an example of a solution driven biomimetic design. Wind induced motion of leaves has been linked to numerous, and often beneficial, biological consequences for plants [26, 89]. Initial considerations of exploiting the wind induced motions of Aspen leaves for harvesting energy were made by experiments conducted by University of Warwick masters students [29, 70, 39, 43]. Eckersley-Carr investigated a curved plate geometry with a thin 'stalk', which was demonstrated to be capable of producing $4\,\mu W$ at a flow velocity of $10\,m\,s^{-1}$ with the use of a piezoelectric element attached to the stalk. Later experiments by Gaskell illustrated the same curved geometry but with a electromagnetic energy extraction mechanism [39], observed to produce 39 mW. Investigations were also made into the interaction of individual devices, such as the ability for their oscillations to become synchronised in a laboratory flume [70] or a wind tunnel [43]. The geometries explored in these initial studies paved the way for the development of the more rigorously defined two-dimensional geometry investigated in this thesis.

1.9 Research Objectives and Thesis Outline

The work presented in this thesis relates to the development of an alternative geometry for a galloping energy harvester, which was initially inspired by the trembling of Aspen leaves in barely noticeable winds. The research objectives can be stated as:

- Develop the understanding of the underlying mechanism by which galloping curved-blade energy harvesters operate
- Optimise the geometric parameters of the curved-blade geometry for the purpose of energy harvesting

Chapter 2 considers the first of these objectives with an examination of the dynamics of the galloping curved-blade by means of both wind tunnel experiment and mathematical modelling. The underlying fluid phenomena are investigated by flow visualisation and hot

wire velocimetry yielding insights into the physical mechanisms at play. For the geometric parameters of the curved-blade to be optimised experimentally for the fulfillment of the second research objective, an approach for characterising the performances of different geometries was required. The development and numerical verification of this method are presented in chapter 3. Finally, chapter 4 details an experimental investigation of the influence of the geometric parameters on the harvesting performance.

2

A Galloping Curved-Blade Energy Harvester

2.1 Introduction

In the case of most galloping energy harvesters, the aerodynamic forces, which allow limit cycle oscillations to form, are largely developed around the tip geometry. The flow field around the tip geometry hence fundamentally determines the potential efficiency of a device. Many geometries have been studied with focus being placed on the square, isosceles-triangular and the D-shaped cross sections [108, 5, 16, 48]. Studies of these geometries have shown the mechanism by which oscillations form to relate to highly separated flows around the tip geometry. The flow around a galloping square cross section has been examined by both numerical and experimental means [66]. The mechanism by which galloping oscillations are formed has been shown to relate to the separation and reattachment of the flow on the sides of the square-section, while the flow on the rear face remains detached [66]. Similarly, in the case of the isosceles-triangular cross section, the boundary layer has been demonstrated to be detached on at least one face depending on the angle of attack [96, 83]. The flow around a D-shaped cross section has been studied numerically with regard to semicircular aerofoils and also shown to be detached at low angles of attack [51, 52]. Hence, the mechanisms for galloping oscillations for the square, isosceles-triangular and D-shaped sections have been shown to relate to detached flows.

In this chapter, the curved-blade geometry, which was initially inspired by the trembling of Aspen leaves, is presented and investigated in the context of galloping energy harvesters. The curved-blade differs from the bluff bodies which have typically been studied in that it is closer to an aerofoil and hence provides the prospect of attached flows. To evaluate the prospect of an energy harvesting device based on this geometry, its dynamics are first evaluated. A galloping oscillator with a curved-blade tip geometry is mounted into a low speed wind tunnel and its dynamics tracked. The resulting measurements are compared to simulations obtained with a simplistic lumped-parameter mathematical model. To provide an insight into the underlying fluid phenomena which govern the formation of oscillations, flow visualisation and particle image velocimetry (PIV) are applied, as well as hot-wire velocimetry. The energy harvesting performance is then evaluated by simulations of the lumped-parameter model and results compared with the square-prism geometry as a comparator.

The galloping system and wind tunnel experimental setup are first described in Section 2.2. Following this the experimental investigation of the harvester dynamics is presented in Section 2.3, alongside the mathematical modelling and the experimental determination of model parameters. The flow visualisations are presented and interpreted in Section 2.4, while Section 2.5 illustrates the methodology in which hot-wire velocimetry was applied and the subsequent results obtained. Finally, the potential energy harvesting performance of the curved-blade is evaluated in Section 2.6 and compared to that of the square-prism geometry.

2.2 System Description

The harvester consisted of a cantilever beam and a curved-blade. The section of the curved-blade was chosen to be a circular arc, while the cantilever beam was of steel construction. The blade was rigidly mounted to the end of the beam and the beam fixed with a clamp. The constructed system is demonstrated in Figure 2.1, while further details of the system parameters are presented in Table 2.1. For the purpose of experimentally investigating the dynamics of the device, the system was assembled within a low speed wind tunnel such that the blade was oriented perpendicular to the free-stream flow direction. The wind tunnel had a test section of $1.04 \times 1.37\,\mathrm{m}$ with a turbulence intensity of less than $1\,\%$ and was capable of obtaining stable flow velocities between $0.5\,\mathrm{m\,s^{-1}}$ and $24\,\mathrm{m\,s^{-1}}$. An illustration of the experimental setup within the wind tunnel test section is illustrated in Figure 2.2. The observed oscillations relate to the motion of the blade in a plane normal to the flow direction as illustrated in Figure 2.1. Oscillations were experimentally observed with flow velocities ranging from $0.9\,\mathrm{m\,s^{-1}}$ to $5.8\,\mathrm{m\,s^{-1}}$ corresponding to Reynolds numbers of 6.2×10^3 and

4.0×10^4.

Parameter	Symbol	Value (unit)
Blade Base Circle Radius	R	75 (mm)
Blade Half Arc Angle	γ	45°
Blade Chord Length	Ch	75 (mm)
Blade Thickness	th	7.5 (mm)
Blade Span	S	75 (mm)
Beam Length	l_b	150 (mm)
Beam Width	w_b	12.5 (mm)
Beam Thickness	t_b	0.5 (mm)

Table 2.1: Parameters of experimental galloping oscillator

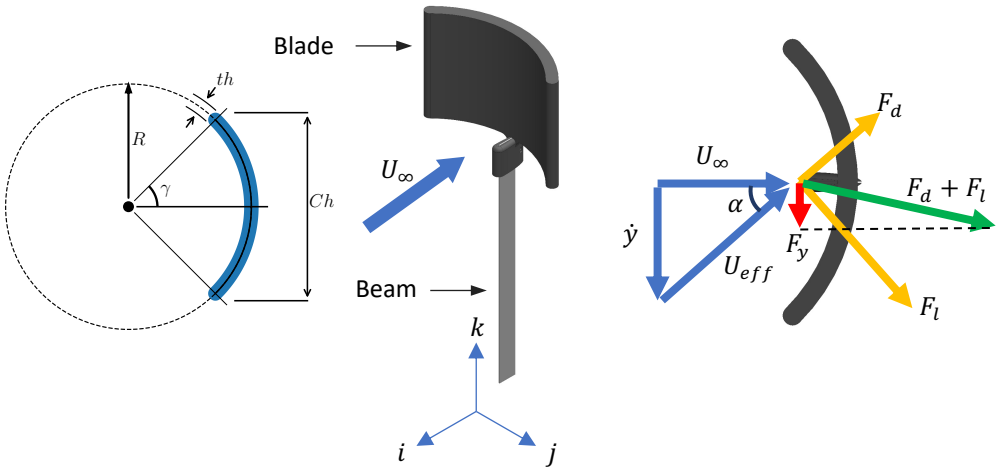

Figure 2.1: Illustration of geometry and definition of variables. Oscillations result in motion in j, k plane. U_∞ denotes the freestream flow velocity, $\dot{y}$ is the linear velocity of the blade centre of mass, U_{eff} is the effective flow velocity and α is the effective angle of attack. F_l and F_d denote the lift and drag forces, while F_y is the aerodynamic force in the j direction.

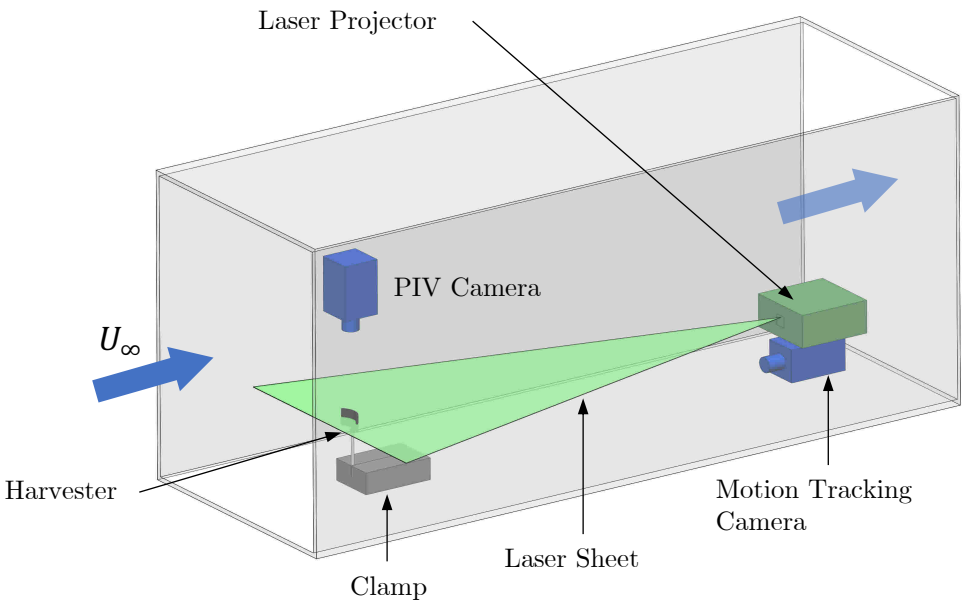

Figure 2.2: Illustration of low speed wind tunnel experimental setup.

2.3 Harvester Dynamics

2.3.1 Motion Tracking of Harvester Dynamics

The dynamics of the harvester were captured with a 2D motion tracking system implemented with a 1920×1080 pixel resolution camera with a frame rate of 50 fps. The position of the motion tracking camera within the test section is demonstrated in Figure 2.2. Three fluorescent markers were tracked by the system, the first of which was positioned at the fixed end of the cantilever beam and acted as a datum. The second marker was attached to the free end of the cantilever beam, while the final marker was painted onto the rear surface of the curved-blade. The images acquired by the camera were processed by a global binary threshold and the centroids of the subsequent connected regions evaluated, providing the centroids of the markers. The positions of the markers as viewed by the motion tracking camera are demonstrated in Figure 2.3.

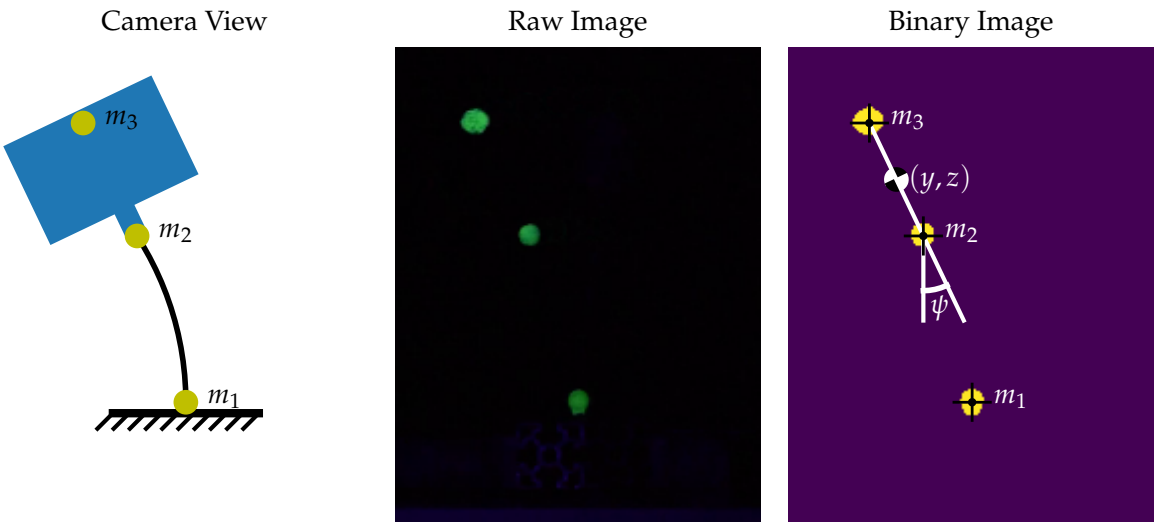

Figure 2.3: Illustration of motion tracking process. m_1, m_2 and m_3 demonstrate the locations of the motion tracking markers. y and z represent the location of the blade centre of mass along the j and k axes respectively.

The dynamics of the system could be described by the displacement of the blade centre of mass along the j axis in Figure 2.1. The centre of mass position was determined by interpolating between the locations of the second and third markers, while the angle between the line formed by these markers and the vertical, which represents the orientation of the blade, was used to evaluate the maximum slope angle of the beam ψ. The precision of the system was estimated as 0.24 mm or 2.2×10^{-4} Ch when evaluated over a one minute time series. Flow velocity was measured within the tunnel with the use of a pitot tube connected to a Furness Controls FC0560 digitial manometer. The manometer was sampled at 100 Hz with an estimated uncertainty of $0.012\,\mathrm{m\,s^{-1}}$.

During an experimental run the galloping oscillator started in a resting position while the freestream flow velocity was incrementally increased. After each incremental increase in flow velocity the galloping oscillator was given a 5 minute time period to reach steady-state behaviour. Following this relaxation period, the position of the blade was motion tracked for a further 5 minutes. Once the maximum freestream flow velocity in the test range was obtained, the procedure was repeated in reverse, incrementally decreasing the flow velocity back down. This allowed the observation of hysteresis in the dynamics. This experimental procedure is illustrated in Figure 2.4.

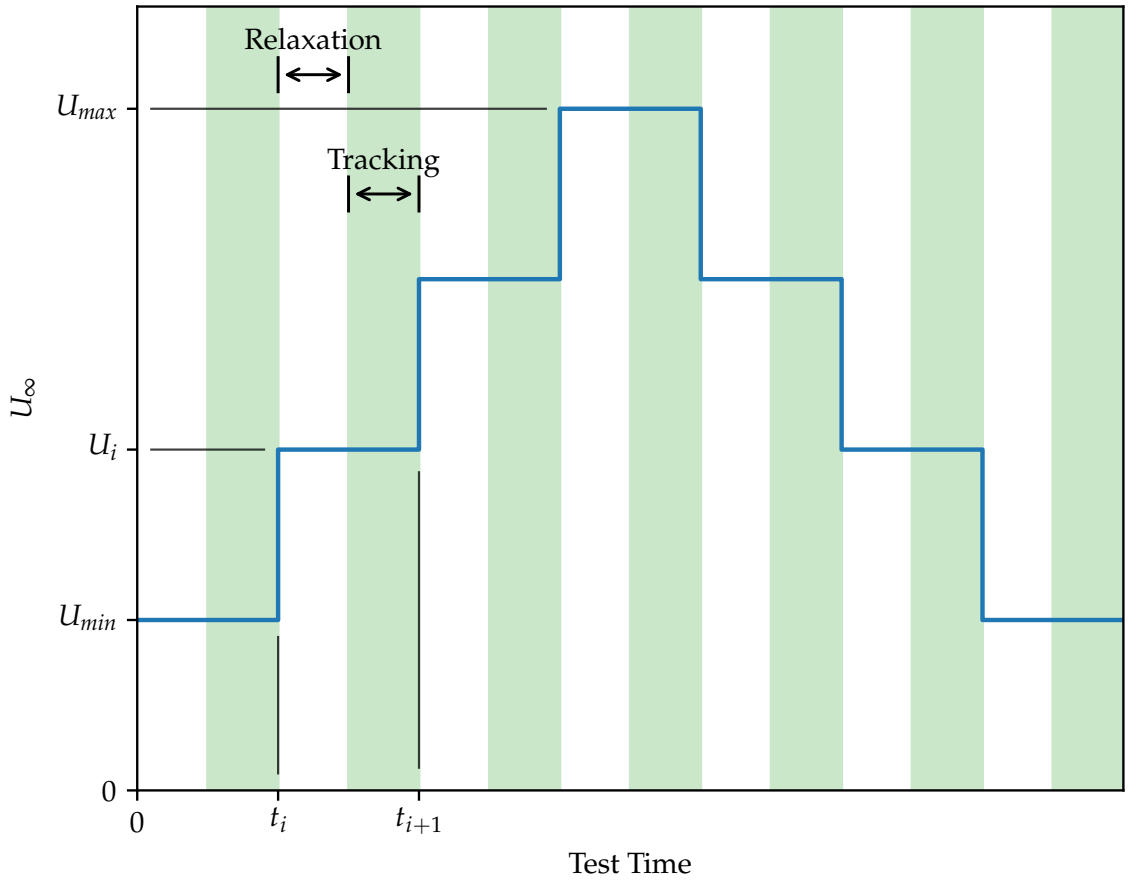

Figure 2.4: Illustration of motion tracking methodology. $U_{\min}$, $U_{\max}$ denote the minimum and maximum freestream flow velocities obtained during an experiment respectively, while t_i is the start time of the i_{th} test and U_i denotes the flow velocity during the i_{th} test.

2.3.2 Mathematical Modelling

Simplistic modelling approaches with single degree of freedom lumped-parameter models have been shown to be relatively effective in describing the dynamics of galloping energy harvesters [24] and can provide insight into the underlying physical mechanisms which govern their dynamics. Similarly to Barreo-Gil [13], by considering small deflections of the beam, the position of the system can be reduced to a linear displacement in the y direction. However, as the rotation of the blade around k axis in Figure 2.1 is significant, its influence should be incorporated. By assuming the beam acts as a cantilever with end load and moment under small deflections, a one-to-one relationship between the y displacement and maximum slope angle ψ can be derived and used to form an effective mass, denoted by m_{eff}. The system can hence be described by the second-order ordinary differential equation

$$\ddot{y} = \frac{1}{m_{\text{eff}}} \left(F_y(\dot{y}) - K_{\text{beam}} y - C_{\text{damp}} \dot{y} \right), \tag{2.1}$$

where

$$m_{\text{eff}} = m + \frac{I_{xx}}{R_{\text{eff}}^2}. \tag{2.2}$$

Here I_{xx} denotes the moment of inertia of the blade around an axis parallel to the i axis and running through its centre of mass and R_{eff} is the effective radius of rotation. m, K_{beam} and C_{damp} denote the tip mass, beam stiffness and damping coefficient respectively.

By linear superposition, the deflection y and maximum slope angle ψ of a cantilever beam with an end load denoted by F which is offset by a distance b from the beam end, resulting in an external moment Fb, can be written as

$$y = F\left(\frac{l_b^3}{3EI} + \frac{b l_b^2}{2EI} \right), \quad \psi = F\left(\frac{l_b^2}{2EI} + \frac{b l_b}{EI} \right), \tag{2.3}$$

where E is the elastic modulus of the beam material, I denotes the second moment of area of the beam cross section and l_b is the beam length. Combining the equations provides a relationship between y and ψ and an expression for the effective radius

$$\psi = \frac{3(l_b + 2b)}{l_b(2l_b + b)} y, \quad R_{\text{eff}} = \frac{l_b(2l_b + b)}{3(l_b + 2b)}. \tag{2.4}$$

The aerodynamic force F_y could be represented as a function of the non-dimensional force coefficient C_y by

$$F_y = \frac{1}{2} \rho A_f C_y(\alpha) \left(U_\infty^2 + \dot{y}^2 \right), \tag{2.5}$$

where ρ is the density of air and U_∞ is the flow velocity. The aerodynamic force coefficient C_y can be written in terms of the lift and drag coefficients, C_l and C_d, as

$$C_y = C_l \cos(\alpha) - C_d \sin(\alpha), \tag{2.6}$$

where α is the effective angle of attack of the blade, which is given by $\alpha = \arctan(\dot{y}/U_\infty)$, as illustrated in Figure 2.1. Under the assumption of quasistatic aerodynamics, where unsteady and transient aerodynamic effects occur at timescales much shorter than that of the oscillation period, the aerodynamic force coefficient F_y can be considered to be a function of α only. In such cases the lift and drag coefficients can be measured on a static tip geometry as functions of α and used to evaluate C_y with Equation 2.6. Although this approach is used in the implementation of the model, it is important to recognize that this is not an accurate representation of the aerodynamic behaviour when the timescales are

not separated, which is the case at least in part of the regime evaluated in the wind tunnel experiment.

2.3.3 Determination of Mechanical Parameters

Before the mathematical model and experimental data could be compared, the mechanical parameters of the galloping oscillation had to be determined. These included the effective stiffness of the cantilever beam K_{beam}, the mechanical damping coefficient C_{damp} and the tip mass m. The tip mass was measured using a set of precision weighing scales. To obtain the damping coefficient and effective stiffness, the blade was displaced and released under zero wind conditions, allowing decaying oscillations to be recorded by the motion tracking system. As the oscillations were close to sinusoidal and highly under-damped, the oscillation frequency could be assumed to be the natural frequency and hence was obtained with a zero crossing algorithm. By matching this to the natural frequency of simulated system,

$$\omega_n = 2\pi\sqrt{\frac{K_{\text{beam}}}{m_{\text{eff}}}}, \tag{2.7}$$

the effective stiffness could be evaluated. The damping coefficient was evaluated with the use of the Hilbert transform by similar methods to those described by Feldman [38]. The Hilbert transform is defined as

$$H(u)(t) = \frac{1}{\pi}\int_{-\infty}^{\infty}\frac{u(\tau)}{t-\tau}d\tau, \tag{2.8}$$

and enabled the amplitude envelope of decaying oscillations to be evaluated. Figure 2.5 illustrates an example time series of decaying oscillations and the calculated amplitude envelope. The amplitude envelope is de-trended and temporally filtered with a low pass Gaussian filter to remove the influence of slight asymmetry in the oscillation prior to evaluating the Hilbert transform. The damping coefficient can then be extracted by

$$C_{\text{damp}} = 2m_{\text{eff}}\frac{d}{dt}(\ln(A(t))), \tag{2.9}$$

where $A(t)$ is the instantaneous amplitude envelope. The derivative $\frac{d}{dt}(\ln(A(t)))$ is assumed to be close to constant and was hence found by linear fitting as illustrated in subplot (b) of Figure 2.5. The extracted oscillation frequency and damping coefficient are detailed in Table 2.2, alongside the calculated effective beam stiffness K_{beam}.

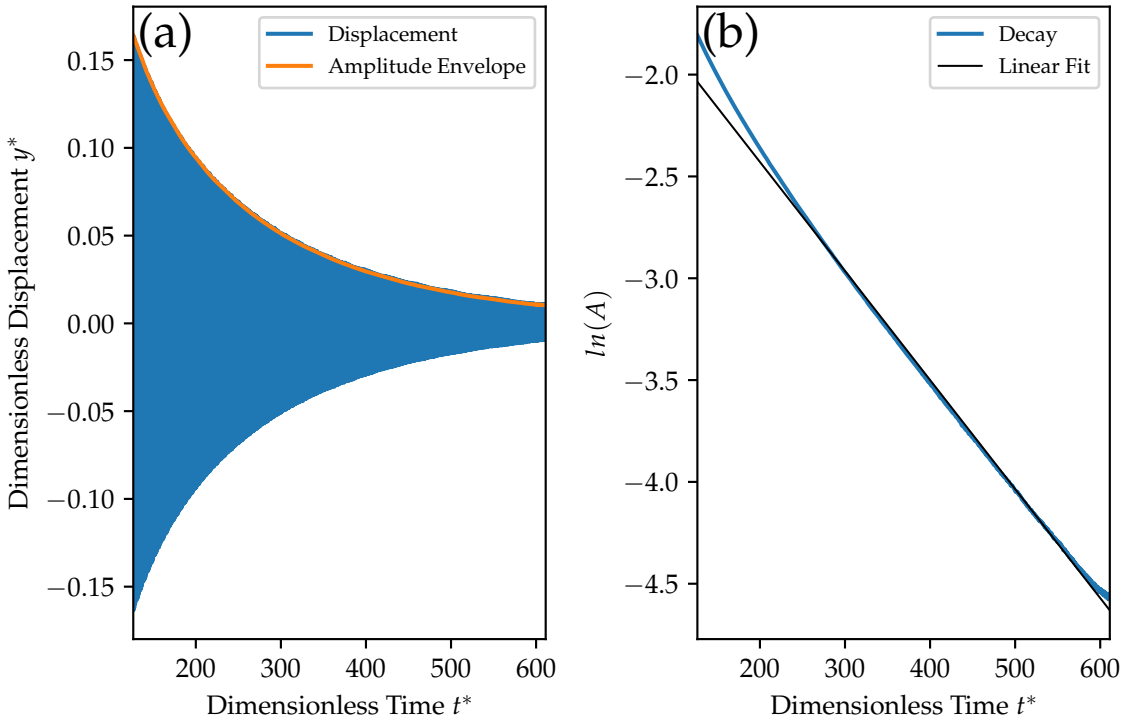

Figure 2.5: Illustration of amplitude enveloping of decaying oscillations and determination of damping coefficient. Subplot (a) demonstrates the amplitude envelope, while the linear fitting of the instantanous amplitude in log space is shown in subplot (b).

Parameter	Symbol	Value (unit)
Oscillation Frequency	ω	13.24 $(\mathrm{rad\,s^{-1}})$
Effective Beam Stiffness	K_{beam}	0.328 $(\mathrm{N\,m^{-1}})$
Damping Coefficient	C_{damp}	0.0017 $(\mathrm{N\,s\,m^{-1}})$

Table 2.2: Extracted mechanical parameters.

2.3.4 Measurement of Aerodynamic Forces

The aerodynamic forces which are formed on the curved-blade are critical in defining both the dynamics of the device and its potential as an energy harvester. However, as the aerodynamic forces are significantly smaller than the forces generated by the deflection of the cantilever beam, their direct measurement during an oscillation is not practically achievable whilst maintaining a reasonable level of accuracy. Yet, for the quasistatic aerodynamic term in the mathematical model to be simulated, the steady aerodynamic force coefficient C_y was required as a function of α. By Equation 2.6 this could be obtained by separate

measurements of the lift and drag coefficients with angle of attack made with a static curved-blade. The lift and drag coefficient of a static blade were hence measured experimentally with a single axis force balance and the resulting coefficients used to calculate C_y.

The force balance was designed around a Futek LSB200 load cell, which had a capacity of 0.2 N. Due to the large weight of the blade relative to the magnitude of the aerodynamic forces, the blade could not be directly mounted to the load cell without surpassing its force limits. The blade was hence mounted to a lever which allowed the weight of the blade to be supported by the structure and ensured only the aerodynamic forces were applied to the load cell. The fulcrum of the lever was created with two socket joints with stainless steel spheres within polytetrafluoroethene (PTFE) sockets, minimising the frictional forces generated within the joints. To balance the moment created by the weight of curved-blade when the sting was perturbed from the vertical orientation, a counterweight was attached below the lever arm. To reduce the influence of vibration on the measurements, a viscous damper was mounted to one end of the lever. The damper consisted of a 3D printed ABS sphere which was contained within a cylindrical volume of glycerol and mounted by a steel rod to the lever arm of the force balance. Figure 2.6 below illustrates the construction of the force balance, while Figure 2.7 shows the position of the force balance within the wind tunnel test section. The balance was attached to the mounting plate of a larger force balance already positioned below the test section. This provided robust fixing to the laboratory floor via damped fixtures.

The acquisition circuitry was based around a Burr-Brown INA125 precision amplifier, which amplified the output signal as well as providing a stable input voltage to the bridge. The signal was acquired with a National Instruments USB-6009 Multifunction I/O device, providing a 10 bit resolution and a sampling rate of 200 Hz. The load cell was calibrated prior to its assembly into balance by application of known masses.

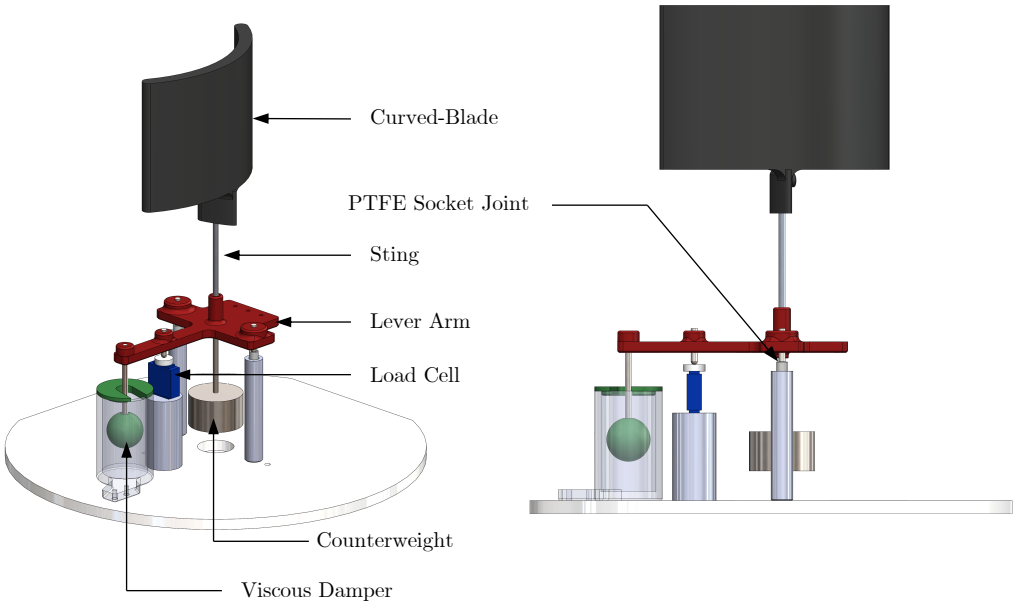

Figure 2.6: Illustration of force balance design.

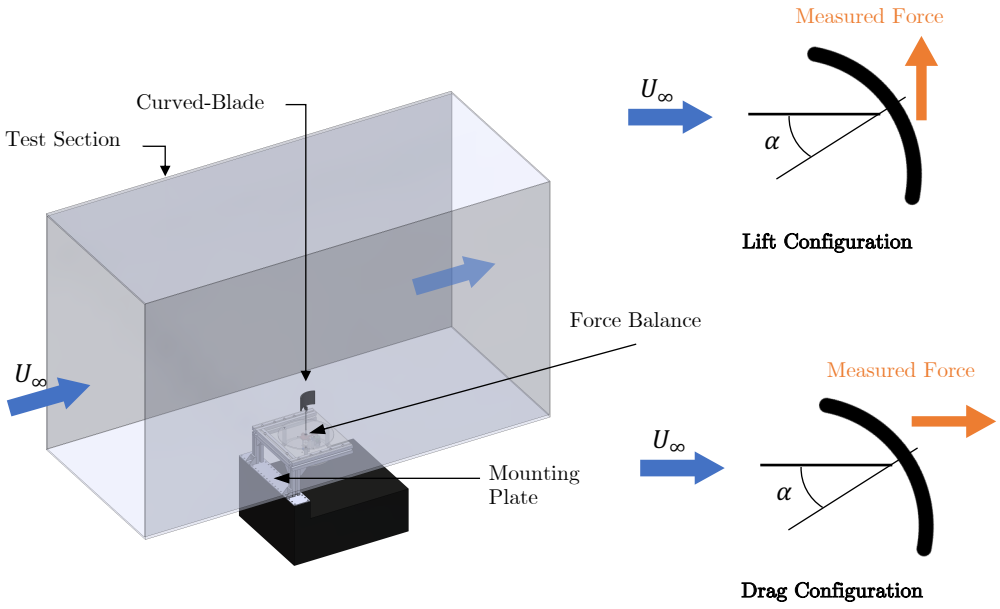

Figure 2.7: Illustration of force balance location within wind tunnel test section. U_∞ denotes the freestream flow direction, while α illustrates the angle of attack created by rotating the curved-blade on the rigid sting.

The measurement procedure began with the curved-blade being rotated on the sting forming an angle between the plane of symmetry of the curved-blade and the freestream flow velocity direction as illustrated in Figure 2.7. As the blade was rigidly mounted to the sting and hence stationary, this angle defined the angle of attack. Depending on whether the lift or drag coefficient was to be measured, the force balance was either configured to measure the force perpendicular or parallel to U_∞. A signal was then acquired from the load cell under no flow conditions to allow the subtraction of a zero aerodynamic force offset from the results. The wind tunnel was then operated at a flow velocity of $1.6\,\mathrm{m\,s^{-1}}$, while a 2 min signal was acquired from the load cell with a sampling frequency of 200 Hz. The first 90 s of the signal was ignored as it contained the transient start-up of the wind tunnel and the remaining 30 s was averaged and used to calculate the aerodynamic force. The measurements were repeated five times to provide a good measure of their uncertainty and 25 different angles of attacks were measured with the load cell positioned to measure both lift and drag forces.

The uncertainty of the evaluated aerodynamic coefficients can be quantified by propagating estimations of the errors of the measured forces and flow velocity. Firstly considering the lift and drag coefficients

$$C_l = \frac{2F_l}{\rho A_f U_\infty^2}, \quad C_d = \frac{2F_d}{\rho A_f U_\infty^2}. \tag{2.10}$$

Taking the partial derivatives with respect to measured force F_x and flow velocity yields

$$\frac{\partial C_x}{\partial F_x} = \frac{2}{\rho A_f U_\infty^2}, \quad \frac{\partial C_x}{\partial U_\infty} = \frac{4F_x}{\rho A_f U_\infty^3}, \tag{2.11}$$

where C_x denotes either the lift coefficient or drag coefficient and F_x represents either the lift force or drag force. The subsequent quantified uncertainty in the calculated force coefficient σ_{c_x} can be calculated by

$$\sigma_{c_x}^2 = \left(\frac{\partial C_x}{\partial F_x}\right)\sigma_{F_x}^2 + \left(\frac{\partial C_x}{\partial U_\infty}\right)\sigma_U^2, \tag{2.12}$$

where σ_{F_x}, σ_U denote the estimated uncertainties in the measured aerodynamic force and flow velocity respectively. Similar analysis of Equation 2.6 provides an expression for the estimated uncertainty in C_y as

$$\sigma_{c_y}^2 = \cos^2(\alpha)\sigma_{c_l}^2 + \sin^2(\alpha)\sigma_{c_d}^2 + \left(C_l \sin(\alpha) + C_d \cos(\alpha)\right)^2 \sigma_\alpha^2. \tag{2.13}$$

The resulting statically measured force coefficients are demonstrated in Figure 2.8, with error bars illustrating the measurement uncertainties as estimated by equations 2.12

and 2.13. Subplot (a) demonstrates the projections of the lift and drag coefficient by $\cos(\alpha)$ and $\sin(\alpha)$ respectively, which corresponds to the direction of $\dot{y}$ in Figure 2.1. Considering Equation 2.6, the difference of these two projected coefficients provides the C_y force coefficient which acts to accelerate the motion of the curved-blade. The three regions in which the projection of the lift coefficient pulls away from the drag coefficient projection hence relate to the three peaks in the C_y coefficient illustrated in subplot (b). The numerical simulation of Equation 2.15 could then be performed by linearly interpolating the C_y coefficient from the statically measured coefficients at each time step.

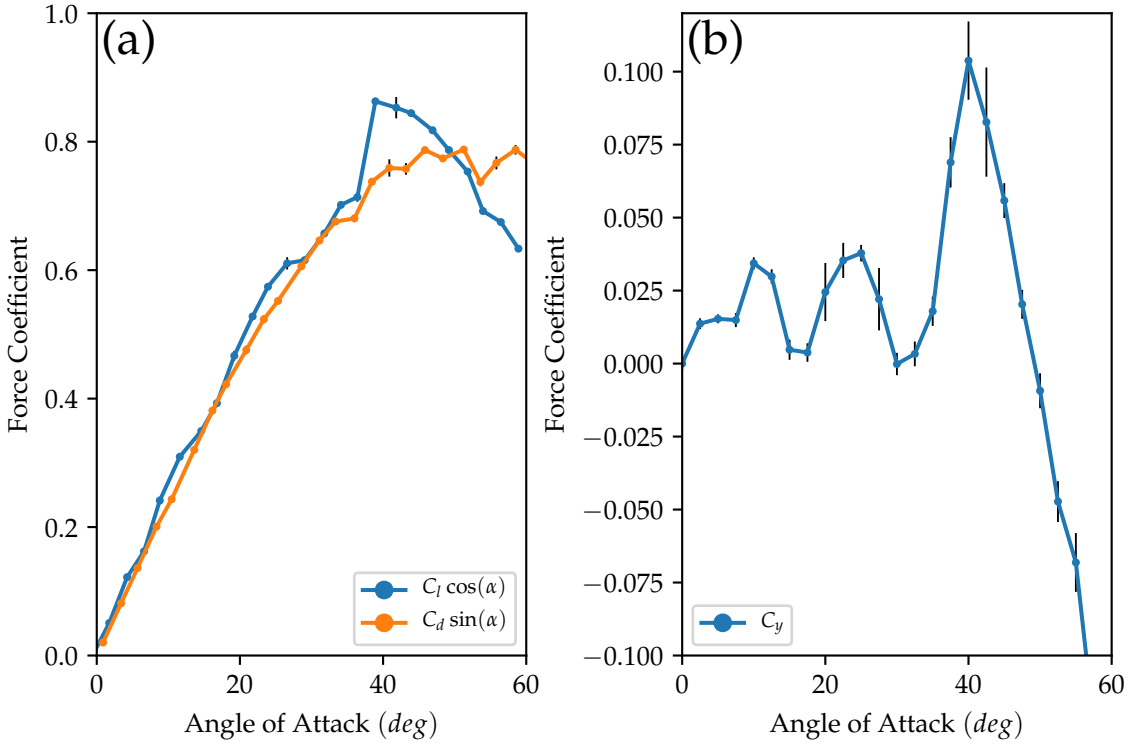

Figure 2.8: Curved-blade statically measured force coefficients. C_y calculated by Equation 2.6.

2.3.5 Experimental Results and Comparison to Mathematical Model

The nature of the limit cycle formed by the galloping oscillator comprises an important part of its dynamics. With the assumption that the motion of the blade is planar, its position can be described by its centre of mass coordinates in the j, k plane of Figure 2.1 denoted by y and z respectively, while its orientation can be defined by the maximum slope angle of the beam ψ. The power spectrum of the y displacement demonstrates the frequency composition of the oscillation, which can be evaluated via the Discrete Fast

Fourier Transform (DFFT). This is shown in Figure 2.9 with a range of reduced velocities, where reduced velocity U^* is defined as $\frac{2\pi U_\infty}{\omega_n Ch}$. Although multiple harmonics are observed, the first harmonic is of substantially greater power than those following with a high quality factor, suggesting that the oscillation is close to sinusoidal. The second harmonic relates to the asymmetry of trajectory, which is likely to have been caused by an asymmetry in the cantilever beam stiffness. However, with a power of four orders of magnitude smaller than the main oscillation, this is not a significant effect.

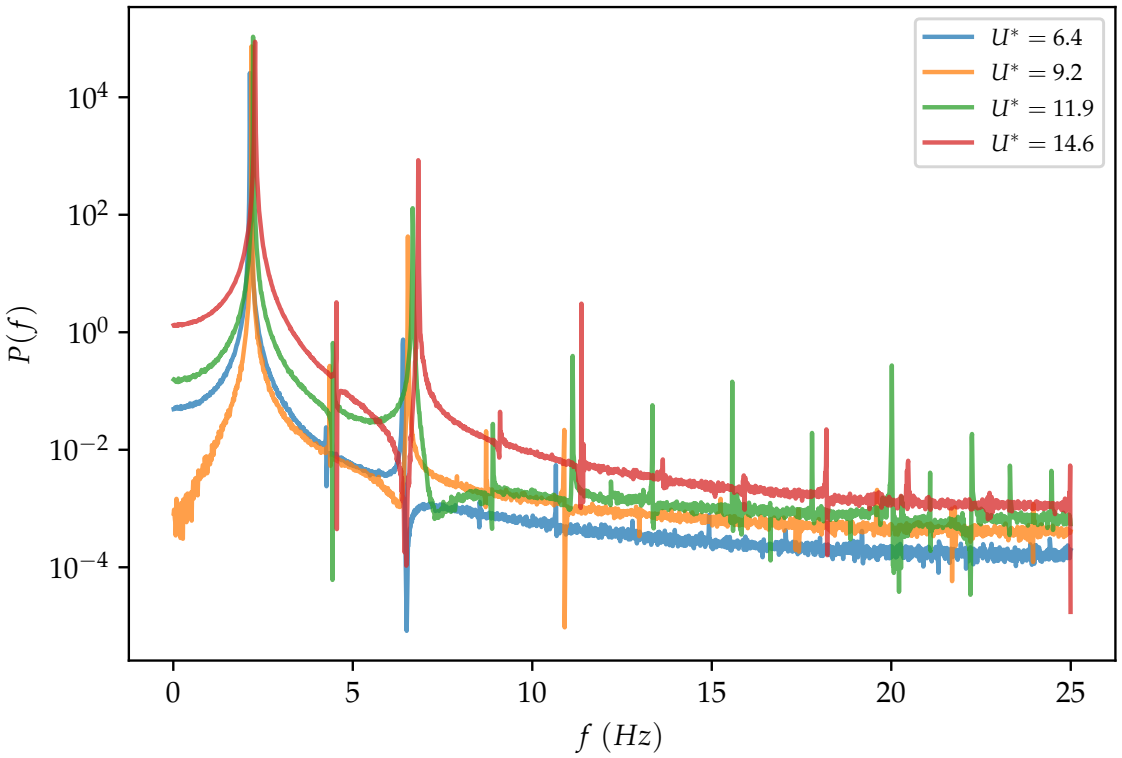

Figure 2.9: Limit cycle y displacement power spectrum.

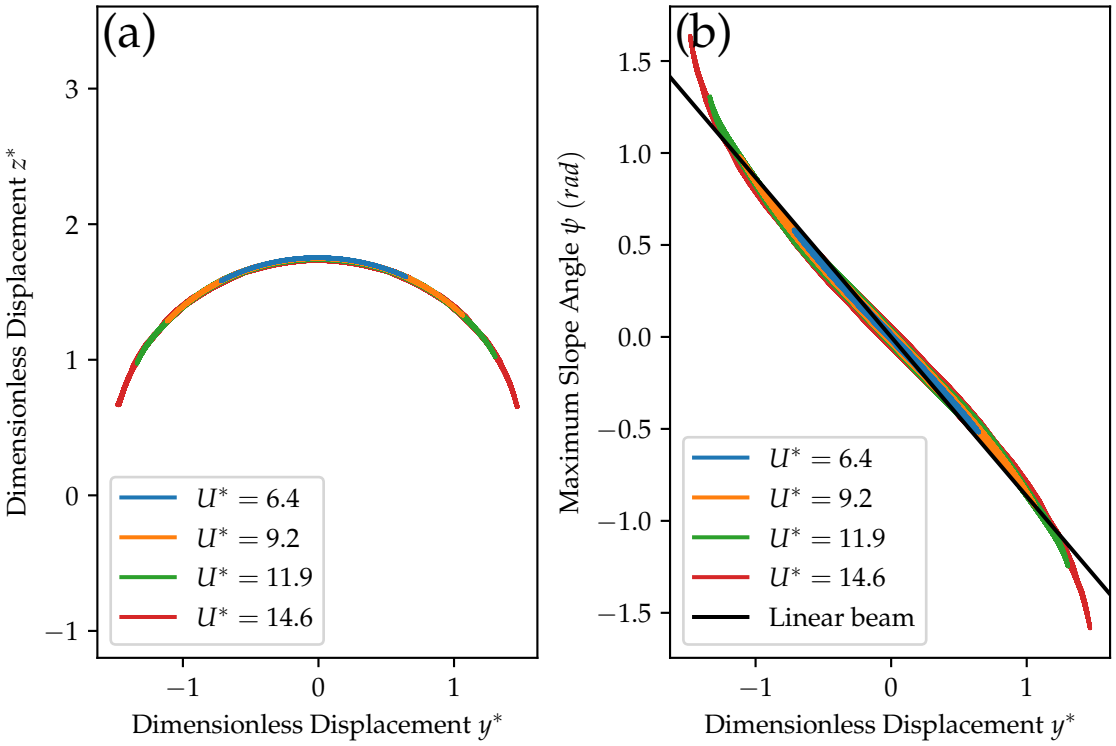

Figure 2.10: Illustration of blade trajectory on a range of limit cycles. z^* and y^* denote the dimensionless displacement in the j and k directions respectively and are given by $z^* = z/Ch$, $y^* = y/Ch$. Subplot (a) illustrates the trajectory of blade centre of mass, whilst the trajectory of the blade orientation is demonstrated in subplot (b).

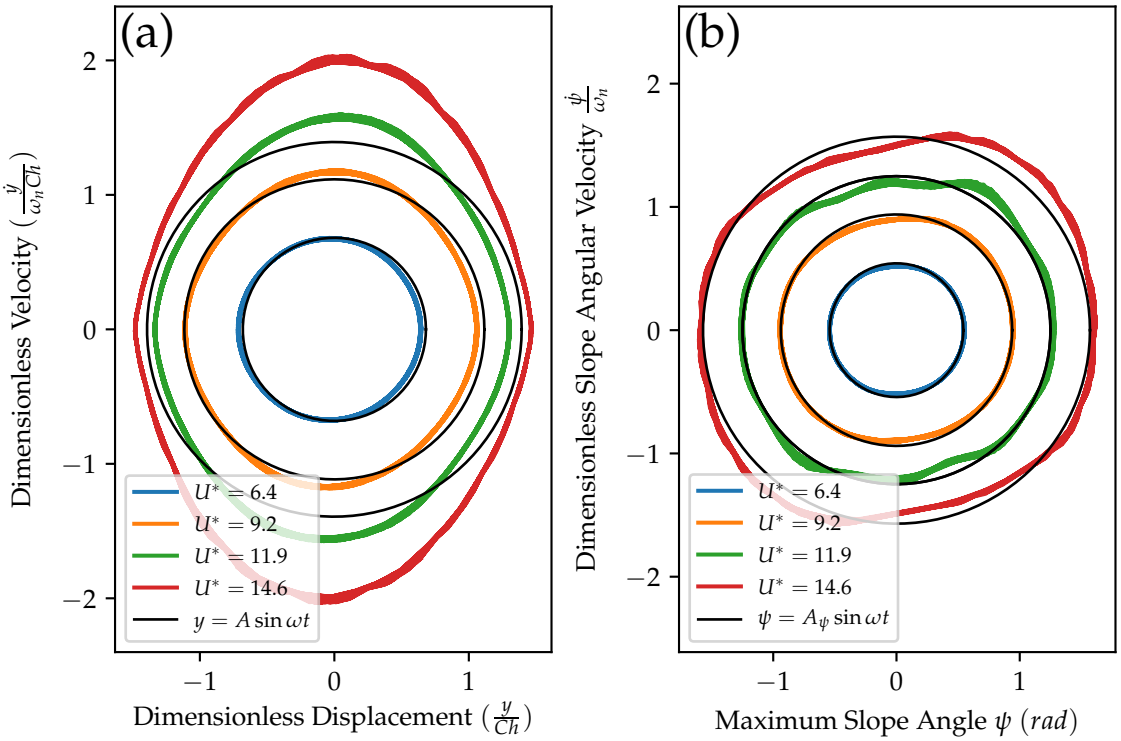

Figure 2.11: State space representation of limit cycles at a range of reduced velocities. The black circles represent sinusoidal oscillations of equal amplitude. Subplot (a) shows the $y, \dot{y}$ state space projection. Subplot (b) shows the $\psi, \dot{\psi}$ state space projection

The trajectory of the blade centre of mass within the j, k plane is illustrated in subplot (a) of Figure 2.10. At low reduced velocity the z displacement can be seen to be relatively small, however as the reduced velocity is increased and the oscillation amplitude grows, the z displacement becomes more significant. The relationship between the blade orientation ψ and the y displacement is demonstrated in subplot (b) of Figure 2.10. The relationship is largely linear, although deviating close to the displacement maximas at the highest oscillation amplitudes, and is well predicted by the small deflection linear beam model. This hence validates the application of a one-to-one relationship between y and ψ for the formulation of an effective mass in the mathematical model.

As the position and orientation of the blade is described by three variables, z, y and ψ, the state space is six-dimensional. For each of the variables the limit cycle can be plotted into a two-dimensional projection of the state space corresponding to each variable and its time derivative. Subplot (a) in Figure 2.11 demonstrates the state space projection of the limit cycle in the $y, \dot{y}$ plane, while the $\psi, \dot{\psi}$ projection is shown in Subplot (b) in Figure 2.11. Perfectly sinusoidal oscillations of a single degree of freedom form circles in the two-

dimensional state space, as illustrated by the black lines. In the case of the $y, \dot{y}$ projection, at low reduced velocity when the oscillations are relatively small, the limit cycles are close to circular, hence suggesting that they can be well described by a sine curve. As the reduced velocity and amplitude grow this projection of the limit cycle becomes distorted due to the growing presence of vertical motion of the blade. The $\psi, \dot{\psi}$ projection retains a circular trajectory to a much greater oscillation amplitude, although higher frequency distortions are observable, which likely to relate to oscillations in the ψ degree of freedom.

The amplitude variability is another key characteristic of the limit cycle. Computing the oscillation amplitude with the Hilbert transform and filtering with a Gaussian low pass filter of standard deviation equal to an oscillation period yields a estimate of the oscillation amplitude over time. Examples of the limit cycles amplitude distributions evaluted from both the y, $\dot{y}$ and ψ, $\dot{\psi}$ state space projections are illustrated in Figure 2.12. The distributions are shown normalized with their means. The variation of amplitude for the four example cases is small, relating to a maximum normalised standard deviations of 0.0063 and 0.0067 for the y and ψ degrees of freedom respectively.

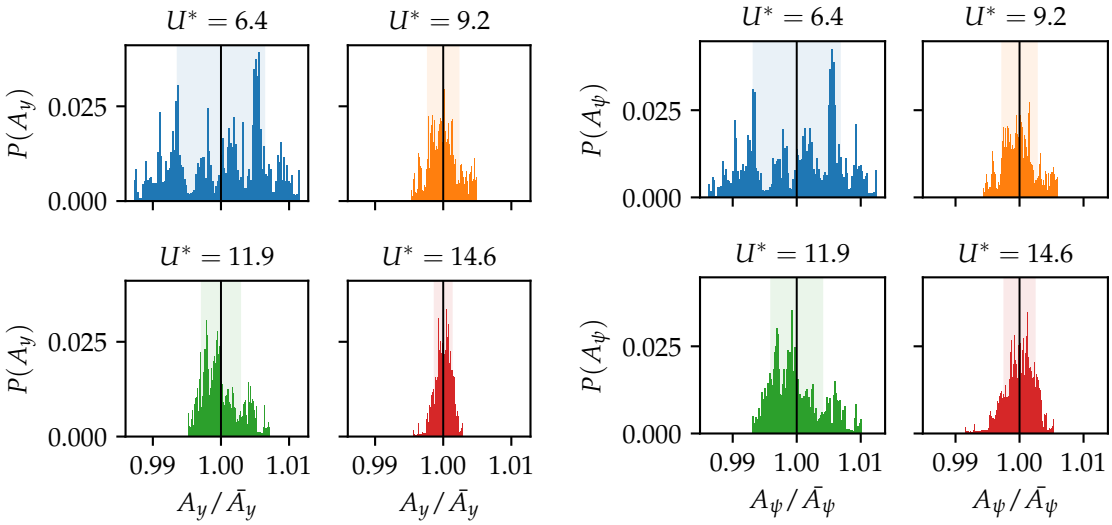

(a) Limit cycle amplitude variation in the y, $\dot{y}$ projection

(b) Limit cycle amplitude variation in the ψ, $\dot{\psi}$ projection

Figure 2.12: Amplitude variation of limit cycle evaluated with the y and ψ variables

The relationship between oscillation amplitude and flow velocity is an essential feature of a galloping oscillator, particularly its bifurcation behaviour. The evaluated variation of oscillation amplitude with reduced velocity demonstrates the different branches of oscillations, as well as the bifurcations which exist between them. The harvester exhibited a subcritical Hopf bifurcation in the wind tunnel experiment, with oscillations beginning at

the flow velocity of $1.11\,\mathrm{m\,s^{-1}}$ while flow velocity was increased, and remaining until the flow velocity of $0.90\,\mathrm{m\,s^{-1}}$ when flow velocity was decreased as shown by the blue line in the inset within subplot (a) of Figure 2.13. The Strouhal number was determined experimentally behind a static blade to be 0.2, as later described in Section 2.5. As the Hopf bifurcation occurs close to a reduced velocity of $1/St$, unsteady effects are likely to have a significant influence on the onset of oscillations. The maximum measured velocity amplitude of the blade occurred at the oscillation amplitude of 0.24 m or 2.2 Ch, where Ch denotes the curved-blade chord length. A branch of smaller amplitude oscillations was found to exist at wind speeds above $3.1\,\mathrm{m\,s^{-1}}$. The existence of two distinct branches of oscillations separated so significantly in amplitude is suggestive of a difference in physical mechanism between them and is discussed further in relation to the flow visualisations in Section 2.4.

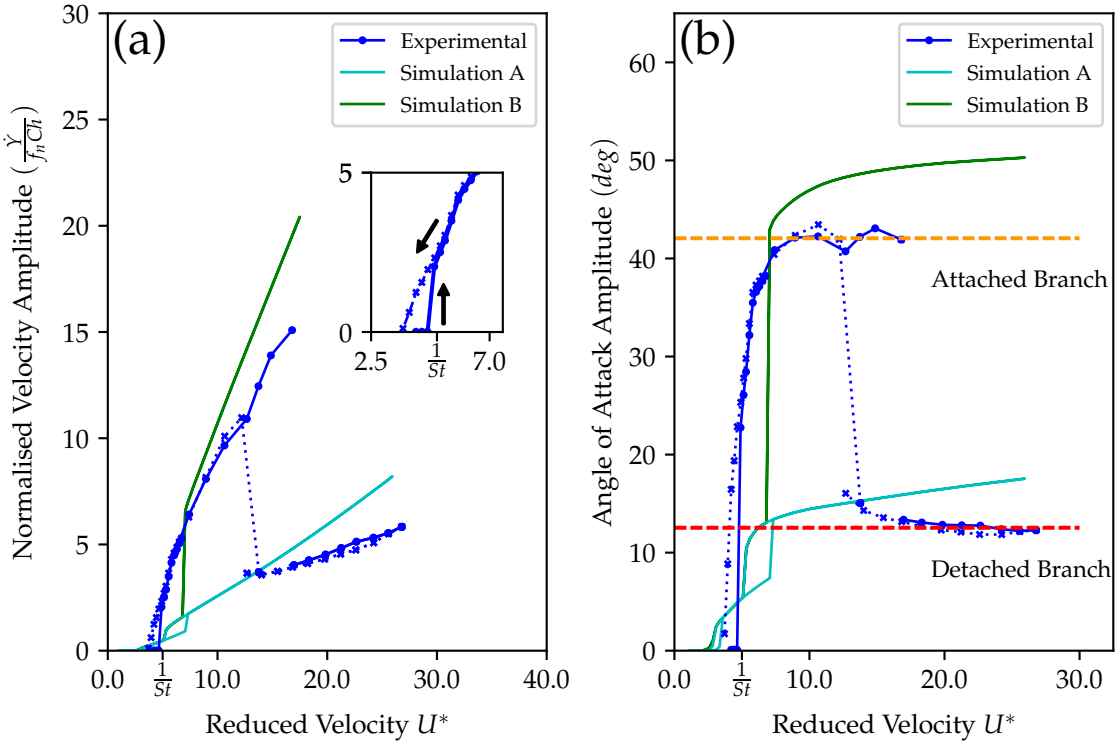

Figure 2.13: Experimental and simulated harvester dynamics. Dotted lines with crosses represent behaviour with decreasing reduced velocity. Subplot (a) illustrates the normalised velocity amplitude versus reduced velocity with the inset demonstrating the hysteresis loop created by the subcritical Hopf and saddle-node bifurcation. Subplot (b) shows the angle of attack amplitude with reduced velocity. The dashed lines mark the average of the final five points in high and low amplitude branches. The reduced velocity of $\frac{1}{St}$ is marked.

Figure 2.13 also presents simulation results of the mathematical model obtained with both small pertubation and large displacement initial conditions, labelled simulation

A and B respectively. The mathematical model demonstrates two branches of stable limit cycles, occurring at similar velocity amplitudes to the experimentally measured cycles. In agreement with experimental data, the Hopf bifurcation was subcritical in the model, although the subcritical branch was of significantly shorter length. The bifurcations however differed with the low amplitude branch growing from the Hopf bifurcation in the model, rather than the high amplitude branch as observed in the wind tunnel experiment. The simulation results also demonstrate an additional hysteresis loop formed by a pair of saddle-node bifurcations, occurring just after the Hopf bifurcation. In Figure 2.8 this relates to the harvester moving from operation around the first C_y peak to the second C_y peak as flow velocity is increased. Unsteady flow effects may hence allow the oscillations to surpass the second C_y peak in the experiment moving directly to the large amplitude branch.

The maximum angle of attack α for both the experimental dynamics and the mathematical model are demonstrated in subplot (b) of Figure 2.13. In both the experimental dynamics and mathematical model, the maximum angle of attack can be seen to become insensitive to the flow velocity far from the Hopf bifurcation. The angles of attack to which the low and high amplitude branches are tending towards can be seen to correspond to the first and last peak in C_y in Figure 2.8. This is illustrated by the dashed lines in Figure 2.13. The last peak in C_y in Figure 2.8 can be seen to relate to the sudden jump in the projection of the lift coefficient, $C_l \cos\alpha$.

2.4 Flow Visualisation and Particle Image Velocimetry

Flow visualisation provides an effective means of gaining an insight into experimental fluid phenomena without the requirement of extensive point velocity measurements, while particle image velocimetry (PIV) allows the quantitative measurement of velocity field via image processing techniques [86]. To investigate the flow structures around the blade, the smoke-wire technique was applied with a twisted pair of 0.255 mm diameter wires mounted horizontally across the wind tunnel test section and coated in mineral oil. At the maximum flow velocity at which flow visualisations were performed, the Reynolds number of the wire was 23. A voltage was then applied across the wire with a DC power supply. The subsequent heating vapourised the mineral oil and hence seeded the flow. The vapourised oil was illuminated with a 0.5 W laser projector, while images were captured by a Phantom high speed camera mounted above the harvester at 1000 fps with an image size of 1152 $\times$ 720 pixels. The analysis was performed with Dantec PIV software using an adaptive correlation algorithm. Figure 2.2 demonstrates the configuration of the PIV and motion tracking systems within the test section.

Figure 2.14 illustrates the flow visualisation and PIV results for steady-state oscil-

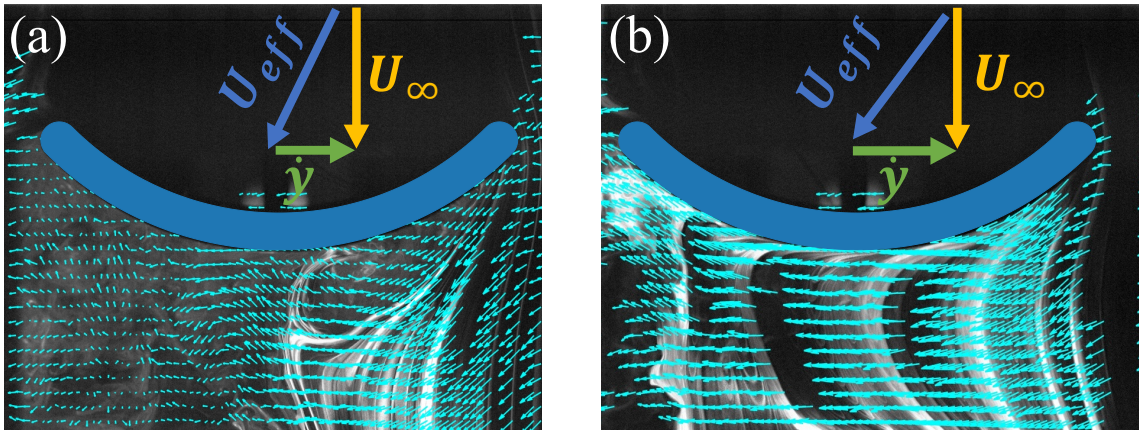

Figure 2.14: Flow visualisation results at mid-position, where the tip speed is maximum. In subplot (a) the flow velocity is $1.13\,\mathrm{m\,s^{-1}}$, reduced velocity $U^* = 5.0$ and angle of attack $\alpha = 26°$. Flow detachment and the turbulent wake are observed. In subplot (b) the flow velocity is $1.37\,\mathrm{m\,s^{-1}}$, reduced velocity $U^* = 6.0$ and angle of attack $\alpha = 37°$. Attached flow is observed.

lations at two different reduced velocities. The blade is viewed from above with the rear surface facing the bottom of the image. The blade position is close to that of maximum velocity and the velocity field is plotted in a frame of reference moving with the blade. The visualisation in subplot (a) reveals leading edge separation and a large wake at low angle of attack, however in subplot (b), at higher angles of attack the flow is found to become attached. During each half-oscillation cycle, the flow becomes detached as the blade stops at maximum displacement. As the blade then accelerates back to its mid-position, the angle of attack increases and the flow becomes attached. The first of these two cases relates to the lower amplitude branch discovered in the experimental dynamics described in Section 2.3, while the attached flow observed in subplot (b) can be connected to the higher amplitude branch. The two branches therefore correspond to different flow phenomenon as the flow only becomes attached in the higher amplitude branch. Pronounced unsteady flow effects were observed with flow patterns varying substantially between oscillation cycles. Wake interaction was observed at the lowest flow velocity with shed vortices being convected back onto the rear surface of the blade as the direction of motion reversed.

2.5 Hot-Wire Velocimetry

2.5.1 Methodology

To gain an insight into the unsteady flow structures developed around the curved-blade both in a static and dynamic case, hot-wire velocimetry was employed. Hot-wire velocimetry is a valuable tool which can supply point velocity measurements with high accuracy and frequency response in a range of fluid mediums [19]. The fundamental principle of operation relies on measuring the convective cooling of a thin wire or film by the flow and relating this measurement to flow velocity. Although different approaches can be applied in the measurement of the cooling effect, here a constant temperature methodology is utilised, where the current through the wire is varied by a control loop to maintain a constant temperature and this applied current used to determine flow velocity.

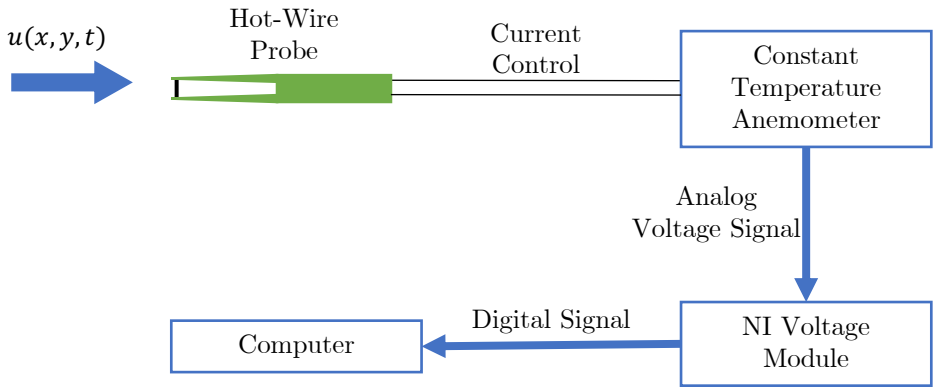

Figure 2.15: Illustration of constant temperature anemometer system.

As illustrated by Figure 2.15, a constant temperature anemometer system can be decomposed into three main components, the probe, constant temperature anemometer and acquisition system. The acquisition system was implemented with a National Instruments NI-9215 voltage input module, which had a sampling frequency of 20 kHz and a 16 bit resolution, in combination with a computer. A Dantec 55P11 miniature wire probe, consisting of a 5 µm diameter plated tungsten wire of length 1.25 mm, was connected to a MiniCTA 54T42 constant temperature anemometer to form the rest of the system.

The relationship between output voltage and flow velocity is typically largely non-linear in hot-wire velocimetry and hence careful calibration is required. Calibration was performed against the pitot tube and FC0560 manometer arrangement described in Section

2.3.1. A nine point calibration was applied and a third-order polynomial fitted to describe the relationship between output voltage and flow velocity. As the calibration is sensitive to the environmental conditions, such as the ambient temperature, it was repeated for each series of experiments. A typical calibration curve and fitted polynomial is illustrated in Figure 2.16. The third-order polynomial can be seen to provide an accurate representation of the calibration data.

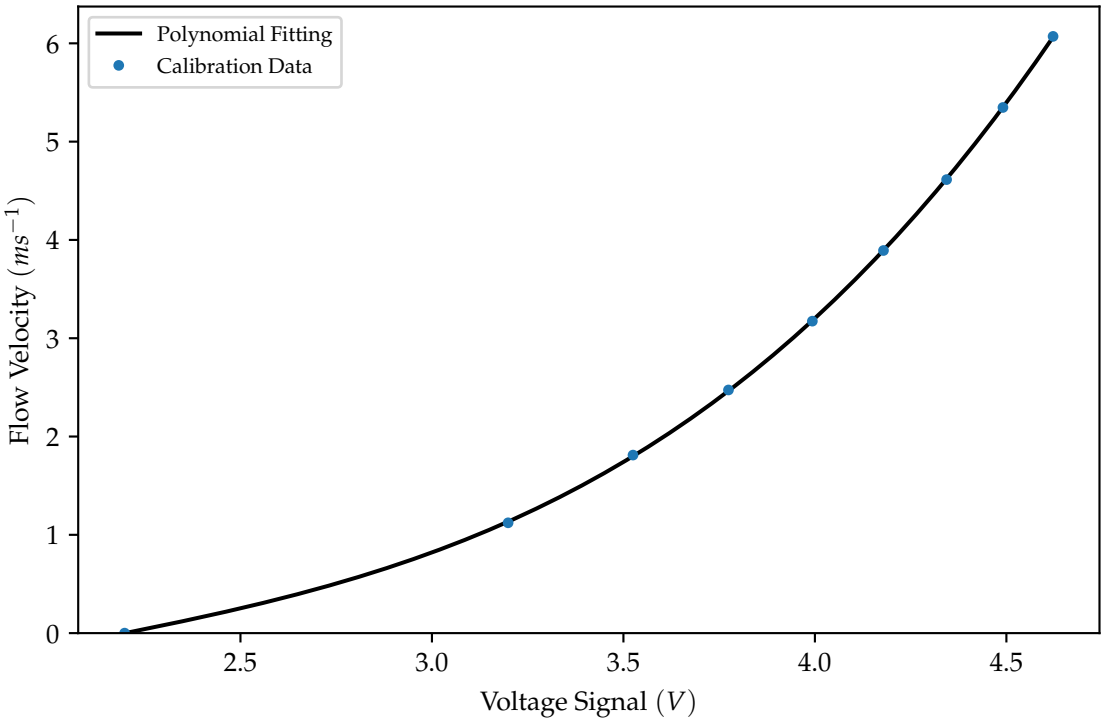

Figure 2.16: Example hot-wire anemometer calibration curve. Flow velocity and voltage signal error-bars as estimated with standard deviation are smaller in size than the markers.

The flow around the curved-blade varies depending on the blade kinematics. As the flow cannot be assumed to be quasistatic, measurements were made both with a blade mounted rigidly with its plane of symmetry inclined to the freestream flow direction as in Figure 2.7, resulting in a constant angle of attack, and also with an oscillating blade, where the angle of attack oscillates. The first of these cases will be referred to as the static curved-blade, while the second as the oscillating curved-blade.

To investigate the frequency composition of the unsteady flow structures formed on the static curved-blade, hot-wire measurements were made on the edge of the wake. The hot-wire probe was positioned a distance of 15 mm from the rear face at centre chord and at a vertical position 20 mm above the blade. Results were obtained at five angles of attack

and at five Reynolds numbers. The position of the hot-wire probe was rotated around the centre of rotation of the curved-blade, ensuring that its position with respect to the blade remained constant. The position of the hot-wire probe relative to the curved-blade is illustrated for three of the investigated angles of attack in Figure 2.17.

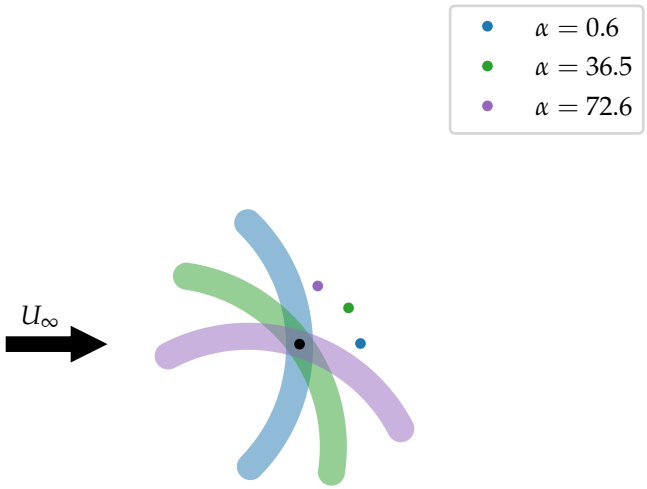

Figure 2.17: Position of hot-wire probe relative to curved-blade.

Further to investigating the unsteady flow structures on a static curved-blade, measurements were also made on an oscillating blade. To provide a reference to the oscillation phase with the hot-wire signal, a light gate was positioned over the cantilever beam. This allowed the hot-wire measurements to be phase averaged with the oscillation phase ϕ. The light gate incorporated a Light Emitting Diode (LED) and Light Dependent Resistor (LDR), which were mounted such that the beam of the LED illuminated the surface of LDR. By positioning the light gate around the cantilever such that it obstructed the LED beam in its unperturbed state and connecting the LDR to a 5 V voltage divider, a signal could be produced which contained a peak at each passing of the cantilever beam across its zero displacement position. This signal could be acquired simultaneously with the hot-wire signal by the NI-9215 voltage input module. Figure 2.18 demonstrates the construction of the light gate and its position relative to the curved-blade and cantilever beam.

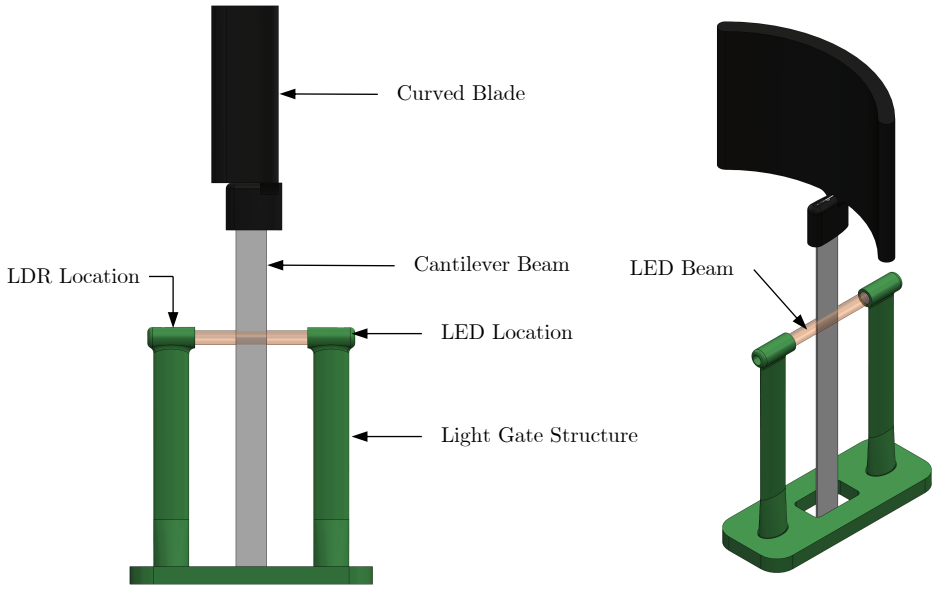

Figure 2.18: Illustration of light gate assembly.

A typical voltage signal generated by the light gate is demonstrated in Figure 2.19. The signal was first filtered with a low pass Gaussian filter before a peak detection algorithm was applied to identify the locations of the peaks, which correspond to the time instances at which the curved-blade passed the zero displacement position. With the zero displacement time instances established, the oscillation phase was assumed to evolve linearly between each set of passings with $\phi = 0$ as the first, $\phi = \pi$ as the second and the cycle completed with $\phi = 2\pi$ at the final passing of the zero displacement position.

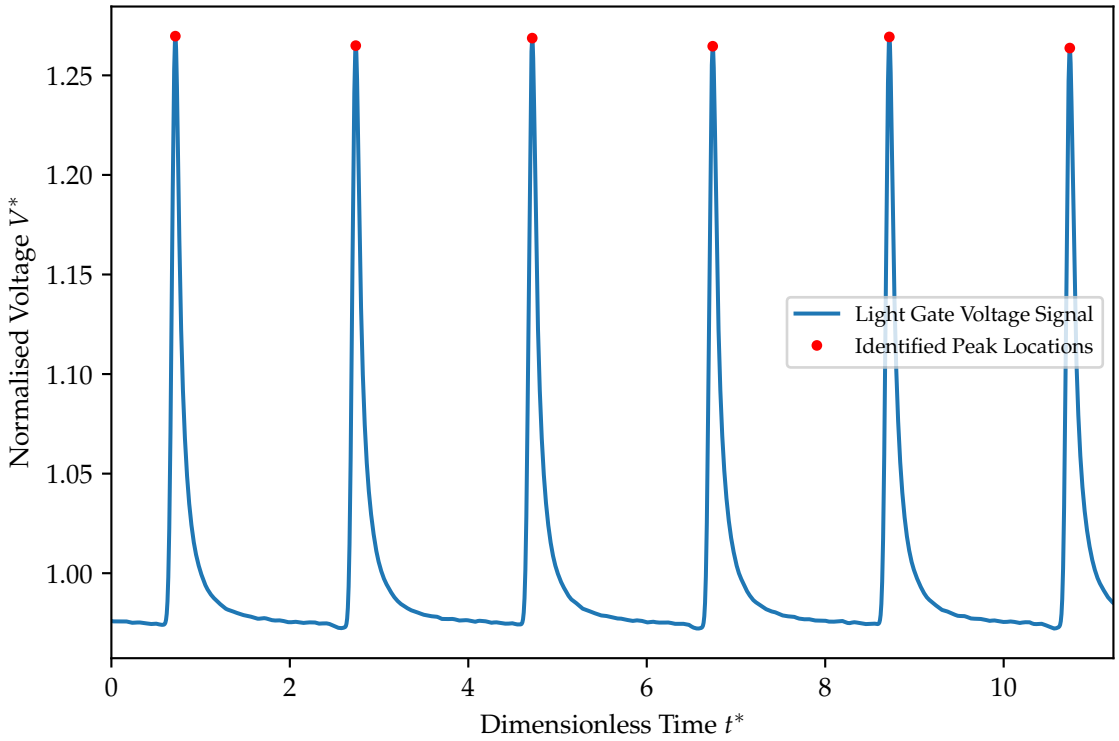

Figure 2.19: Example voltage signal from light gate. Time is non-dimensionalised with the oscillation period, hence $t^* = \frac{t}{2\pi\omega}$, while the voltage signal is normalised by its mean value.

2.5.2 Results with Static Curved Blade

The relationship between the mean flow velocity, as well as the turbulence intensity, with angle of attack α is demonstrated in Figure 2.20. The velocity variation can be seen to be much greater at the lowest two angles of attack, suggesting that in these cases the hot-wire probe was within the wake region. The normalised velocity was greater than unity for the all angles of attack over 19° with the maximum occurring at an angle of attack of 55° across the whole Reynolds number range.

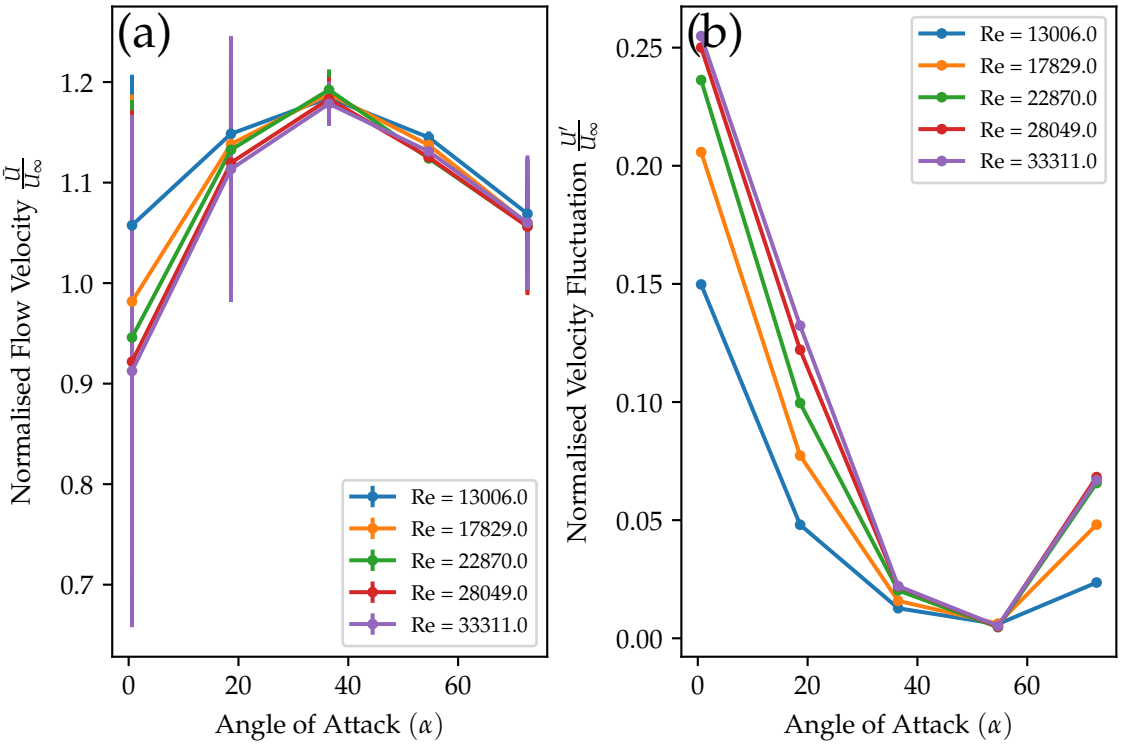

Figure 2.20: Statistical properties of static curved-blade hot-wire measurements. Subplot (a) shows the mean flow velocity normalised by the freestream, whereas the the turblence intensity is shown in subplot (b).

By inspecting the frequency composition of the velocity measurements, an insight into the scales of the unsteady flow structures can be gained. Figure 2.21 illustrates the power spectrums with non-dimensional frequency $\frac{Chf}{U_\infty}$, which directly corresponds to Strouhal number. The non-dimensional frequency is shown in the range from 0 to 1, which corresponds to structures of length scale equal to or larger than the chord length. In the lowest angle of attack case, where the axis of the curved-blade is close to perpendicular with the flow direction, no clear and periodic large scale unsteady structures were detected by the hot-wire measurements as demonstrated by the lack of a distinct spectral peak in subplot (b) of Figure 2.21. At an angle of attack of 18.6° a clear spectral peak is evident across the full range of evaluated Reynolds numbers corresponding to a Strouhal number of around 0.2. This is likely to relate to the periodic shedding of vortices. A peak is also evident at an angle of attack was of 36.5°, however occurring at a slightly high frequency relating to a Strouhal number of around 0.3 and of significantly less power. This suggests that increasing the angle of attack results in a higher frequency of vortex shedding. The absence of a peak in the zero degree angle of attack spectrum is likely to relate to the

positioning of the hot-wire probe as the unsteady shedding of vortices would be expected in this situation.

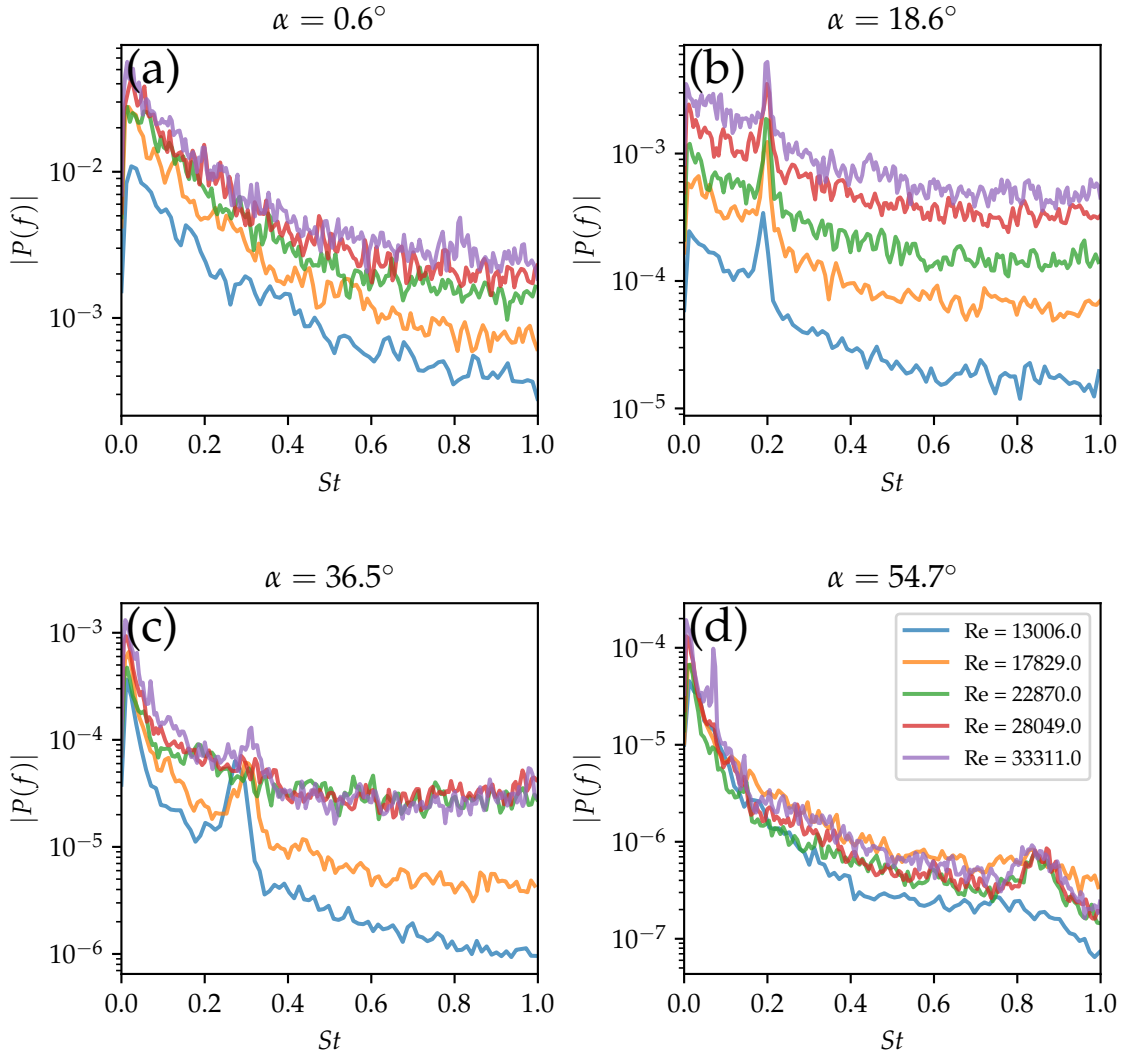

Figure 2.21: Hot-wire velocity power spectrums. Frequency is normalised with the freestream flow velocity U_∞ and chord length Ch and hence can be represented as Strouhal number St.

2.5.3 Results with Oscillating Curved Blade

To evaluate the frequency composition of the hot-wire time series whilst maintaining a high temporal resolution, the wavelet transform was applied using a Morlet wavelet. The subsequent spectrogram was phase averaged by interpolating onto a phase array defined by the peaks detected in the light gate signal. Figure 2.22 demonstrates the wavelet power after

phase averaging a 10 minute time series for each of the displayed cases. An oscillation phase ϕ of zero relates to the phase instance in which the curved-blade is at its zero displacement position and is hence directly in front of the hot-wire probe. Between a phase of 0 and $2\,\pi$ the curved-blade passed the hot-wire probe a further time before returning to its zero displacement position at $\phi = 2\pi$. The regions of high power in the hot-wire signal relates to the edge of the curved-blade wake, which given the position of the hot-wire probe above the curved-blade is likely to consist of the tip vortex. As the wake evolved in time during each oscillation whilst the curved-blade also moved relative to the hot-wire probe position, the changing power spectrum with phase presented in Figure 2.22 cannot strictly be decomposed into the temporal or spatial variance of the wake but rather is a combination of both. The plots show a clear distinction between the attached branch, shown in subplots (a) and (b), and the detached branch, shown in (c) and (d). The wake region can be seen to occur close to $\phi = \pi$ in the subplot (a) and (b), when the probe is directly behind curved-blade. This is consistent with the attached flow regime as the wake region is likely to intersect with the hot-wire probe closer to the trailing edge of the curved-blade. In subplots (c) and (d), the wake region is detected notably prior to $\phi = \pi$, illustrating the flow was highly separated, while the splitting of the high power region into distinct peaks may correspond to the shedding of multiple wake structures.

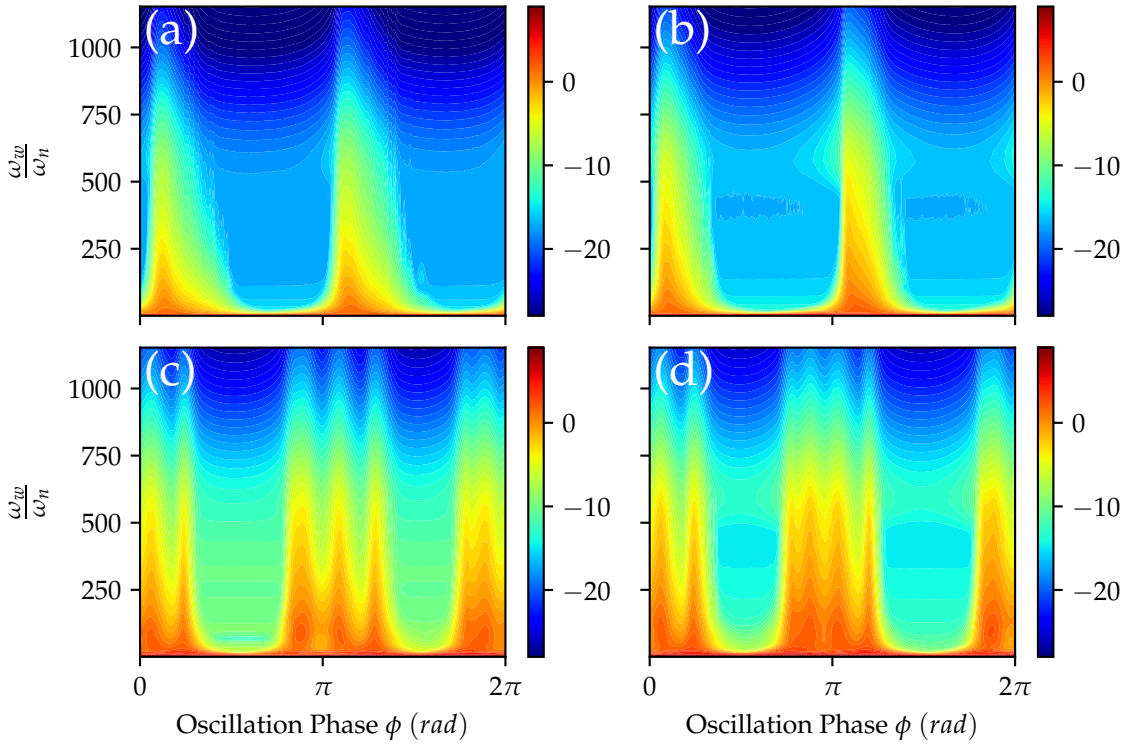

Figure 2.22: Wavelet power spectrogram of hot-wire signals captured behind oscillating curved-blades. The colourmap shows $\log_2 P$ to improve the clarity of the results. Subplots (a) and (b) were acquired from the high amplitude branch with reduced velocities of 12.5 and 16.9 respectively, while subplots (c) and (d) represent the behaviour in the lower amplitude branch with reduced velocities of 30.0 and 35.0. ϕ corresponds to the oscillation phase, while ω_w is the wavelet frequency and ω_n is the natural oscillation frequency.

2.6 Prediction of Harvesting Performance

Although the experimental evaluation of the dynamics of the curved-blade galloping oscillator in Section 2.3, in combination with the flow visualisations in Section 2.4, demonstrate the existence of multiple branches of oscillations and some of the underlying fluid mechanisms, an evaluation of the potential energy harvesting performance has not yet been presented. To investigate the energy harvesting potential of the curved-blade, similarly to Abdelkefi et al [2] an additional equation was simulated representing a piezoelectric harvesting circuit given by

$$\dot{V} = -\frac{1}{C_{\text{piez}}}\left(\frac{V}{R_l} + \theta\dot{y}\right), \tag{2.14}$$

where C_{piez} is the capacitance of the piezoelectric element, R_l denotes the load resistance,

V the generated voltage and θ the electromechanical coupling factor. An additional term $\frac{\theta V}{m}$ is also added to Equation 2.15 to provide the feedback from the piezoelectric, resulting in the equation

$$\ddot{y} = \frac{1}{m}\left(F_y(\dot{y}) - K_{\text{beam}}y - C_{\text{damp}}\dot{y}\right). \tag{2.15}$$

Typical values for θ and C_{piez} were taken from the work of Alhadidi [7] by matching non-dimensional coupling factor $\frac{2\pi\theta^2}{C_{\text{piez}}m\omega_n^2}$. By simulating the system with the additional equation the potential power output could be predicted. For comparison, simulations were also performed with the polynomial representation of C_y for the square-prism developed by Parkinson [79] given by

$$C_y = \sum_0^n a_i \tan^i \alpha = a_1 \tan\alpha + a_3 \tan^3\alpha + a_5 \tan^5\alpha + a_7 \tan^7\alpha, \tag{2.16}$$

where the polynomial coefficients are tabulated in Table 2.3.

a_1	a_2	a_3	a_4	a_5	a_6	a_7
2.69	0	−168	0	6270	0	−59900

Table 2.3: Polynomial coefficients of the aerodynamic force representation for the square-prism [79].

The load resistances were optimised to maximise output power. Figure 2.23 demonstrates the comparison of the simulated oscillation displacement and angle of attack amplitudes between the square-prism and curved-blade. In both cases, the dependance of the displacement amplitude on reduced velocity becomes close to linear at the higher end of the considered range, corresponding to a constant angle of attack amplitude as illustrated in subplot (b). At low reduced velocities, the curved-blade operates close to its first C_y maxima corresponding to an angle of attack amplitude of around 12°. As the reduced velocity increases, the falling significance of mechanical damping in relation to aerodynamic forces enables the curved-blade to surpass the first C_y peak and operate at a much higher angle of attack.

The simulated harvested power for both the curve blade and square-prism are shown in subplot (a) of Figure 2.24. When operating in the higher amplitude branch the curved-blade is predicted to produce significantly more power than the square-prism. Coefficient of performance is a widely utilised metric for the quantifying the efficiency with which a device can convert energy from fluid flow and is defined as the ratio of converted power to the power available in the fluid contained within the swept area of the device [57]. This can be defined mathematically as

$$C_p = 2\frac{P}{\rho A_{\text{swept}} U_\infty^3}, \tag{2.17}$$

where A_{swept} denotes the swept area. Subplot (b) demonstrates a comparison of the coefficient of performance simulated for the curved-blade and square-prism geometries. As swept area grows with oscillation amplitude, the devices appear more efficient at low reduced velocity, when the oscillation amplitude is small. This enables the square-prism to obtain greater values of C_p that predicted for the curved-blade at higher reduced velocity.

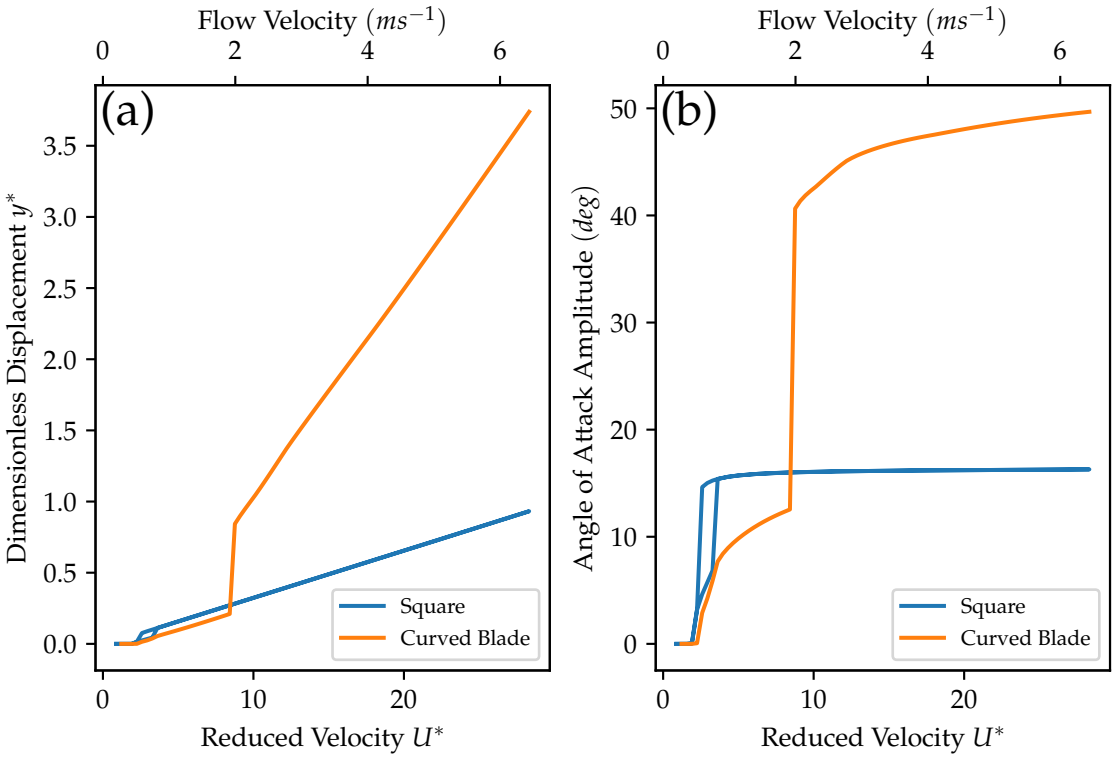

Figure 2.23: Comparison of simulated oscillation amplitudes between the curved-blade and square-prism.

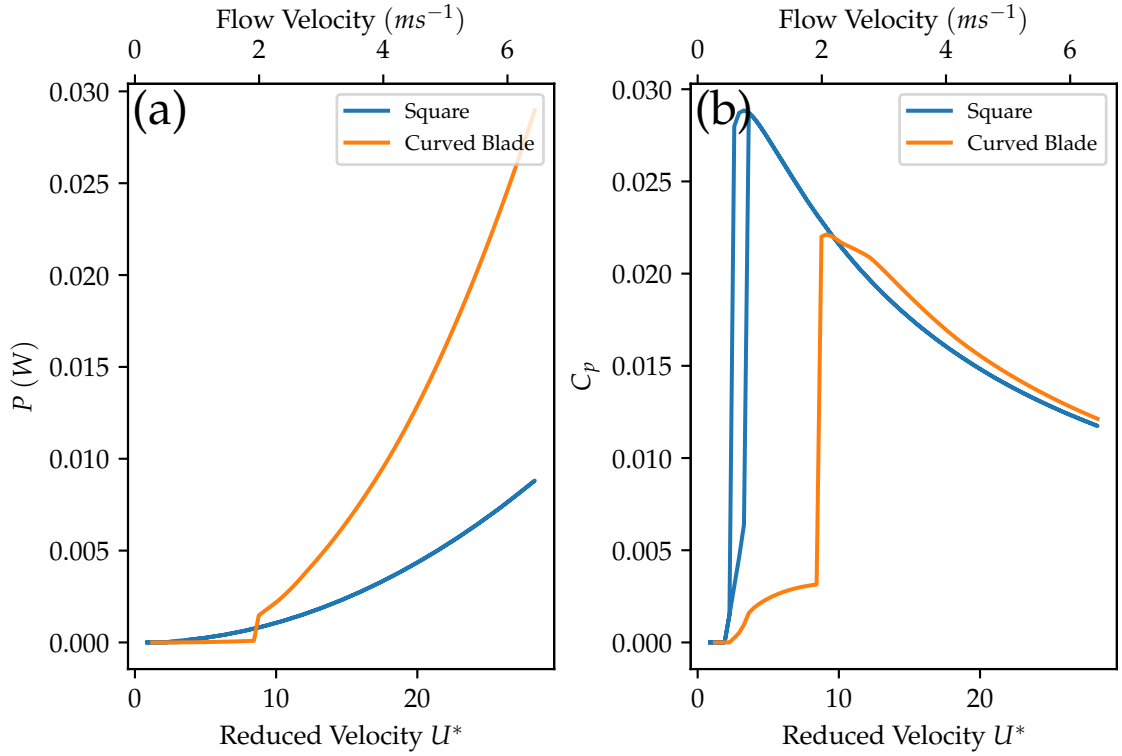

Figure 2.24: Comparison of simulated output power and coefficient of performance between the curved-blade and square-prism.

2.7 Summary

In this chapter, we have presented a curved-blade geometry for a galloping energy harvester, inspired by the trembling of an Aspen leaf. An experimental investigation of the harvester dynamics has demonstrated the existence of two disinct branches of oscillations separated significantly in amplitude. Flow visualations and PIV measurements have illustrated that, when in the higher amplitude branch, the flow becomes attached to the rear face of the curved-blade when its linear velocity is close to its maximum, while in the lower amplitude branch the flow remains separated. A lumped-parameter model based on a quasistatic representation of the aerodynamic forces has been formulated and demonstrated to also exhibit two branches of limit cycles close to those observed experimentally. The discrepancies between the model and the experiment are attributed to the unsteady nature of the flow around the harvester tip, which requires further investigation. Simulations have also predicted the curved-blade geometry to produce more power than the widely considered square-prism when operating in the high amplitude branch.

3

Characterising Energy Harvesting Performance from the Free Oscillation Transient

3.1 Introduction

The measurement of output power forms a key component of the development of all forms of energy harvesting systems. Evaluating the performance of piezoelectric energy harvesting from nonlinear systems which form self sustained oscillations or limit cycles due to a nonlinear damping term is typically performed by either evaluating a system experimentally with a transduction mechanism implemented [108, 49] or by modelling the nonlinearity and simulating the system coupled to a harvesting circuit [3]. The difficulty with the first method is that the performance is highly dependent on the electromechanical coupling and the parameters of the harvesting circuit. Hence, an experimental optimisation should be performed to ensure the device is operating at its maximum performance. As the number of parameters to optimise is significant, this can require a substantial number of experiments before an optimum is obtained and it is not always convenient or even possible to alter the properties of the electromechanical coupling. The second method allows the optimisation to be performed either analytically or by simulation which is less time consuming, however there can be difficulties regarding the evaluation and modeling of the nonlinear term of a

physical system [54], especially in the presence of unsteady aerodynamic effects.

In this chapter a method is presented which aims to characterise the energy harvesting performance of a galloping energy harvester or similar self-excited system from the free oscillation transient of the oscillator with no harvesting mechanism connected. The proposed method uses the growth rate of total energy during the transient of a system with no harvesting circuit to predict the optimal performance. This allows different systems to quickly be evaluated experimentally and compared in terms of their performance without the optimisation of harvesting parameters or the evaluation and modeling of the damping nonlinearity. As the method exploits the energy balance of the system, it bears similarities to methods which have been applied to find approximate analytical solutions to single degree of freedom energy harvesters with known nonlinearity [112, 90], however in this case the problem is reversed in that trajectory is known but the nonlinearity is not. The method is however dependent on timescale separation between the dissipative and conservative terms in the system. In this chapter the mathematical formulation of the method is presented and the accuracy of the method is demonstrated when applied to simulations of a harvester based on both the Van Der Pol and Rayleigh oscillators. The accuracy is evaluated over a wide range of timescale separations to establish the region in which the method can reliably be applied. We then apply the method to the case of a galloping oscillator with realistic parameters.

3.2 Derivation of Method

3.2.1 Definition of General System

The derivation begins by first considering the governing ordinary differential equations for a single degree of freedom mechanical oscillator with nonlinear damping $f(y, \dot{y})$ coupled to a piezoelectric energy harvesting circuit as formulated in [3],

$$\ddot{y} - \frac{1}{m} f\left(y, \dot{y}\right) \dot{y} + \omega_n^2 y - \frac{\theta}{m} V = 0, \tag{3.1}$$

$$\dot{V} = -\frac{1}{C_{\text{piez}}} \left(\frac{V}{R_l} + \theta \dot{y} \right), \tag{3.2}$$

where Equation 3.1 represents the dynamics of a mechanical oscillator with displacement y and nonlinear damping dependent on y and/or $\dot{y}$. The mass of the oscillator is denoted by m and ω_n represents the natural frequency. The oscillator is coupled linearly to Equation 3.2 by electromechanical coupling factor θ. Equation 3.2 describes the dynamics of a piezoelectric harvesting circuit consisting of a load resistor of resistance R_l, and a piezoelectric element

with capacitance C_{piez}.

By multiplying Equation 3.1 by the linear velocity $\dot{y}$ and the oscillator mass m, an equation in terms of instantaneous power can be obtained as

$$m\dot{y}\ddot{y} - f\left(y,\dot{y}\right)\dot{y}^2 + m\omega_n^2 y\dot{y} - \theta V\dot{y} = 0. \tag{3.3}$$

With the assumption of periodic oscillations of frequency ω_n, Equation 3.3 can be cycle-averaged by integrating temporally between 0 and $\frac{2\pi}{\omega_n}$ and dividing by the oscillation period yielding

$$\frac{\omega_n}{2\pi}\int_0^{\frac{2\pi}{\omega_n}} m\dot{y}\ddot{y}dt - \frac{\omega_n}{2\pi}\int_0^{\frac{2\pi}{\omega_n}} f\left(y,\dot{y}\right)\dot{y}^2 dt + \frac{\omega_n}{2\pi}\int_0^{\frac{2\pi}{\omega_n}} m\omega_n^2 y\dot{y}dt - \frac{\omega_n}{2\pi}\int_0^{\frac{2\pi}{\omega_n}} \theta V\dot{y}dt = 0. \tag{3.4}$$

The total energy is now defined as the sum of the kinetic and potential energies in the galloping oscillator and can be written as

$$E_{\text{tot}} = \frac{1}{2}m\dot{y}^2 + \frac{1}{2}m\omega_n^2 y^2. \tag{3.5}$$

Taking the time derivative of the total energy and cycle averaging yields

$$\frac{d\bar{E}_{\text{tot}}}{dt} = \frac{\omega_n}{2\pi}\int_0^{\frac{2\pi}{\omega_n}} m\dot{y}\ddot{y}dt + \frac{\omega_n}{2\pi}\int_0^{\frac{2\pi}{\omega_n}} m\omega_n^2 y\dot{y}dt. \tag{3.6}$$

Substituting into Equation 3.3 gives

$$\frac{d\bar{E}_{\text{tot}}}{dt} - \overbrace{\frac{\omega_n}{2\pi}\int_0^{\frac{2\pi}{\omega_n}} f\left(y,\dot{y}\right)\dot{y}^2 dt}^{\bar{P}_f} - \overbrace{\frac{\omega_n}{2\pi}\int_0^{\frac{2\pi}{\omega_n}} \theta V\dot{y}dt}^{\bar{P}_{\text{elec}}} = 0. \tag{3.7}$$

Here $\bar{P}_f$ and $\bar{P}_{\text{elec}}$ denote the cycle-averaged power flows due to the nonlinear term $f\left(y,\dot{y}\right)\dot{y}$ and electromechanical coupling respectively. Similar consideration of Equation 3.2 provides a cycle-averaged power expression for the harvesting circuit

$$\overbrace{\frac{\omega_n}{2\pi}\int_0^{\frac{2\pi}{\omega_n}} C_{\text{piez}}V\dot{V}\,dt}^{\frac{d\bar{E}_{\text{cap}}}{dt}} = \overbrace{\frac{\omega_n}{2\pi}\int_0^{\frac{2\pi}{\omega_n}} \frac{-V^2}{R_l}\,dt}^{\bar{P}_{\text{harv}}} - \overbrace{\frac{\omega_n}{2\pi}\int_0^{\frac{2\pi}{\omega_n}} \theta\dot{y}V\,dt}^{\bar{P}_{\text{elec}}}, \tag{3.8}$$

where $\bar{P}_{\text{harv}}$ denotes the cycled averaged harvested power and $\frac{d\bar{E}_{\text{cap}}}{dt}$ is the cycle-averaged time derivative of the power contained within the capacitor in the circuit. Combining the two cycle-averaged equations in terms of power flows yields

$$\frac{d\bar{E}_{\text{tot}}}{dt} - \bar{P}_f = -\frac{d\bar{E}_{\text{cap}}}{dt} - \bar{P}_{\text{harv}}. \tag{3.9}$$

Provided there is significant timescale separation between the conservative and non-conservative terms the system can be considered as weakly nonlinear and hence the trajectory can be approximated as sinusoidal giving

$$y = A_y \sin(\omega t), \quad V = A_V \sin(\omega t + \phi_v), \tag{3.10}$$

where A_y denotes the amplitude of the y displacement, A_V is the amplitude of the voltage in the harvesting circuit and ϕ_v is the phase difference between the displacement and the voltage. Under this assumption, it can be shown that all terms in Equation 3.9 become functions of the displacement amplitude A_y only and hence the power flow is defined by the oscillation amplitude and the parameters. When the system is operating on a limit cycle, hence with constant amplitude, and energy is harvested with $\theta > 0$, there cannot be cycle-averaged accumulation of energy within either the electrical circuit or the galloping oscillator resulting in

$$\frac{d\bar{E}_{\text{tot}}}{dt} = 0, \quad \frac{d\bar{E}_{\text{cap}}}{dt} = 0. \tag{3.11}$$

This yields the simplification of Equation 3.9 to

$$\bar{P}_f = \bar{P}_{\text{harv}}. \tag{3.12}$$

Alternatively, considering a case without energy harvesting, hence $\theta = 0$, and in which oscillations are growing

$$\frac{d\bar{E}_{\text{tot}}}{dt} = \bar{P}_f. \tag{3.13}$$

Comparing equations 3.12 and 3.13 and considering that the terms are functions of the oscillation amplitude A_y only with the assumption of a sinusoidal trajectory

$$\frac{d\bar{E}_{\text{tot}}}{dt}|_{\theta=0} = \bar{P}_{\text{harv}}|_{\theta>0}. \tag{3.14}$$

Under the condition that the steady-state amplitude when $\theta > 0$ is equal to the instantaneous amplitude when $\theta = 0$,

$$A_y(\theta = 0) = A_y(\theta > 0). \tag{3.15}$$

The cycle-averaged accumulation of total energy within the mechanical oscillator $\frac{d\bar{E}_{\text{tot}}}{dt}$ without a harvesting mechanism therefore provides an estimate of the power which

could be harvested at the same instantaneous amplitude, A_y, if a mechanism where to be implemented and harvested energy under steady-state conditions, whilst maintaining constant amplitude.

3.2.2 Characterisation of Stability

By predicting the steady-state performance of the system with a harvesting circuit at a given amplitude, the method has stated that the addition of a harvesting circuit will result in the formation of a limit cycle at this amplitude. This limit cycle could be either stable, unstable or half-stable depending on the nature of the nonlinearity of the function $f(y, \dot{y})$. An approach can be made to evaluate the stability by calculating the derivative of the cycle-averaged power flow with respect to the oscillation amplitude A_y. When operating under steady-state conditions with a harvesting circuit, there will be no cycle-averaged power flow and hence

$$\bar{P}_f - \bar{P}_{\text{harv}} = 0. \tag{3.16}$$

Considering the derivative of this power flow with respect to oscillation amplitude the stability criterion can be formulated as

$$\frac{d}{dA_y}\left(\bar{P}_f - \bar{P}_{\text{harv}}\right) \begin{cases} < 0, & \text{stable} \\ > 0, & \text{unstable} \\ = 0, & \text{half-stable} \end{cases}. \tag{3.17}$$

Evaluating the second term, $\frac{d\bar{P}_{\text{harv}}}{dA_y}$, requires the assumption of a voltage trajectory, which as stated in Equation 3.10 is assumed to be sinusoidal. This yields

$$\bar{P}_{\text{harv}} = \frac{\omega_n}{2\pi}\int_0^{\frac{2\pi}{\omega_n}} \frac{V^2}{R_l} dt = \frac{\omega_n}{2\pi}\int_0^{\frac{2\pi}{\omega_n}} \frac{A_v^2 \sin^2\left(\omega_n t + \phi_v\right)}{R_l} dt. \tag{3.18}$$

The voltage amplitude A_v and voltage phase difference ϕ_v are still required in terms of the displacement amplitude and the system parameters. Similarly to Tan et al [90], by considering the original ordinary differential equation representing the harvesting circuit, Equation 3.2, and substituting sinusoidal functions for the voltage and displacement and their time derivatives, the phase difference ϕ_v and voltage amplitude A_v can be shown to be

$$\phi_v = \tan^{-1}\left(\frac{1}{C_{\text{piez}} R_l \omega_n}\right), \quad A_v^2 = \frac{R_l^2 \theta^2 \omega_n^2}{1 + C_{\text{piez}}^2 \omega_n^2 R_l^2} A_y^2. \tag{3.19}$$

Performing the integral in Equation 3.18 and substituting for A_v yields

$$\bar{P}_{\text{harv}} = \frac{A_y^2}{2}\left(\frac{R_l^2\theta^2\omega_n^3}{1+C_{\text{piez}}\omega_n^2R_l^2}\right). \tag{3.20}$$

Taking the derivative with respect to A_y gives

$$\frac{d\bar{P}_{\text{harv}}}{dA_y} = A_y\left(\frac{R_l^2\theta^2\omega_n^3}{1+C_{\text{piez}}\omega_n^2R_l^2}\right). \tag{3.21}$$

As the stability should be evaluated on the limit cycle where power flows are balanced, Equation 3.16 can be used to provide an additional condition and in combination with Equation 3.20, allows the derivative to be written in terms of $\bar{P}_f$ as

$$\frac{d\bar{P}_{\text{harv}}}{dA_y} = \frac{2\bar{P}_f}{A_y}. \tag{3.22}$$

By consideration of Equation 3.13, the total energy growth rate in the free transient can be utilised to predict $\bar{P}_f$ by

$$\frac{d}{dA_y}\left(\bar{P}_f - \bar{P}_{\text{harv}}\right) = \frac{d}{dA_y}\left(\frac{d\bar{E}_{\text{tot}}}{dt} - \bar{P}_{\text{harv}}\right). \tag{3.23}$$

The stability criterion hence becomes

$$\frac{d}{dA_y}\left(\frac{d\bar{E}_{\text{tot}}}{dt}|_{\theta=0}\right) - \frac{2}{A_y}\left(\frac{d\bar{E}_{\text{tot}}}{dt}|_{\theta=0}\right)\begin{cases} <0, & \text{stable} \\ >0, & \text{unstable} \\ =0, & \text{half-stable} \end{cases}. \tag{3.24}$$

3.3 Implementation of Method

Further to the derivation of underlying mathematics behind the method, in this section we describe its implementation. When capturing the dynamics of a nonlinear oscillator by experimental means, some combination of the state space variables is typically measured. In the case of the single degree of freedom mechanical oscillator, these variables are comprised of $y(t)$ and $\dot{y}(t)$. The objective of the method is to obtain a prediction of the power output and stability as a function of the oscillation amplitude A_y with the state space variables as a starting point. As shown by the mathematical derivation in Section 3.2, the power can be predicted by Equation 3.14, while the stability of the subsequent limit cycle is given by 3.24.

The implementation of the method is illustrated in Figure 3.1. Beginning with the state space variables $y(t)$ and $\dot{y}(t)$, the total energy is first calculated by use of Equation

3.5. This requires the mass of the system to be known, as well as assuming that the stiffness term is linear. To evaluate the cycle-average of the total energy, rather than integrating from t to $t+\frac{2\pi}{\omega_n}$ and dividing by the oscillation period, which is essentially a moving average filter, a low pass Gaussian filter is implemented as this is more effective at removing high frequency noise. The standard deviation of the Gaussian filter was chosen to be half of the oscillation frequency in the frequency domain. With the cycle-averaged total energy computed, its time derivative was required to form the prediction of output power. This derivative was obtained by formulating a cubic spline between the points and taking the analytical derivative of each interval. This derivative thus formed the final prediction of power.

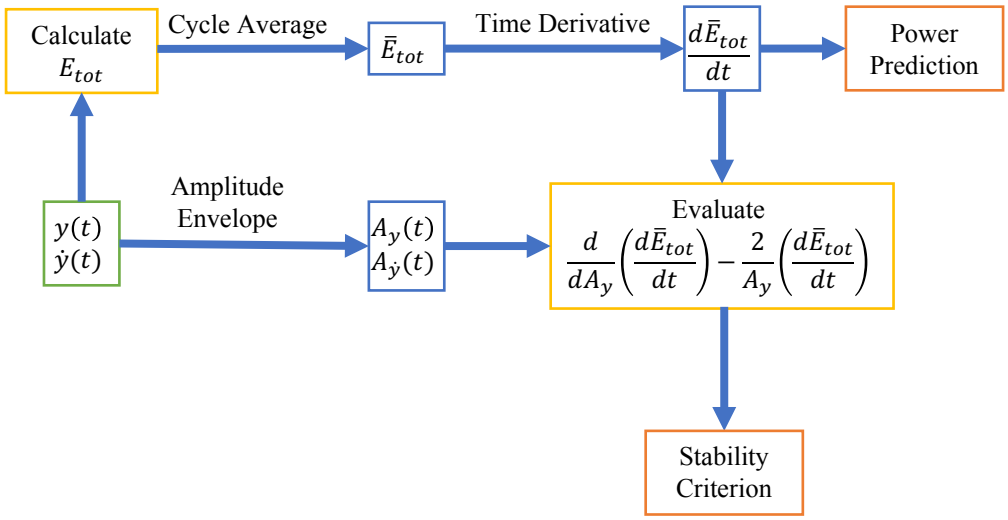

Figure 3.1: Illustration of transient method implementation.

As the stability criterion required the derivative of the cycle-averaged total energy with respect to oscillation amplitude, the amplitude envelope of both the displacement and velocity were evaluated by the absolute value of the discrete Hilbert transform. The stability criterion presented in Equation 3.24 could then be formulated and assessed to determine the stability of the predicted limit cycle.

3.4 Examples with Simple Nonlinearities

3.4.1 System Definition

To investigate the ability of the method to accurately characterise the energy harvesting performance of a system with a transduction mechanism from the free oscillation transient of a system without transduction, the system was considered with a number of different

nonlinearities with a wide range of timescale separations. The error in the prediction hence indicates the region of timescale separations over which the method is applicable. The Van Der Pol and Rayleigh oscillators contain the simplest nonlinearities which result in the formation of limit cycle oscillations and are good test cases for the method. Table 3.1 illustrates the nonlinearities for these two oscillators.

System	$f(y, \dot{y})$
Van Der Pol	$\mu\left(1-y^2\right)$
Rayleigh	$\mu\left(1-\dot{y}^2\right)$

Table 3.1: Definition of $f(y, \dot{y})$

3.4.2 Simulation Methodology

For both the Van Der Pol and Rayleigh systems, the timescale separation is defined by the parameter μ. To investigate how the accuracy of the prediction method changed with the timescale separation, μ was varied logarithmically from 1×10^{-2} to 5. At each value of μ results obtained by simulation of the system coupled to a harvesting circuit and the characterisation from the free oscillation transient were compared.

The simulations were performed with a fourth-order Runge-Kutta integration scheme which was implemented in a custom C++ script. Each simulation comprised of an initial value problem where the solution was evolved in time until steady-state behaviour was observed. This enabled stable limit cycles to be captured, as well as the transient formed during the evolution of the solution from the initial conditions to the stable limit cycle. The system was first simulated with $\theta = 0$ and small displacement initial conditions to allow the free transient to be captured and used to predict the harvesting performance. The performance was then calculated from simulations with $\theta > 0$ and with steady-state conditions established.

To evaluate the relationship between the steady-state oscillation amplitude and harvesting performance at each value of μ, the electromechanical coupling coefficient θ was varied linearly from zero to the value predicted by linear stability analysis to stabilise the equilibrium, denoted by $\theta_{\max}$. This value was determined by applying the bracketing method to the real parts of the repeated roots of the eigenvalues of the system Jacobian. To obtain the Jacobian of the Van der Pol and Rayleigh systems, the equations must first be written in normal form. In the case of the Van der Pol oscillator this yields

$$\begin{aligned}\dot{y}_0 &= y_1,\\ \dot{y}_1 &= \frac{\mu}{m}\left(1-y_0^2\right)y_1 - \omega_n^2 y_0 + \frac{\theta}{m}y_2,\\ \dot{y}_2 &= -\frac{1}{C_{\text{piez}}R_l}y_2 - \frac{\theta}{C_{\text{piez}}}y_1,\end{aligned} \tag{3.25}$$

where $y_0 = y$, $y_1 = \dot{y}$ and $V = y_2$. Similarly for the Rayleigh oscillator

$$\begin{aligned}\dot{y}_0 &= y_1,\\ \dot{y}_1 &= \frac{\mu}{m}\left(1-y_1^2\right)y_1 - \omega_n^2 y_0 + \frac{\theta}{m}y_2,\\ \dot{y}_2 &= -\frac{1}{C_{\text{piez}}R_l}y_2 - \frac{\theta}{C_{\text{piez}}}y_1.\end{aligned} \tag{3.26}$$

For both the Van Der Pol and Rayleigh oscillators, the system Jacobians can be written as,

$$\mathbf{J_{vp}} = \begin{bmatrix} 0 & 1 & 0\\ -\omega_n^2 - 2\mu\frac{y_0 y_1}{m} & \frac{\mu}{m}\left(1-y_0^2\right) & \frac{\theta}{m}\\ 0 & -\frac{\theta}{C_{\text{piez}}} & -\frac{1}{C_{\text{piez}}R_l}\end{bmatrix}, \quad \mathbf{J_r} = \begin{bmatrix} 0 & 1 & 0\\ -\omega_n^2 & \frac{\mu}{m}\left(1-3y_1^2\right) & \frac{\theta}{m}\\ 0 & -\frac{\theta}{C_{\text{piez}}} & -\frac{1}{C_{\text{piez}}R_l}\end{bmatrix}, \tag{3.27}$$

where $\mathbf{J_{vp}}$ and $\mathbf{J_r}$ denote the Jacobian of the Van der Pol and Rayleigh oscillators respectively. In both cases, the system has only a single trivial equilibrium position at $y = 0$, $\dot{y} = 0$, $V = 0$. Evaluating the Jacobians at this point yields the same result for both systems, which can be written as

$$\mathbf{J_{vp}} = \mathbf{J_r} = \begin{bmatrix} 0 & 1 & 0\\ -\omega_n^2 & \frac{\mu}{m} & \frac{\theta}{m}\\ 0 & -\frac{\theta}{C_{\text{piez}}} & -\frac{1}{C_{\text{piez}}R_l}\end{bmatrix}. \tag{3.28}$$

Finding the complex conjugate pair of eigenvalues and solving for when the real parts are equal to zero with the bracketing method provides the value of θ at which the equilibrium returns to stability. Figure 3.2 demonstrates the methodology applied to investigate the accuracy of the method.

The operation of the method is demonstrated in Figure 3.3. Subplot (a) shows an example of non-dimensional displacement during a free oscillation transient. The corresponding cycle-averaged total energy is shown in subplot (b), which can be seen to grow from close to zero at the small displacement initial conditions to a constant value at the limit cycle, where oscillations are of constant amplitude. The time derivative of the cycle-

averaged total energy is demonstrated in subplot (c), which provides the prediction of the power which could be harvested at a particular oscillation amplitude. This can be seen to grow from a small value, when the oscillation amplitude is small, to zero on the limit cycle as the oscillations are no longer growing but with a maximum in between. This maximum is a prediction of the maximum cycle-averaged power which could be harvested with the system and the amplitude at which it occurs can be considered as the optimal operational amplitude in terms of output power.

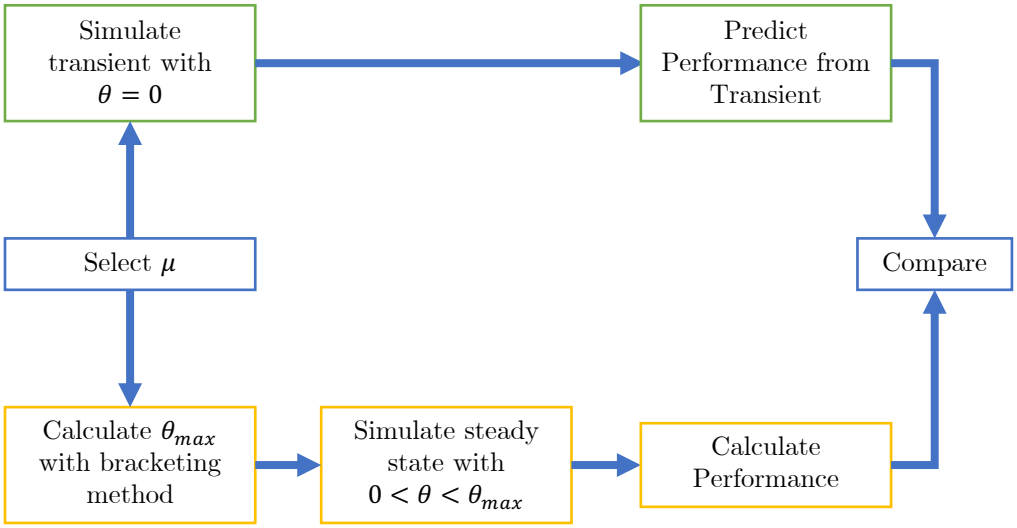

Figure 3.2: Illustration of simulation methodology for verification.

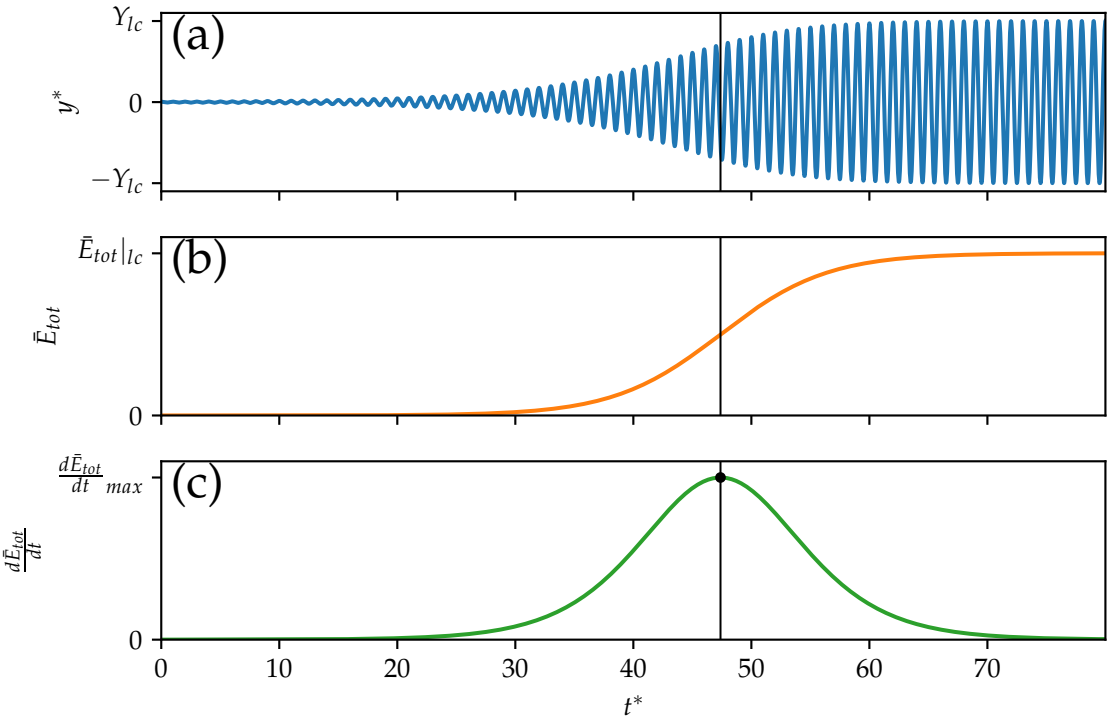

Figure 3.3: Illustration of extraction of performance from free transient. Time is normalised with the oscillation period, while Y_{lc} denotes the oscillation amplitude on the limit cycle.

3.4.3 Simulation Results and Comparison to Characterisation from Free Transient

In this section the simulation results obtained with the Van der Pol and Rayleigh oscillators are described and a comparison drawn between the prediction of output power from the free transient and the output power simulated under steady conditions with $\theta > 0$. Firstly, the trajectory of the limit cycle is considered. As the timescale difference between the conservative and nonconservative terms diminishes as the parameter μ is increased, limit cycle deformation becomes increasingly evident. Figure 3.4 shows the limit cycles formed by the system with both Van der Pol and Rayleigh nonlinearity and with no energy harvesting, hence $\theta = 0$, over a range of timescale separations as defined by μ. It is clear that in the case of the Van der Pol nonlinearity, as μ becomes greater than unity the limit cycle is deformed by stretching along the velocity axis resulting in the absolute velocity maxima no longer occurring at the zero displacement position. The resulting limit cycle trajectory diverges considerably from the undeformed circular sinusoidal trajectory evident at large timescale separations. The system with the Rayleigh nonlinearity exhibits similar behaviour, although the deformation of the cycle is less notable.

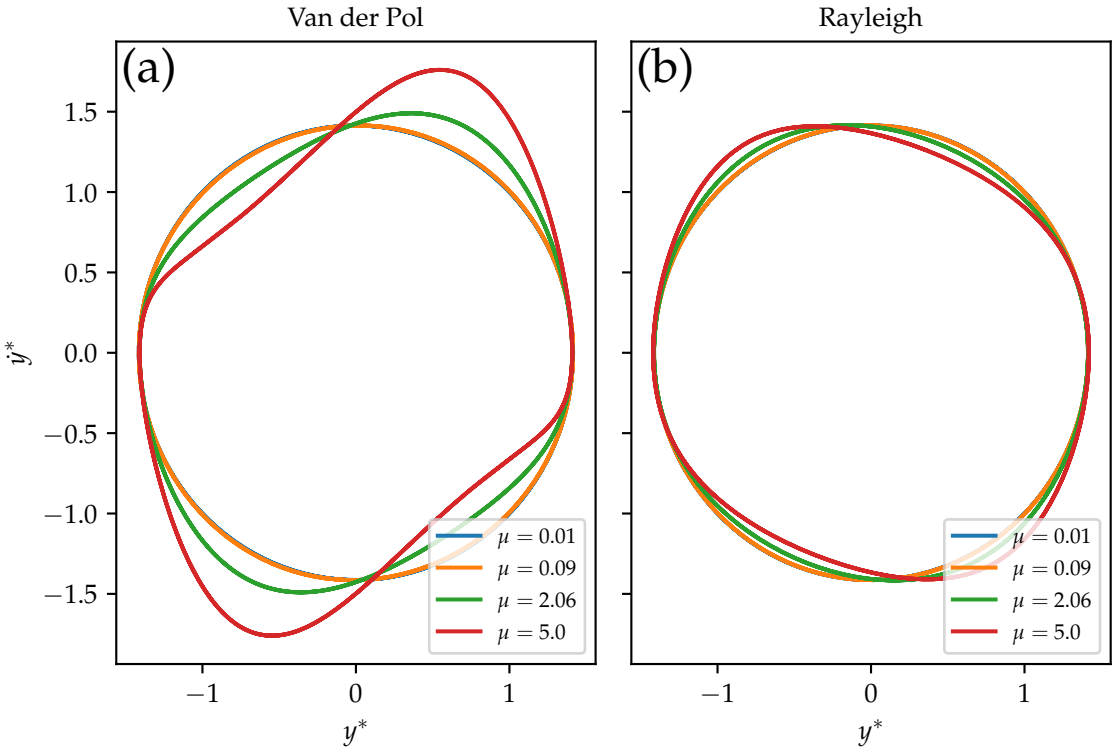

Figure 3.4: Limit cycles formed by the Van der Pol and Rayleigh systems with varying values of the parameter μ and with $\theta = 0$. y^* and $\dot{y}^*$ denote the displacement and velocity respectively as non-dimensionalised by their amplitudes measured by their standard deviations.

A comparison of the performance curves predicted from the free oscillation transients and those simulated with $\theta > 0$ is illustrated in figures 3.5 and 3.6 for the Van der Pol and Rayleigh oscillators respectively. As expected, when the timescale separation is large with small values of μ, the method accurately predicts the energy harvesting performance. However, as the magnitude of μ becomes close to order 1, the prediction from the free oscillation transient can be seen to underestimate the performance substantially. This is the case for both nonlinearities considered, although the error was worse when evaluated with the Van der Pol oscillator. As the timescale separation between the oscillation period and the transient becomes small the process of cycle averaging results in the smoothing of the growth rate of total energy, flattening the prediction of output power and hence underestimating the performance.

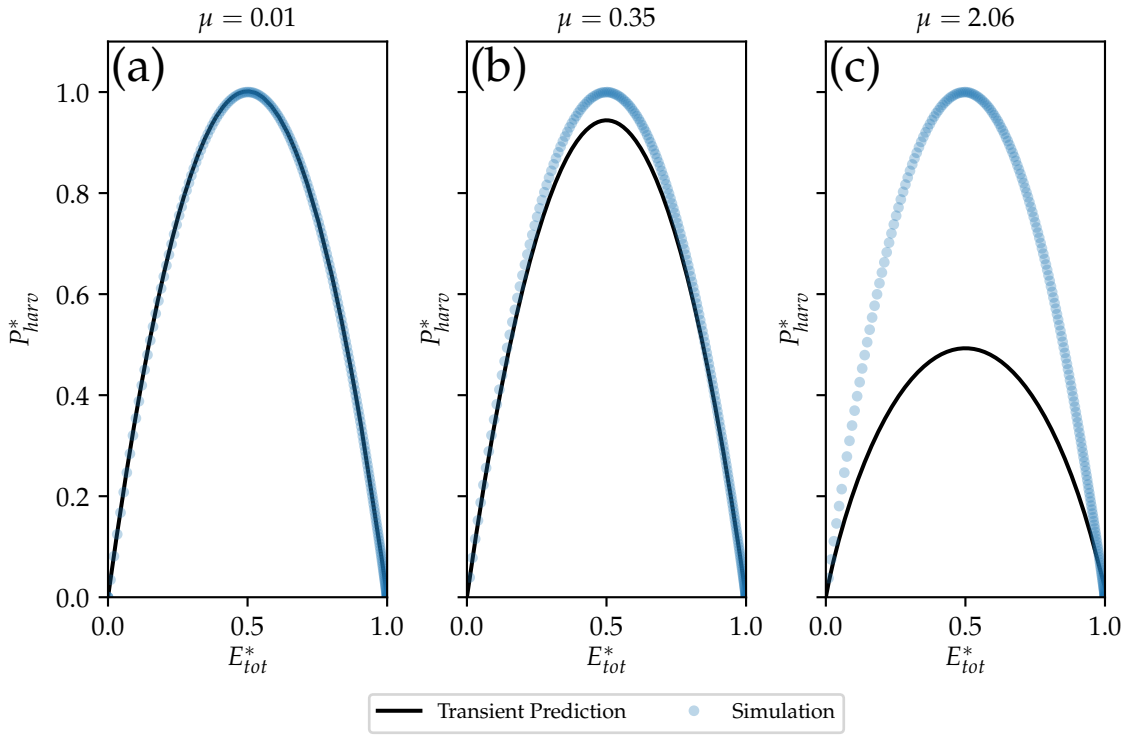

Figure 3.5: Comparison of simulated and predicted normalised output powers with Van Der Pol oscillator.

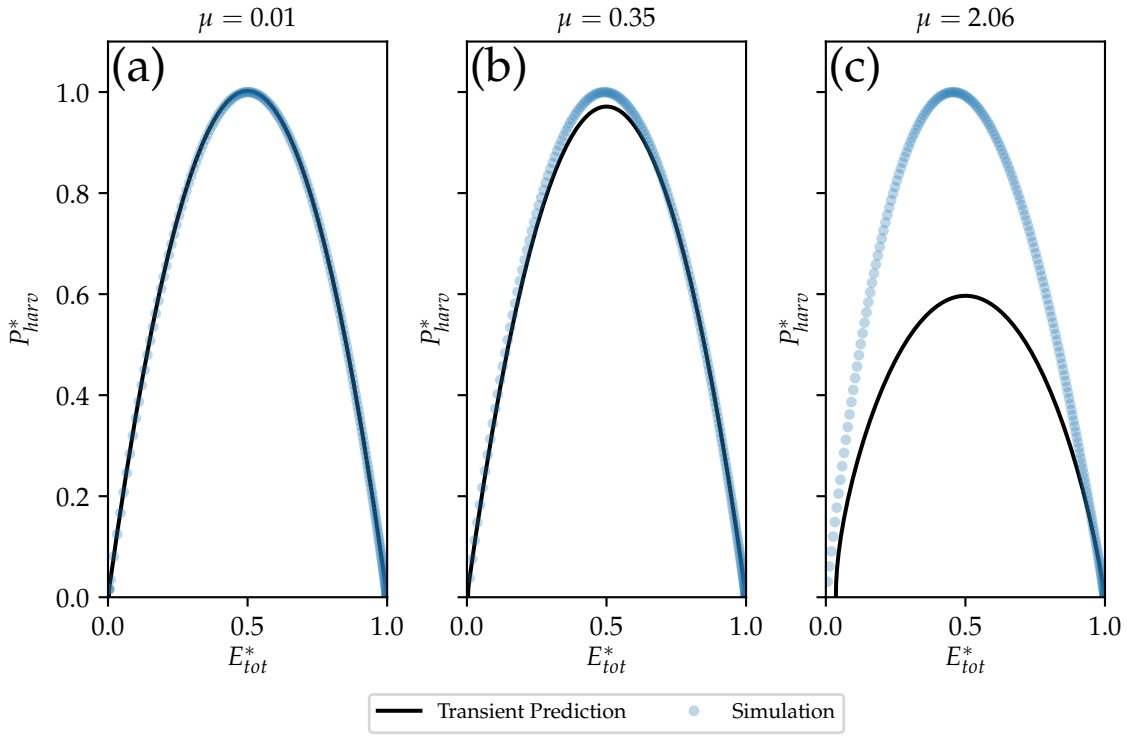

Figure 3.6: Comparison of simulated and predicted normalised output powers with Rayleigh oscillator.

Figure 3.7 represents the behaviour of both the mean and maximum relative error over the full range of μ assessed. The relative error ϵ_{rel} is defined as $\frac{\epsilon}{P_{\text{harv}}}$, where ϵ is the difference between the simulations with $\theta > 0$ and the predicted power. Observing the relative error with the parameter μ on logarithmic scales demonstrates close to linear behaviour over the evaluated region of timescales separations. This is especially true of the maximum relative error.

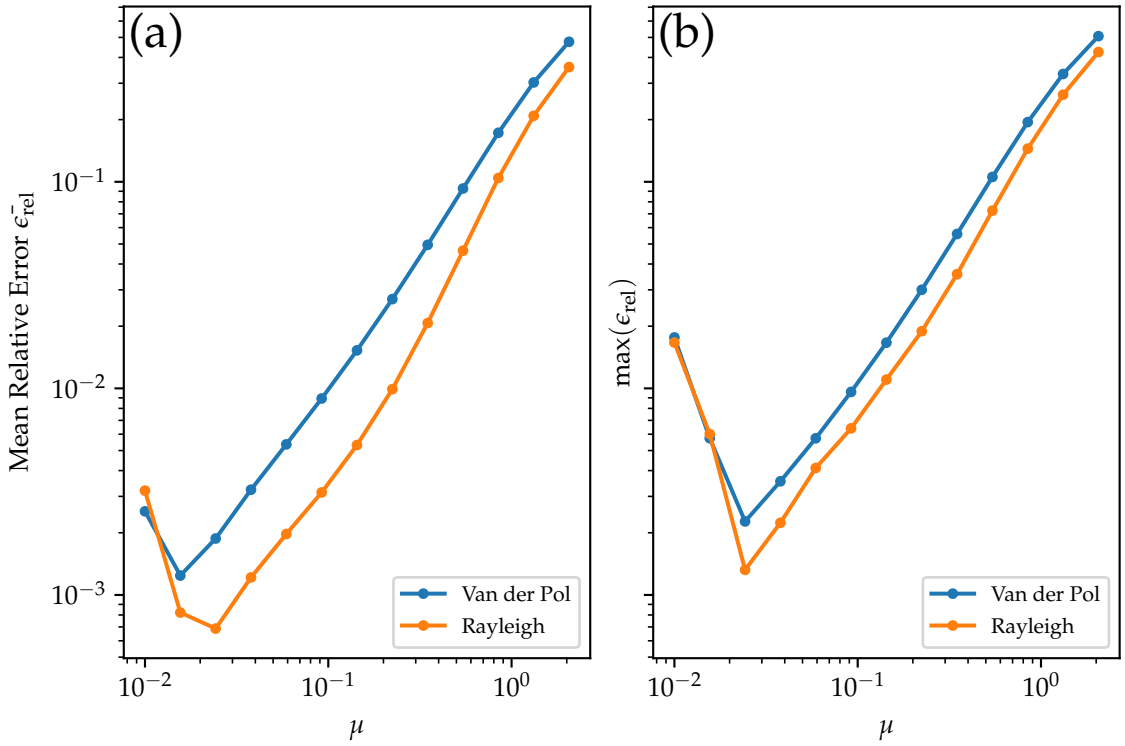

Figure 3.7: Comparison of relative error for harvesting from Van Der Pol and Rayleigh oscillators. Subplot (a) demonstrates the mean relative error, while subplot (b) shows its maximum value.

3.5 Application to the Galloping Oscillator

3.5.1 System Definition

Now that the method has been shown to be capable of accurately predicting energy harvesting performance with simple damping nonlinearities when the timescale separation is sufficient, the method can be applied to the galloping energy harvester. Compared to the Van Der Pol and Rayleigh oscillators, the quasistatic model of the galloping oscillator presents a more complex nonlinearity which results from the change of the aerodynamic forces acting on the tip geometry with the effective angle of attack α. Similarly to Abdelkefi et al [3], the model can be represented in terms of the dimensionless force coefficient C_y as

$$\ddot{y} - \frac{\rho A_f}{2m} C_y(\alpha)\left(\dot{y}^2 + U_\infty^2\right) + \frac{C_{damp}}{m}\dot{y} + \omega_n^2 y - \frac{\theta}{m}V = 0, \tag{3.29}$$

$$\dot{V} = -\frac{1}{C_{\text{piez}}}\left(\frac{V}{R_l} + \theta\dot{y}\right), \tag{3.30}$$

where ρ is the density of air, A_f is the frontal area of the tip geometry, m denotes the tip mass and U_∞ represents the freestream flow velocity. The mechanical damping in the system is defined by the damping coefficient C_{damp}. C_y is a function of the effective angle of attack α, which can be written as

$$\alpha = \tan^{-1}\left(\frac{\dot{y}}{U_\infty}\right). \tag{3.31}$$

$C_y(\alpha)$ is typically represented by a polynomial approximation in terms of $\tan(\alpha)$, which can be expressed as

$$C_y = \sum_{i=1}^{n} a_i \tan^i(\alpha) = \sum_{i=1}^{n} a_i \left(\frac{\dot{y}}{U_\infty}\right)^i. \tag{3.32}$$

As in Section 2.6 of Chapter 2, to simulate the model, the seventh-order odd termed polynomial approximation developed by Parkinson [79] was implemented, which describes the galloping of the square-prism. The seventh-order polynomial can be written as

$$C_y(\alpha) = a_1\left(\frac{\dot{y}}{U_\infty}\right) + a_3\left(\frac{\dot{y}}{U_\infty}\right)^3 + a_5\left(\frac{\dot{y}}{U_\infty}\right)^5 + a_7\left(\frac{\dot{y}}{U_\infty}\right)^7. \tag{3.33}$$

While the coefficients are tabulated in 2.3 presented in Chapter 2. The objective of simulating the quasistatic galloping energy harvester and comparing the predictions of the method with the simulation results with $\theta = 0$ was to verify the method with parameters which could be realistically be presented by an experimental system. The parameters where hence matched to the experimental study of Yang et al [108], which are presented in Table 3.2.

Parameter	Sym	Value (unit)
Mass	m	0.0301 (Kg)
Piezoelectric Capacitance	C_{piez}	90 (nF)
Load Resistance	R_l	0.259 (MΩ)
Natural Oscillation Frequency	ω_n	6.84 (Hz)
Tip Geometry Frontal Area	A_f	0.006 (m^2)
Air Density	ρ	1.225 ($\text{Kg}\,m^{-3}$)

Table 3.2: Galloping system parameters adopted from Yang et al [108].

3.5.2 Simulation Methodology

The methodology for the simulation of the galloping system was similar to that of the Van Der Pol and Rayleigh systems in Section 3.4 and was performed as demonstrated by the flow diagram in Figure 3.2. Similarly to when evaluating the Van Der Pol and Rayleigh systems, a linear stability analysis was required to determine the range of the electromechanical coupling coefficient with which the equilibrium is unstable, providing the range of θ with which to perform simulations. The galloping system has only a single equilibrium position at $y = 0$, $\dot{y} = 0$, $V = 0$. Evaluating the Jacobian at this point yields

$$\mathbf{J} = \begin{bmatrix} 0 & 1 & 0 \\ -\omega_n^2 & \frac{1}{m}\left(\rho A_f a_1 U_\infty - C_{damp}\right) & \frac{\theta}{m} \\ 0 & -\frac{\theta}{C_{\text{piez}}} & -\frac{1}{C_{\text{piez}} R_l} \end{bmatrix}. \tag{3.34}$$

Unlike in the case of the Van der Pol and Rayleigh oscillators where only stable limit cycles form, the galloping square-prism will form both unstable and stable limit cycles depending on the parameters. The formation of unstable limit cycles enables the existence of multiple stable cycles with the same parameter set. These can be obtained by varying the initial conditions, hence altering which limit cycle the system will evolve to. In this case two sets of initial conditions are simulated, one which corresponds to a large displacement and one which corresponds to a small pertubation from the equilibrium.

Further to investigating the accuracy of the method with the same sampling frequency as produced by the simulations, which may not always be obtainable by experimental means, the influence of the non-dimensional sampling frequency on the accuracy of the prediction was investigated. The non-dimensional sampling frequency f_s^* is defined as the average number of points per oscillation cycle, which can be estimated by $\frac{f_s}{2\pi\omega_n}$, where f_s is the sampling frequency. The simulated free transient was resampled using cubic spline interpolation and with a logarithmically spaced range of non-dimensional sampling frequencies. The prediction method was then applied to each of the resampled transients, yielding predictions with a range of non-dimensional sampling frequencies. These predictions could then be compared to results obtained from simulations with $\theta > 0$.

To provide a similar indication of the timescale separation as provided by μ in the Van der Pol and Rayleigh cases, the ratio of the aerodynamic forces to the restoring force can be estimated by

$$\upsilon = \frac{\rho A_f U_\infty^2}{2m\omega_n^2}. \tag{3.35}$$

3.5.3 Simulation Results and Comparison to Characterisation from Free Transient

As in Chapter 2, the coefficient of performance C_p was utilised to provide a non-dimensional measure of the efficiency of energy extraction from fluid flow, defined as

$$C_p = \frac{2P_{out}}{\rho A_{\text{swept}} U_\infty^3}, \tag{3.36}$$

where A_{swept} is the frontal area which the turbine blade travels through. In the case of the galloping energy harvester the swept area grows with the oscillation amplitude and can be written as

$$A_{\text{swept}} = 2A_y S + A_f, \tag{3.37}$$

where S is the span of the tip geometry. Further to the coefficient of performance, the tip speed ratio U_{tsr} can be defined as the ratio of the linear velocity amplitude to the freestream flow velocity,

$$U_{\text{tsr}} = \frac{A_{\dot{y}}}{U_\infty}. \tag{3.38}$$

A comparison of the simulated coefficient of performance with the predictions generated from the free oscillation transient is presented in Figure 3.8 with flow velocities across the full range experimentally investigated by Yang et al [108]. The method can be seen to accurately predict the coefficient of performance across the full range of experimental conditions, while stable limit cycles were not observed within the predicted unstable regions. This suggests that the regions predicted to relate to unstable limit cycles are likely to also be accurately predicted. Similarly to the Van der Pol and Rayleigh nonlinearities, the accuracy of the method decays as the timescale separation decreases. However, considering the timescale separation as estimated by υ, the timescale separation is above three orders of magnitude for the considered range of flow velocities and hence the method would be expected to be accurate in this range.

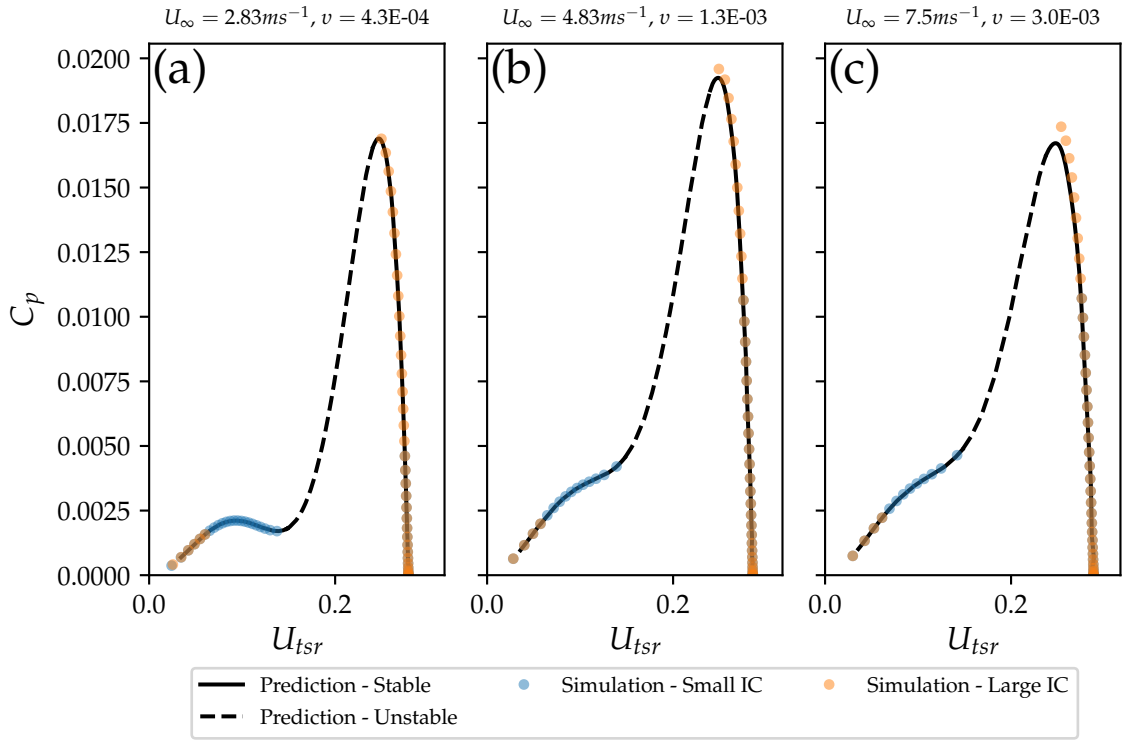

Figure 3.8: Comparison of simulated and predicted coefficient of performance for a galloping energy harvester. U_∞ denotes the freestream flow velocity, while v represents the ratio of the aerodynamic force to the restoring force.

The normalised prediction error obtained with varying non-dimensional sampling frequencies is presented in Figure 3.9. Over the evaluated region of flow velocities, the normalised error can be seen to increase close to linearly with flow velocity. The non-dimensional sampling frequency can also be seen to have little influence on the prediction error until it reaches values less than 6.4. This is a beneficial feature of the method as it is hence relatively insensitive to sampling frequency, which provides greater flexibility in the design of experiments with the aim of applying the method.

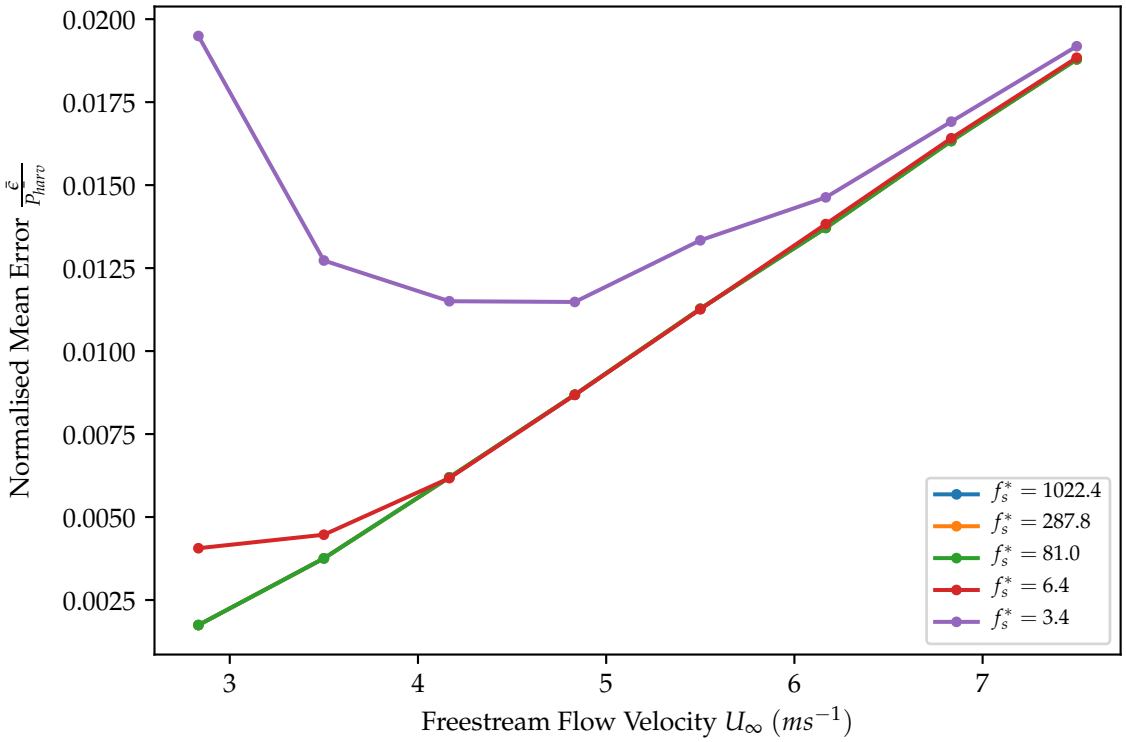

Figure 3.9: Normalised mean prediction error with flow velocity. A range of non-dimensional sampling frequencies are considered where f_s denotes the sampling frequency and $f_s^* = \frac{f_s}{2\pi\omega_n}$ is the non-dimensional sampling frequency, which can be considered as the average data points per oscillation cycle.

3.6 Summary

In this chapter a method for characterising the energy harvesting performance of a piezoelectric energy harvester which operates due to self-excited oscillations has been presented. The method has been verified with the simplest self-exciting nonlinearities, which form the Van der Pol and Rayleigh oscillators. As timescale separation is a required assumption in the development of the method, verification over a broad range of timescale separations has been performed with the simple nonlinearities. With sufficient timescale separation, the method has been shown to be capable of accurately predicting performance in these cases.

The method has then been applied to the quasistatic model for a galloping energy harvester, which presents a more complex nonlinearity. Taking realistic parameters of a device from the experimental study of Yang et al [108], the method has been shown to provide accurate predictions of performance over the full range of flow velocities. The influence of sampling rate has also been considered and shown to not significantly influence

the results unless the non-dimensional sampling rate is less than 6.4. The method could readily be expanded to cases with nonlinear stiffness and systems with additional degrees of freedom, however this is left for future work.

4

The Effect of Curvature on Harvesting Performance

4.1 Introduction

In Chapter 2 it was demonstrated that the attachment of the flow to the rear surface of the curved-blade tip geometry coincided with the existence of a higher amplitude branch and could enable higher energy harvesting efficiencies. However, curved-blades of only a single curvature were considered in the investigation. The curvature of the blade plays a key role in defining the dynamics of the flow structures formed around it and hence the potential efficiency of a device.

In this chapter the influence of curvature on the energy harvesting performance of the curved-blade galloping energy harvester is investigated experimentally. Rather than implementing a transduction mechanism, the energy harvesting performance is characterised from the growth of oscillations in the free oscillation transient by the method developed in Chapter 3, avoiding the influence of the particular implementation of the transduction mechanism on the results. To provide an insight into how the flow structures vary with the curved-blade curvature, smoke-wire flow visualisation is also performed.

4.2 Experimental Methodology

4.2.1 System Description and Experimental Setup

To apply the method developed in Chapter 3 to curved-blades with varying curvatures, a galloping oscillator was again constructed by mounting a 3D printed tip geometry to the end of cantilever beams. Dissimilarly to the configuration investigated in Chapter 2, in this chapter the tip geometry is mounted such that the cantilever beam is parallel to the flow direction. To stiffen the rotational degree of freedom of the curved-blade around the x axis, two cantilever beams were used to mount the tip geometry, one positioned at each end of the span. Figure 4.1 demonstrates the construction of the galloping oscillator. As the dynamics of the system were to be tracked by fluorescent marker motion tracking, three fluorescent markers were attached. The first two defined the locations of the tips of the curved-blade, while the third was mounted to the end of the cantilever beam on the side to be observed by the tracking camera. The oscillator could then be mounted into the low speed wind tunnel and aligned such that oscillations occurred in a direction perpendicular to the freestream flow direction. The orientation of the galloping oscillator with relation to the freestream flow direction is illustrated in Figure 4.1, as well as the positions of the fluorescent markers attached to track its position.

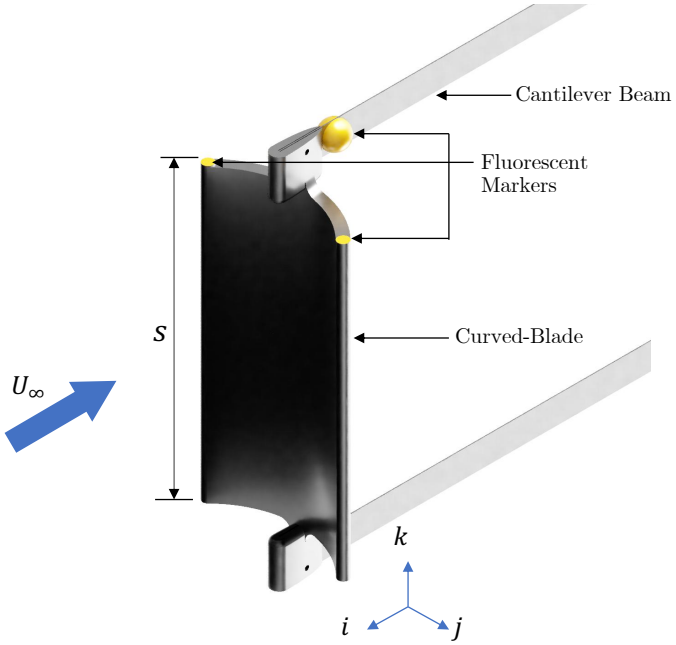

Figure 4.1: Illustration of galloping oscillator construction and orientation relative to the freestream flow direction. Oscillations result in the motion of the curved-blade in the i, j plane. U_∞ denotes the freestream flow velocity.

As in Chapter 2, the cross section geometry of the curved-blade was defined by a circular arc of base radius R and half-arc angle 2γ. The curvature could hence be defined by the half-arc angle γ as demonstrated in Figure 4.3. A range of angles from 90° to 25° were selected for the analysis. For a comparison to be made between blades of different curvature, the chord length, Ch, span, S, and thickness, th, of the blade where maintained constant between the geometries. The blade mass m_{tip} was also kept constant to ensure that the natural oscillation frequency was the same throughout the experiments. This was achieved by varying the infill percentage in the 3D printing process. The parameters of the experimental system are presented in Table 4.1.

The configuration of the experimental apparatus within the wind tunnel section is demonstrated by Figure 4.2. The cantilever beams were mounted with steel clamps onto a vertical clamping structure which enabled the galloping oscillator to be positioned at the centre of the test section. The camera and UV light required for the planar motion tracking system were positioned above the galloping oscillator, with the fluorescent markers located on the top side of the curved-blade. A pitot tube was positioned in front of the system and to the side of the test section to provide a measurement of the freestream flow velocity. The details of the motion tracking system and acquisition of the flow velocity measured with the pitot tube were as described in Chapter 2.

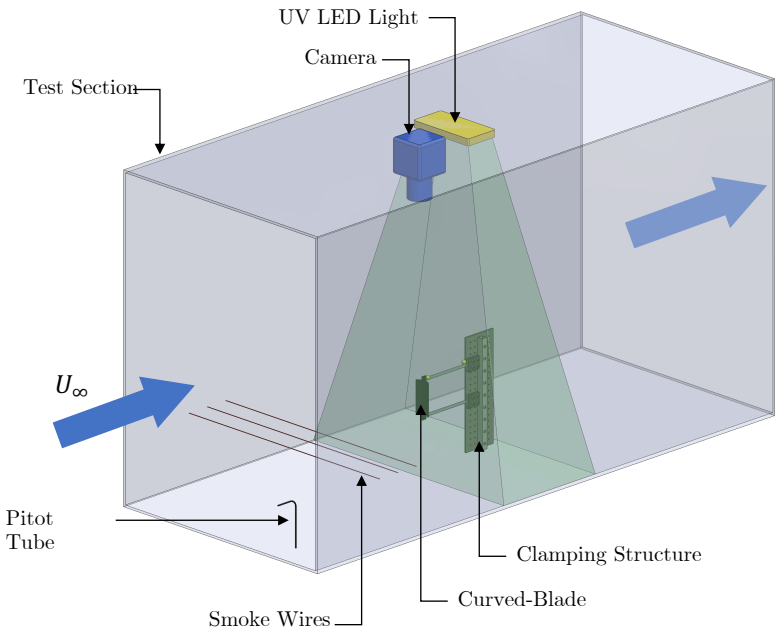

Figure 4.2: Illustration of experimental setup within the wind tunnel test section.

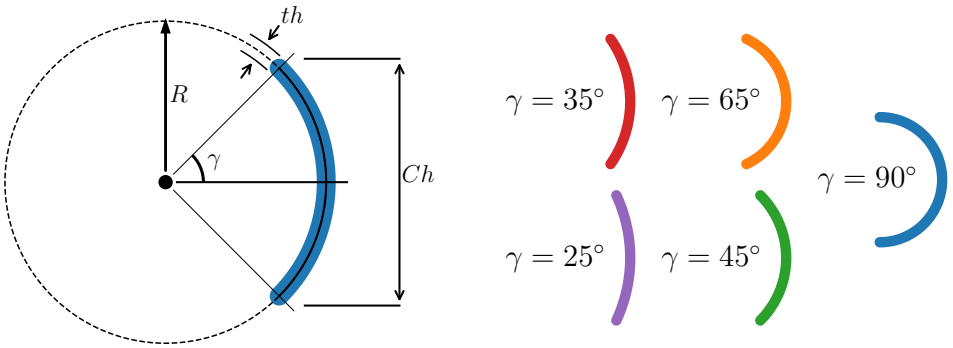

Figure 4.3: Definition of blade section geometry and illustration of selected range of curvatures.

4.2.2 Kinematics in the Parallel Cantilever Configuration

The mounting of the curved-blade such that the cantilever beam was parallel to the freestream flow direction, rather than perpendicular to it, had significant implications for the kinematics of the device. A comparison of the parallel and perpendicular configurations is

Parameter	Sym	Value (unit)
Blade Mass	m_{tip}	40 (g)
Natural Frequency	ω_n	19.7 (rads^{-1})
Blade Half-Arc Angle	γ	$25°, 35°, 45°, 65°, 90°$
Blade Base Circle Radius	R	$81, 60, 49, 38, 34$ (mm)
Blade Chord Length	Ch	68.75 (mm)
Blade Thickness	th	5 (mm)
Blade Span	S	138 (mm)
Beam Length	l_b	212 (mm)
Beam Width	w_b	12.5 (mm)
Beam Thickness	t_b	0.5 (mm)

Table 4.1: Parameters of experimental galloping oscillator with varying curvature.

demonstrated in Figure 4.4. In the perpendicular configuration, the linear velocity of the tip geometry varies along the span from the end mounted to the cantilever to the free end. When the aspect ratio of the tip geometry, defined as $AR = \frac{S}{Ch}$, becomes large and the rotation of the perpendicularly mounted tip geometry is significant, the aerodynamics cannot be assumed to be invariant with position along the span and three dimensional flow effects can become of importance.

In the parallel cantilever configuration, the effective angle of attack α is a function of both the linear velocity $\dot{y}$ and the angular position of the curved-blade as defined by the maximum slope angle of the beam ψ, rather than just the linear velocity, as is the case in the perpendicular configuration. As illustrated by Figure 4.5, the effective angle of attack in the parallel configuration can hence be written as,

$$\alpha = \tan^{-1}\left(\frac{\dot{y}}{U_\infty}\right) - \psi. \tag{4.1}$$

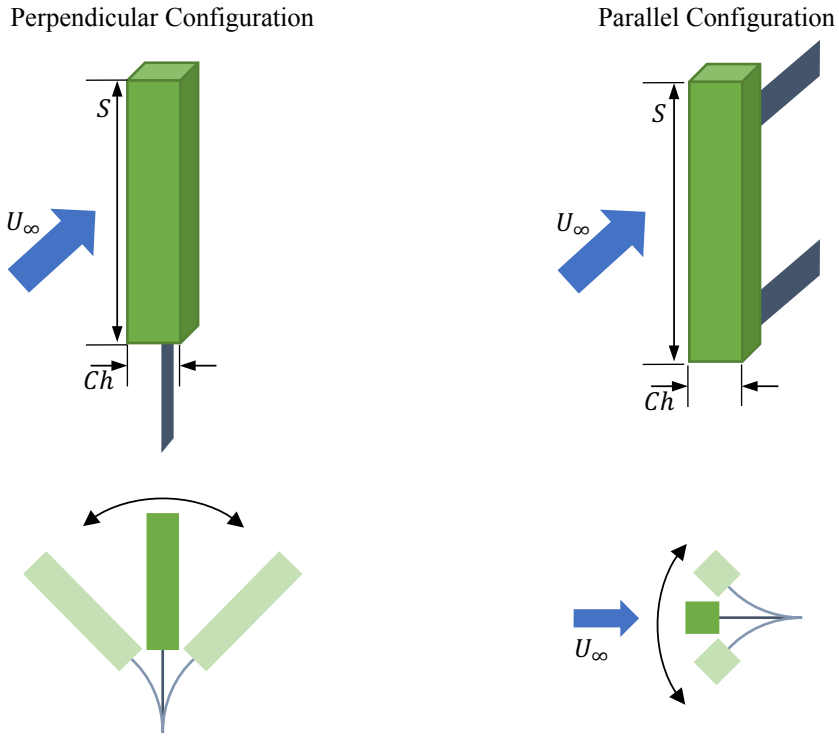

Figure 4.4: Illustration of perpendicular vs parallel configurations. The freestream flow velocity is denoted by U_∞. The span and chord length of the tip geometries are represented by S and Ch respectively. The black arrows demonstrates the direction of motion of the tip geometry.

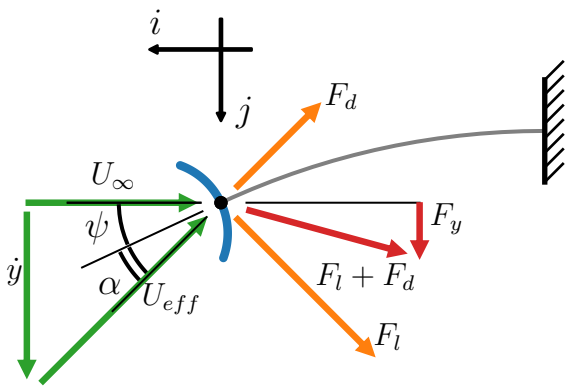

Figure 4.5: Illustration of velocity vectors and forces acting on blade. The blade is rotated by the maximum slope angle of the beam, ψ. U_{eff} denotes the effective flow velocity. The lift force and drag force are represented by F_l and F_d respectively, while the aerodynamic force projected in the j direction is denoted by F_y.

4.2.3 Measurement of System Dynamics and Prediction of Harvesting Performance

Once assembled within the wind tunnel test section, the system dynamics were measured and used to characterise the harvesting performance. The flow velocity within the wind tunnel was varied from $0.9\,\text{m}\,\text{s}^{-1}$ to $2.0\,\text{m}\,\text{s}^{-1}$ corresponding to chord length based Reynolds numbers of 4.0×10^3 and 9.0×10^3 respectively. At each flow velocity, once constant velocity conditions had been obtained, the curved-blade was released in a stationary position close to its equilibrium. This enabled the transient growth of the oscillations up to the limit cycle to be captured.

Figure 4.6 demonstrates an example of the prediction method described in Chapter 3 applied to an experimentally acquired free oscillation transient. Subplot (a) demonstrates the time series of the centre of mass displacement non-dimensionalised by the chord length, $y^* = y/Ch$. Time t^* is non-dimensionalised by the oscillation time period, $t^* = 2\pi\omega t$, and hence represents the oscillation cycle number. Subplot (b) presents the cycle-averaged total energy $\bar{E}_{\text{tot}}$. This can be seen to grow from zero, where there are no oscillations, to a constant value of $\bar{E}_{\text{tot}}|_{lc}$ on the limit cycle. The rate at which $\bar{E}_{\text{tot}}$ grows with time can be seen to be small at the start of the transient and small close to the limit cycle but with a maximum between. Subplot (c) illustrates the cycle-averaged time derivative $\frac{d\bar{E}_{\text{tot}}}{dt}$, which provides the estimate of energy harvesting performance. The amplitude at which cycle-averaged energy growth is fastest and hence the energy harvesting performance would

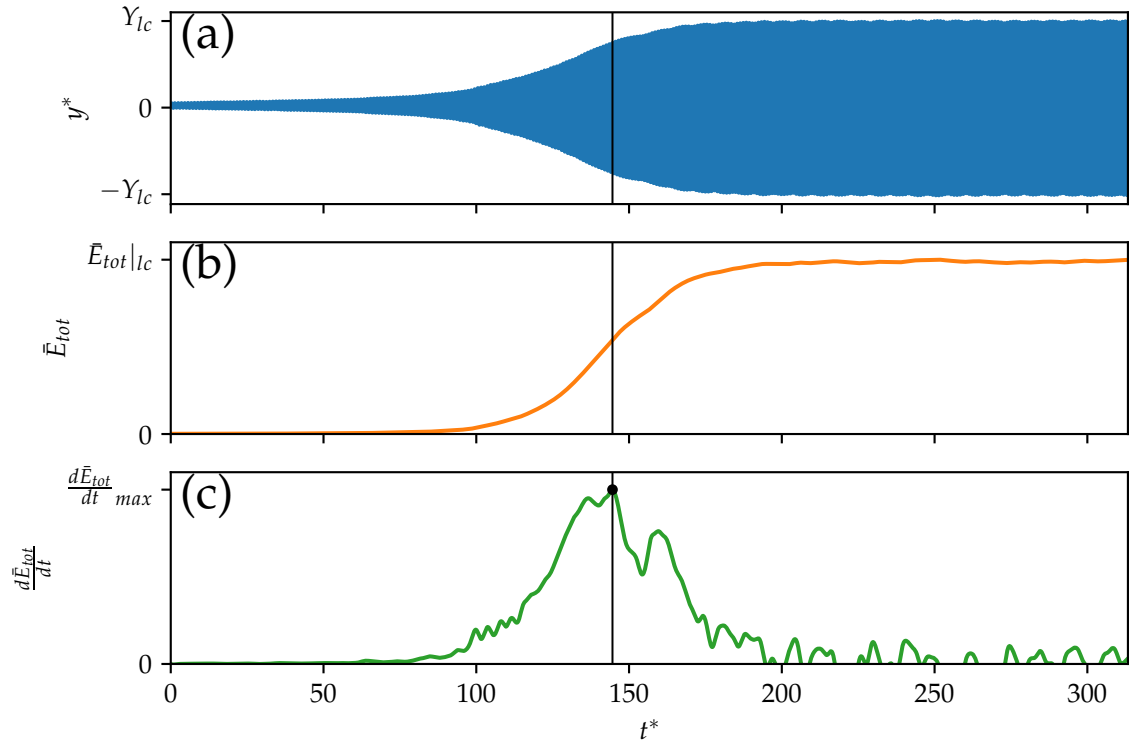

Figure 4.6: Example of extraction of performance from free transient. t^* denotes the time normalised with the oscillation period and hence represents the cycle number. Subplot (a) demonstrates the displacement of the curved-blade non-dimensionalised by chord length. The displacement amplitude and cycle-averaged total energy on the limit cycle are represented by Y_{lc} and $\bar{E}_{\text{tot}}$ respectively.

be greatest is marked by the black line.

4.2.4 Flow Visualisation

Similarly to the flow visualisation methodology presented in Chapter 2 Section 2.4, flow visualisations were obtained by application of the smoke-wire method with a twisted pair mounted horizontally across the wind tunnel test section. Figure 4.2 illustrates the location of the smoke-wire within the test section. To provide a more consistent illumination of the smoke filaments, the smoke was illuminated by two LED arrays positioned outside of the test section. This ensured smoke was visible even when deflected significantly in the vertical direction. Images were captured with a Phantom high speed camera with a frame rate of 600 fps and a resolution of 1152 $\times$ 896 pixels.

4.3 Experimental Dynamics and Estimated Harvesting Performance

4.3.1 Steady-State Dynamics

In capturing the growth of the oscillations from a small perturbation close to the equilibrium to the limit cycle, the steady-state behaviour at the limit cycle is also acquired and provides some insight into the underlying dynamics. Figure 4.7 illustrates the steady-state limit cycle amplitudes as measured by their standard deviations. Subplot (a) shows the displacement amplitude, which is non-dimensionalised with chord length and hence, $A_y^* = \frac{A_y}{Ch}$. The angle of attack amplitude is demonstrated in subplot (b), while the maximum tip speed ratio is shown in subplot (c). The tip speed ratio is defined as the ratio of the linear velocity of the blade to the freestream flow velocity. This can be considered as both an instantaneous value u_{tsr} or a cycle maximum value of U_{tsr},

$$u_{\text{tsr}} = \frac{\dot{y}}{U_\infty}, \quad U_{\text{tsr}} = \frac{A_{\dot{y}}}{U_\infty}. \tag{4.2}$$

The amplitudes are plotted against reduced velocity, which is defined as $U^* = \frac{2\pi U_\infty}{\omega_n Ch}$, where ω_n denotes the natural frequency and Ch is the chord length of the blade.

For all the investigated curvatures, large amplitude galloping oscillations occur only after the region of vortex-induced vibrations which exists around the reduced velocity of $\frac{1}{St}$. This suggests that unsteady vortex forcing may have delayed the onset of galloping oscillations, possibly by a similar mechanism to as observed by Mannini et al with the rectangular prism geometry [69]. The amplitude of the limit cycles can be seen to decrease with half-arc angle γ, with the smallest oscillations consistently observed with the 90° half-arc angle geometry.

For all of the considered geometries, it is noticeable that tip speed ratio amplitude U_{tsr} appears to tend to a constant value with reduced velocity. It can be shown that in the case of a galloping oscillator where the angle of attack is a function of u_{tsr} only with $\alpha = \tan^{-1}(u_{\text{tsr}})$ and the cantilever beam orientated perpendicular to U_∞, the amplitude U_{tsr} on the limit cycle will become constant with reduced velocity as aerodynamics dominates the influence of mechanical damping. This has also been demonstrated experimentally in previous investigations of the galloping curved-blade [97]. As Figure 4.7 shows a similar behaviour, it can be suggested that the most significant period of power flow, which defines the limit cycle amplitude, occurs when ψ is close to zero. This would hence provide a similar dependence of U_{tsr} on U^* as when α is a function of u_{ts} only, where the deflection of the beam does not result in a rotation of the tip geometry which contributes to the angle of attack.

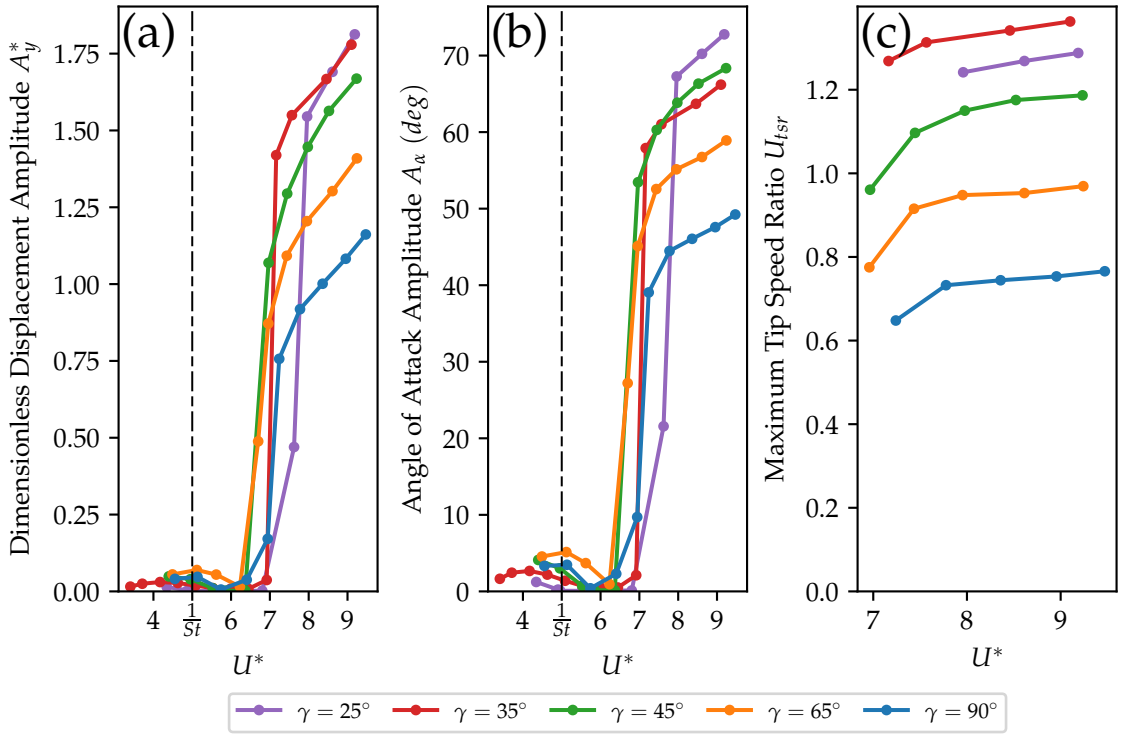

Figure 4.7: Steady-state amplitude behaviour with reduced velocity. Subplot (a) shows the displacement amplitude, which is non-dimensionalised with chord length and hence, $A_y^* = \frac{A_y}{Ch}$. The angle of attack amplitude is demonstrated in subplot (b), while the maximum tip speed ratio is shown in subplot (c).

Examples of the limit cycle trajectories obtained with a 45° half-arc angle curvature are illustrated in Figure 4.8. Subplot (a) demonstrates the y position and velocity of the curved-blade. The black ellipses illustrate ideal sinusoidal trajectories of equivalent amplitude. As the trajectories are close to the ellipses, they can be considered near sinosoidal. Subplot (b) illustrates how the angle of attack varies with the tip speed ratio on the steady-state limit cycle at a number of different reduced velocities. The cycles tend to a constant value at the u_{tsr} maxima, which is consistent with the tending of U_{tsr} to a constant value in figure 4.7. The maximum values of α occur below the maximum value of u_{tsr} and hence correspond to the combined influence of both beam deflection and the velocity of the blade.

4.3.2 Predicted Harvesting Performance

Now the steady-state behaviour of the curved-blades with different curvatures has been described, the analysis can progress to the harvesting performance predictions obtained by application of the method outlined in Chapter 3. Figure 4.9 demonstrates the predic-

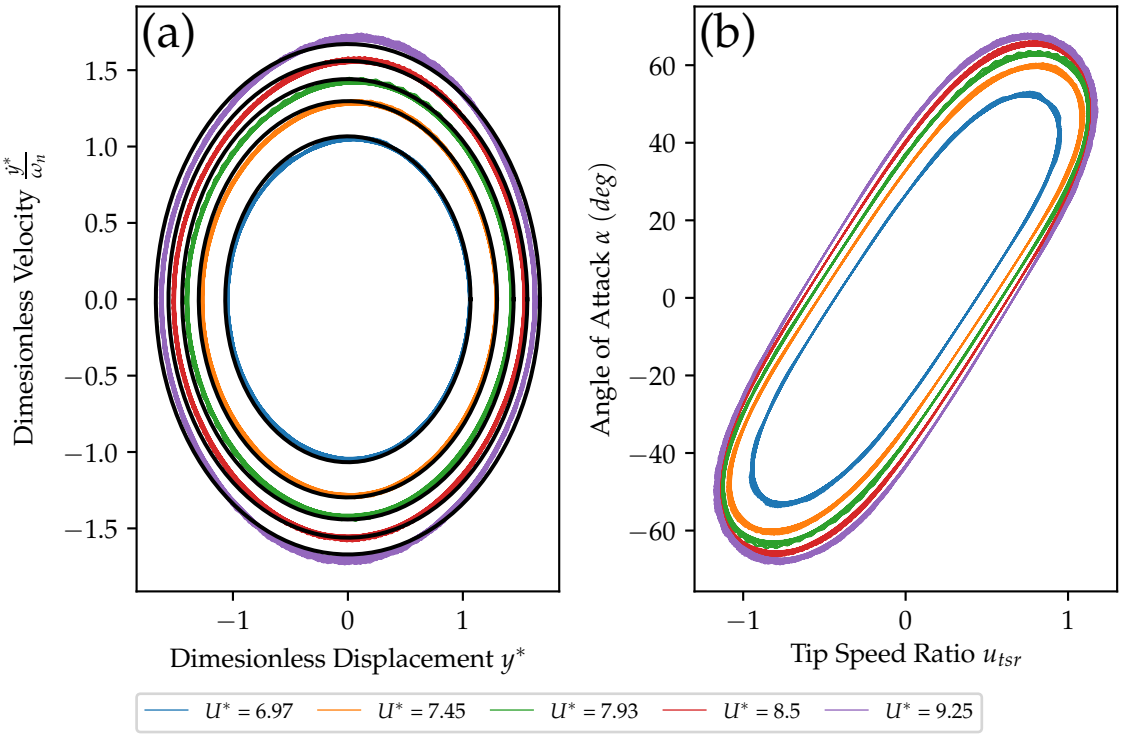

Figure 4.8: Limit cycle trajectories with $\gamma = 45°$ over a range of reduced velocities. Subplot (a) shows the displacement and linear velocity of the blade non-dimensionalised as $y^* = \frac{y}{Ch}$ and $\dot{y}^* = \frac{\dot{y}}{Ch\omega}$ respectively. The black lines represent ideal sinosoidal trajectories based on each of the displacement amplitudes. Subplot (b) illustrates the relationship between the tip speed ratio and effective angle of attack throughout an oscillation cycle.

tions obtained with the varying curvature geometries. The dependence of the coefficient of performance C_p on the tip speed ratio for the different geometries considered is presented in subplot (a). Results obtained at three different reduced velocities are shown, as illustrated by dotted, dashed and solid lines. The characterised performance was found to vary significantly with the oscillation amplitude, which is illustrative that careful design of a transduction mechanism would be required to ensure that a device operated close to the most efficient amplitude. The 35°, 45° and 65° geometries can be seen to significantly outperform the other two. The curves for the three different reduced velocities also appear to be close to collapsing, especially for the 45° and 65° curvatures. This collapse would be expected in the case where the cantilever beam is perpendicular to U_∞ and hence suggests that the most significant point for power flow within the cycle is when ψ is close to zero.

The variation of the C_p maximum with reduced velocity is illustrated in subplot (b) of Figure 4.9 for the different curvature geometries. The 35°, 45° and 65° geometries can be seen to considerably outperform the other two geometries for all considered reduced

velocities. The leading of the three varied with reduced velocity, with the 35° geometry performing best a low reduced velocity, while at high reduced velocity the 65° was best. A large drop in estimated C_p occurred for the 90° geometry around a reduced velocity of 8.5 and requires further investigation.

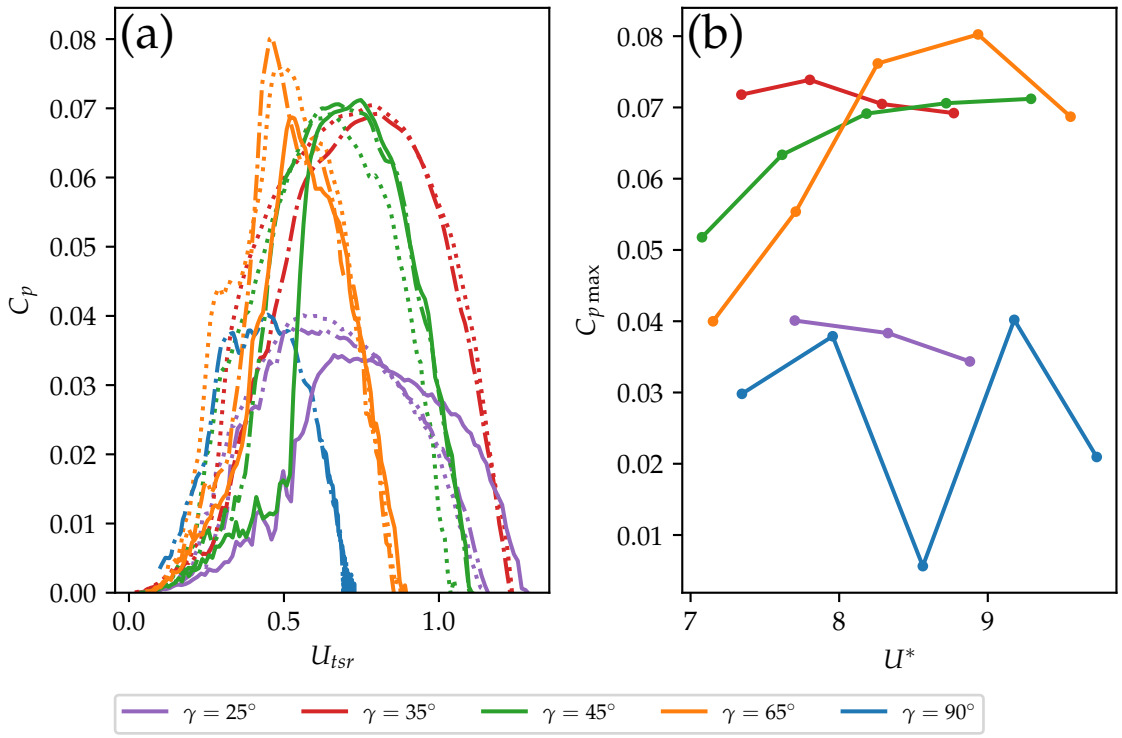

Figure 4.9: Predicted coefficient of performance for the range of considered curvatures. Subplot (a) illustrates the variation of coefficient of performance with maximum tip speed ratio U_{tsr}. Dotted lines represent results acquired at a reduced velocity of 8.0, dashed lines at a reduced velocity of 8.7 and solid lines at reduced velocity of 9.3. Subplot (b) demonstrates the relationship between the maximum predicted coefficient of performance and reduced velocity.

4.4 Flow Visualisations

4.4.1 Zero Displacement Position

Flow visualisations for the four considered curvatures are illustrated in Figure 4.10 at a reduced velocity of 8.4. The blade is viewed from above, with the freestream flow direction in the upward direction. The blade is close to its zero displacement position and is traveling from left to right. The colourmap represents the pixel intensities obtained from

the monochrome Phantom high speed camera and hence the smoke density, and is used to improve the clarity of the visualisations, with light yellow displaying the highest density, whilst the lowest is shown as a dark blue colour. The twisted wires generated a series of filaments of smoke, rather than a continuous sheet. These filaments of smoke represent streaklines, defined as the loci of points of all the fluid particles which have passed through a particular point in the past, and are clearly illuminated in Figure 4.10. When unperturbed by the presence of the blade, the streaklines appear straight, reflecting only the freestream uniform flow. This is evident in the right hand side of the visualisations. Closer to the blade the streaklines are deflected significantly. The deflection of the streaklines in the left direction on the rear surface of the blades is illustrative of the generation of a force in the y direction acting on the blade. Dark blue regions in the visualisations illustrate areas where the smoke is well mixed due to higher vorticity in these areas.

In subplot A, which relates to the least curved geometry with a half-arc angle of 25°, leading edge separation is evident as well as the formation of a large leading edge vortex (LEV). In subplots B, C and D, which relate to the higher performing 35°, 45° and 65° half-arc angle geometries, leading edge flow separation is not evident and the flow appears to be attached for the majority of the chord length. Subplot E demonstrates the geometry with the highest curvature, relating to a half-arc angle of 90°. In this case the separation point is close to the leading edge resulting in the formation of a large wake.

It can hence be concluded that the attachment of the flow to the rear surface of the blade allows the 35°, 45° and 65° half-arc angle geometries to outperform the others considered. The formation and shedding of a leading edge vortex during each half-oscillation was evident for the 25°, 35° and 45° and 65° cases and could provide a lift enhancement in these cases by similar mechanisms to as has been shown to occur in flapping flight [31, 72]. However, the unsteady forces relating to the leading edge vortex and how they relate to energy harvesting performance requires further investigation.

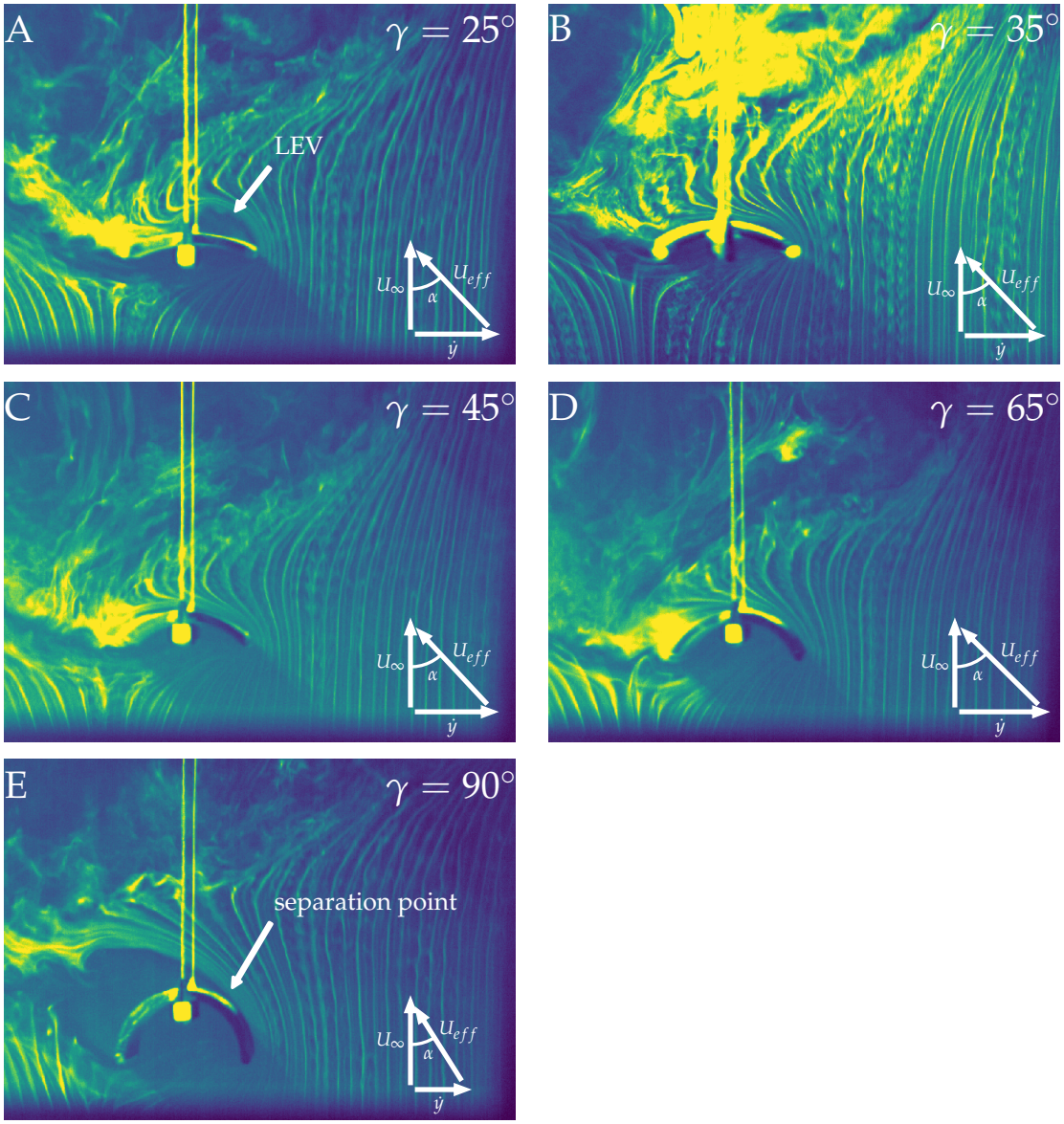

Figure 4.10: Flow visualisations with different curvatures. Reduced velocity $U^* = 8.4$. The colourmap represents the pixel intensity values obtained from the monochrome Phantom high speed camera. The flow can be seen to be attached to the rear surface of the blade in B, C and D but not in A and E .

4.4.2 Full Oscillation Cycle: 45° Half-Arc Angle Geometry

Although the flow structures at the maximum velocity position are of great importance in determining the potential efficiency of the device, significant insight into the underlying mechanisms defining the fluid-structure interaction can be gained by observing the flow

structures across an oscillation cycle. Figure 4.13 demonstrates flow visualisations at six different time instances across half an oscillation period with the 45° half-arc angle geometry. The positions of the time instances on an oscillation cycle of equivalent amplitude are also illustrated in terms of both non-dimensionalised displacement and velocity, as well as tip speed ratio and effective angle of attack. The oscillation amplitude is close to its value at the predicted C_p maximum and is hence representative of best performing case for the particular curvature.

As in Figure 4.10, the blade is viewed from above, with the freestream flow direction in the upward direction. The first time instance, denoted by (1) in Figure 4.13, is close to the maximum tip speed ratio instance, while slightly passed the maximum effective angle of attack. In the 45° case the flow can be seen to be attached at this point. As the linear velocity of the curved-blade then begins to drop in conjunction with the tip speed ratio and effective angle of attack, the flow can be seen to separate from the leading edge, resulting in the formation of a leading edge vortex. The leading edge vortex continues to grow in size as the linear velocity and effective angle of attack continue to fall as illustrated in time instance (3) in Figure 4.13. Between time instances (3) and (4) the effective angle of attack followed by the linear velocity of the blade change sign, coinciding with the shedding of the leading edge vortex from the rear face of the blade. Leading edge separation is not evident in either (4) or (5) and the flow returns to its attached state between these two time instances. The blade finally returns to its maximum velocity position, although now travelling in the opposite direction at time instance (6).

Some further insight can be gained by applying Kelvin's circulation theorem, which states that for an inviscid fluid, the circulation around a closed loop containing the same fluid elements must remain constant [58]. Although the flow is not inviscid, viscous effects are largely confined to the boundary layer. The total circulation can be evaluated as the sum of the contributions of the individual fluid elements including the circulation of the vortices present in the wake, the leading edge vortex and the bound circulation generated around the curved-blade, stated mathematically as

$$\frac{d\Gamma}{dt} = 0, \tag{4.3}$$

where Γ is the circulation contained within the enclosed region. An important time period of interest is when the flow becomes attached to the rear face of the blade, such as between time instances (4) and (6) in Figure 4.13. In this region the angle of attack and bound circulation are growing and hence to balance the bound circulation growth, a series of small vortices are shed into the wake. A clear example of these vortices was observed with the 35° half-arc angle geometry, which is illustrated in Figure 4.11. An illustrative representation of the bound vorticity and small wake vortices at this time instance is presented in subplot

(a) of Figure 4.12. Once the blade begins to decelerate and the angle of attack begins to fall, the bound circulation will also decrease. In this period, corresponding to time instances (1) to (3) in Figure 4.13, the leading edge vortex can be seen to appear and grow rapidly, suggesting that the decreasing bound circulation is balanced by the growth of the leading edge vortex. As the direction of travel of the curved-blade reverses each half-oscillation, so must the bound circulation. From this is can be inferred that a time instance exists in which the bound circulation around the curved-blade is zero. At this time instance, which is likely to occur between time instances (3) and (4) in Figure 4.13 when the angle of attack is small, the circulation of the leading edge vortex must balance the circulation of the vortices shed into the wake of the curved-blade since the previous change in direction of the curved-blade. Subplot (b) of Figure 4.12 demonstrates this time instance.

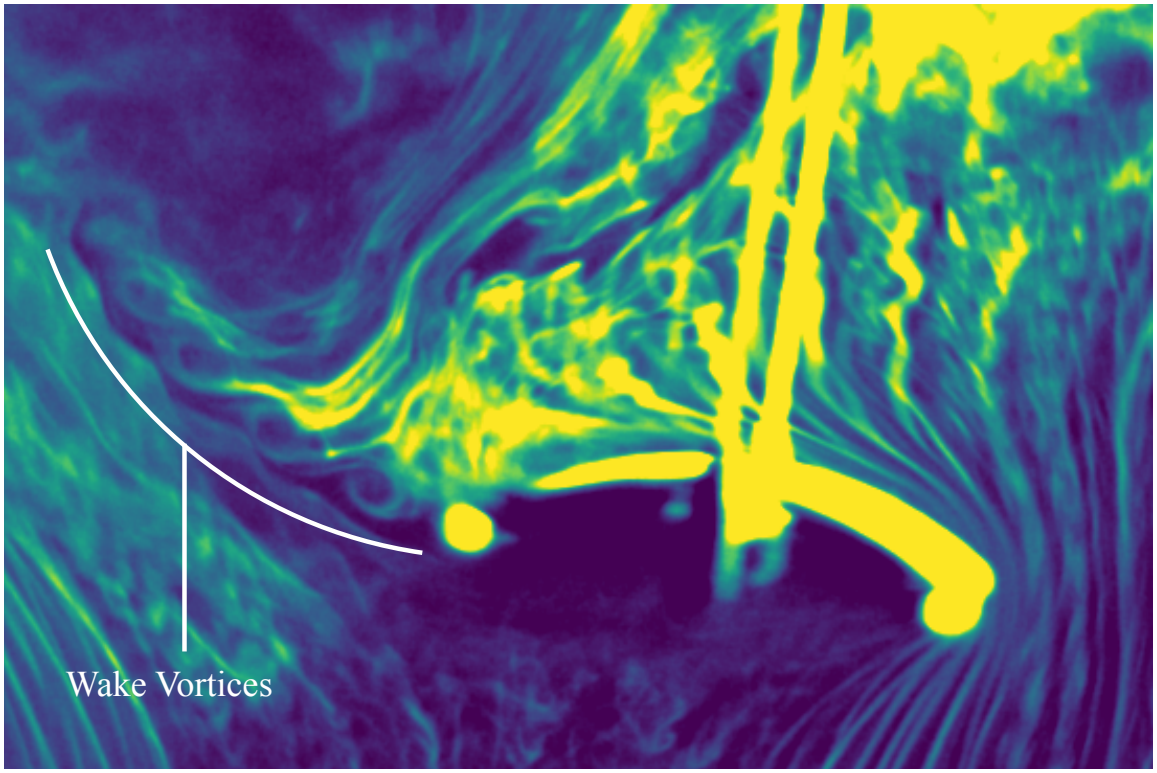

Figure 4.11: Small vortices shed into the wake with the 35° curvature geometry. The curved-blade is moving from left to right and is approaching its maximum velocity position. The free stream velocity is in a vertically upward direction.

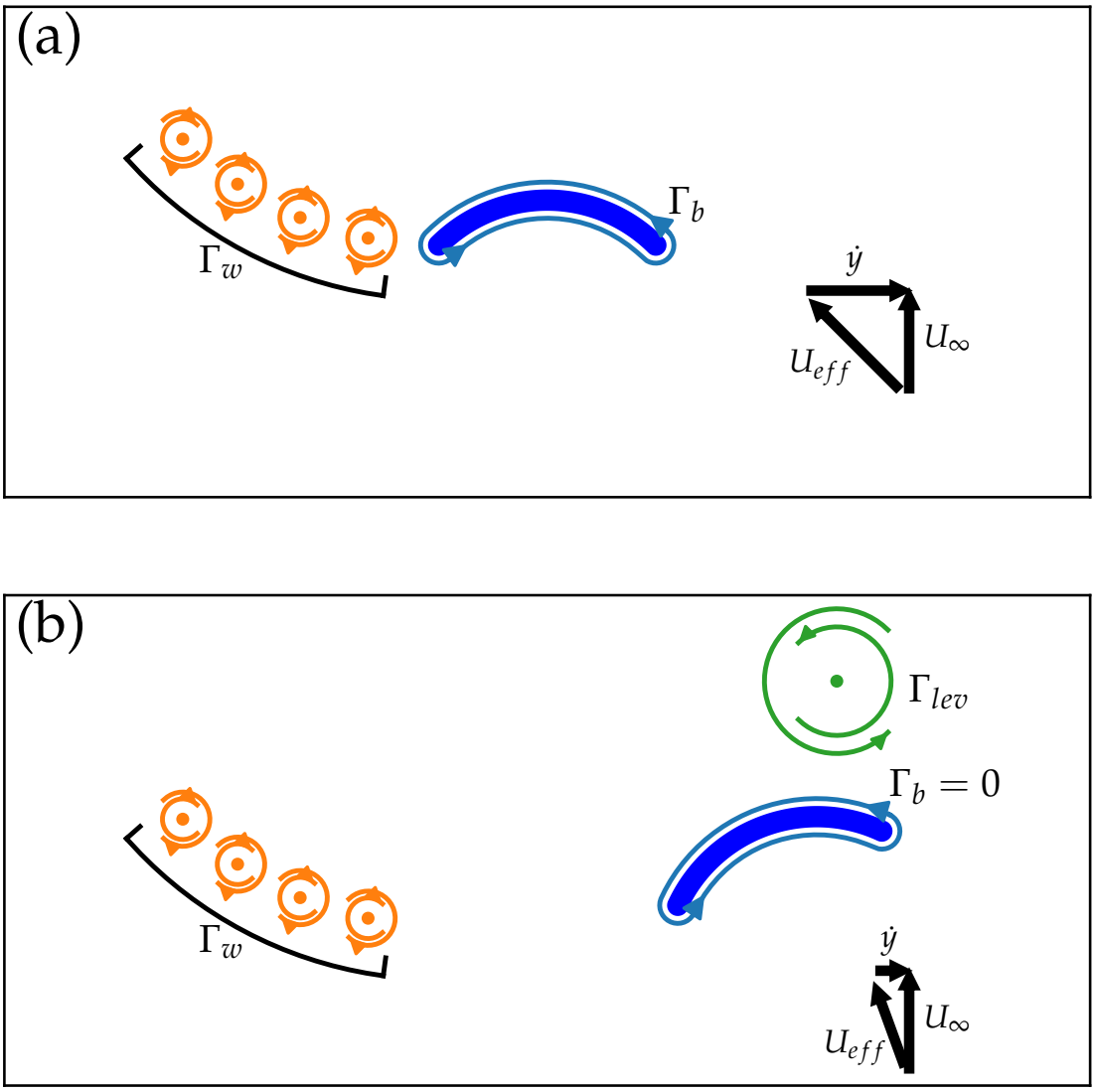

Figure 4.12: Fluid elements and their circulations at two different time instances within an oscillation cycle. Γ_w denotes the circulation in the vortices shed into the curved-blade wake, Γ_b is the bound circulation around the boundary of the curved-blade and Γ_{lev} represents the circulation of the leading edge vortex.

Figure 4.14 illustrates a comparison of the flow visualisations obtained with the 45° curvature geometry at a three different oscillation amplitudes. The predicted coefficient of performance is also shown versus the amplitude of tip speed ratio to provide context of the oscillation amplitudes displayed. The shape of the C_p vs U_{tsr} curve for the 45° curvature is characterised by a region of low C_p when U_{tsr} is small, followed by a broad peak of C_p where the optimal performance is obtained. The first series of flow visualisations relate to the edge

of the low C_p region. At this tip speed ratio amplitude, the flow can be seen to separate from the leading edge at all time instances throughout the oscillation cycle, resulting in the formation of a large wake.

The second series of flow visualisations displayed in Figure 4.14 relate to a tip speed ratio amplitude close to the C_p maximum. The flow visualisations now show the flow to become attached as the curved-blade approaches its maximum velocity position. The comparison between this case and the lowest amplitude case illustrated in subplot (A) therefore suggests the peak in C_p can at least in part be associated with the attachment of the flow.

The final series of flow visualisations in Figure 4.14 illustrate the behaviour when the oscillation amplitude has reached the limit cycle, hence the growth rate of oscillations and subsequently the predicted performance are zero. In this case the flow can also be seen to become attached during each half-oscillation, while a leading edge vortex is again formed and shed as the curved-blade decelerates and changes direction. Although there is no notable qualitative difference in the flow visualisation between the close to maximum C_p and limit cycle cases, as the amplitude is larger there will be greater losses to mechanical damping on the limit cycle. In addition, the kinematics act to limit the performance through the projection of the forces. As the linear velocity of the curved-blade becomes large, the projection of the aerodynamic forces in the direction of motion becomes dominated by the drag force, which acts in an opposing direction to the velocity and is hence negative towards the performance. The combination of these two effects is likely the cause of the limiting of the growth of oscillations and hence the predicted performance.

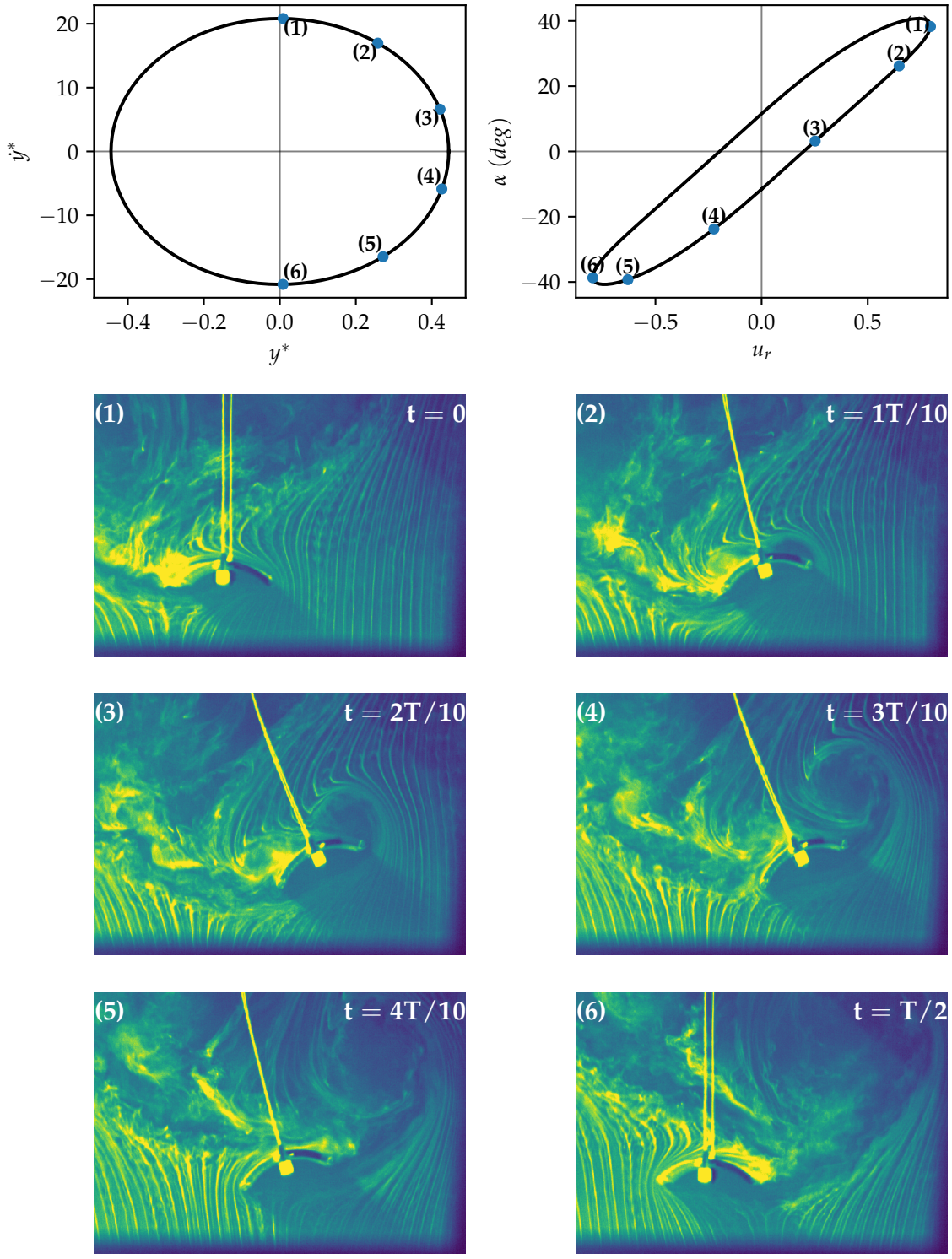

Figure 4.13: 45° half-arc angle geometry flow visualisations close to C_p maximum. Reduced velocity $U^* = 8.4$. The colourmap represents the pixel intensity values obtained from the monochrome Phantom high speed camera. Visualisations at six equally spaced time instances, denoted by (1) to (6) are shown with their corresponding locations in an oscillation cycle of equivalent amplitude demonstrated by the plots of $\dot{y}$ vs y and α vs u_{tsr}

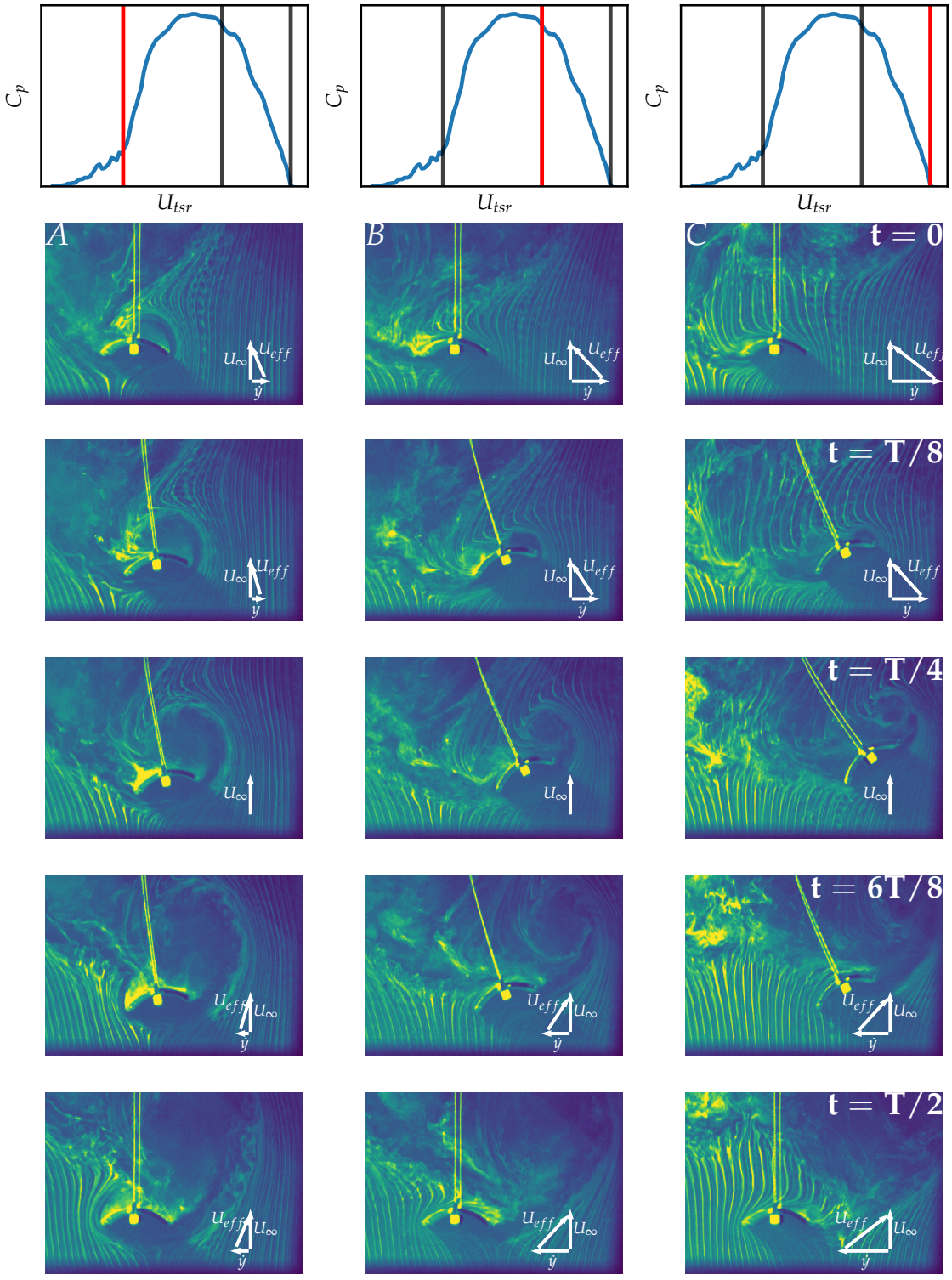

Figure 4.14: Flow visualisations with the 45° half-arc angle geometry at different oscillation amplitudes. Reduced velocity $U^* = 8.4$. The colourmap represents the pixel intensity values obtained from the monochrome Phantom high speed camera.

4.4.3 Full Oscillation Cycle: Comparison of Geometries

The blades of different curvatures presented pronouncedly varying performances as demonstrated by Figure 4.9. This is especially evident when comparing the least and most curved 25° and 90° half-arc angle geometries with the middle cases, such as the 45° geometry. Figure 4.15 demonstrates flow visualisations of this comparison at five different time instances across half of an oscillation cycle. The oscillation amplitudes are close to their values at the predicted C_p maximum for each of the geometries and are therefore representative of best performing cases. Comparing the 25° and 45° geometries, a clear distinction can be made in that leading edge separation was not observed at the maximum velocity position with the markedly better performing 45° geometry, whereas it can clearly be seen to occur prior to the maximum velocity position in the 25° case. In addition, the leading edge vortex can be seen to grow to a larger size in the 25° case before it is eventually shed.

With the 90° half-arc angle geometry, although leading edge separation does not take place, the separation point is consistently close to the leading edge and results in the formation of a large wake. This wake is likely to correspond to relatively large drag forces when compared to the higher performing geometries, which would have limited the performance. As leading edge separation does not take place outside of the change of direction of the curved-blade, a leading edge vortex does not form in this case.

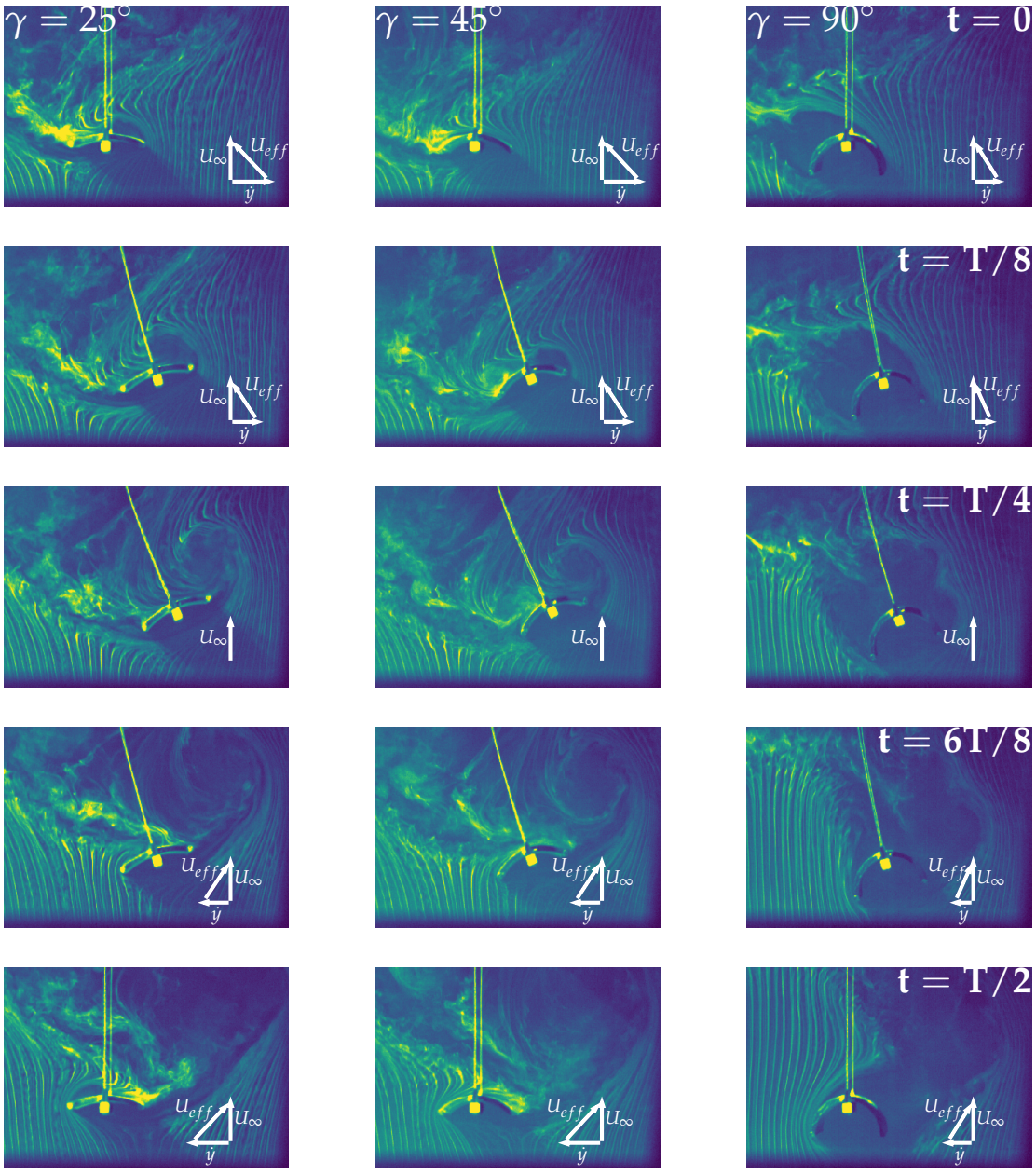

Figure 4.15: Flow visualisations with different curvatures at five different time instances across a half-oscillation cycle. Reduced velocity $U^* = 8.4$. The colourmap represents the pixel intensity values obtained from the monochrome Phantom high speed camera.

4.5 Comparison to the Square-Prism

To form a comparison to geometries which have previously been investigated in the literature, experiments were also performed with the square-prism geometry. A square-prism of span equal to that of the curved-blades and with width and height equal to the chord length was constructed and mounted into the wind tunnel identically to as was performed in the characterisation of the curved-blades, with the same cantilever beams and mounting structure. The mass was also fixed to that of the curved-blade geometries to ensure the oscillation frequency was consistent. The results obtained with the square-prism are presented in Figure 4.16, including both the coefficient of performance vs tip speed ratio amplitude and flow visualisations at the maximum velocity and maximum displacement positions as indicated by $t = 0$ and $t = \frac{T}{4}$ respectively in subplots (b) and (c).

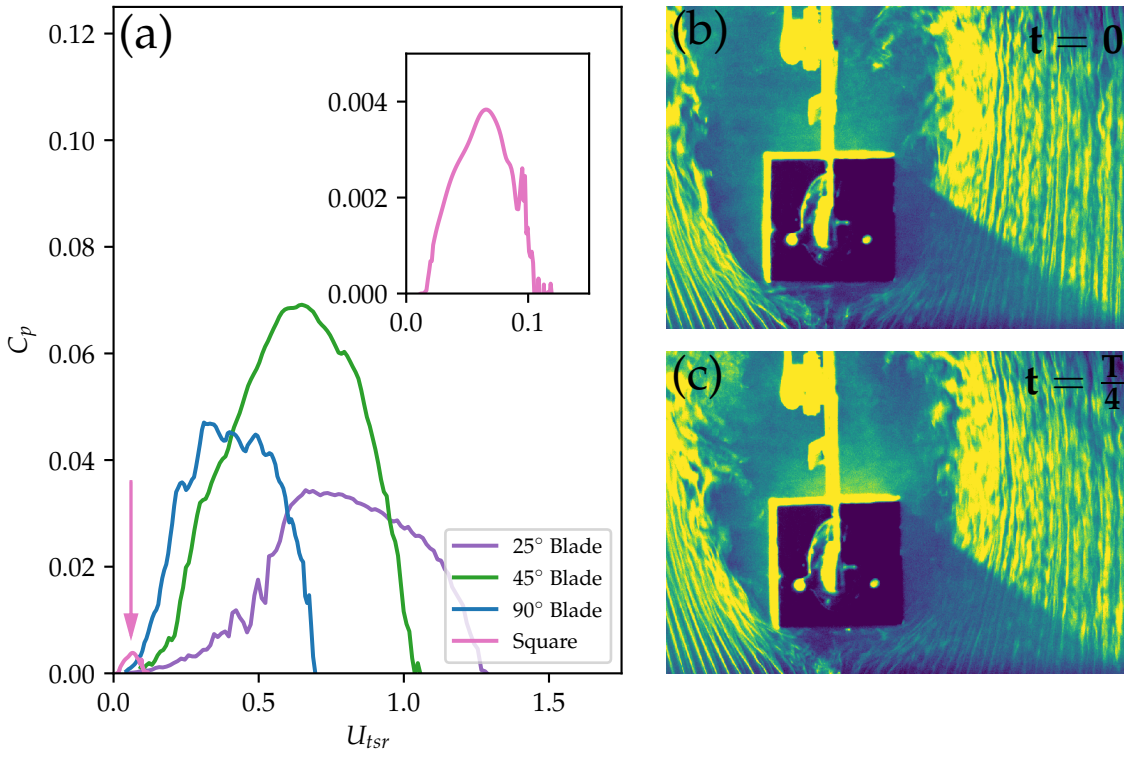

Figure 4.16: Comparison of curved-blade and square-prism performance and square-prism flow visualisations. Subplot (a) illustrates the coefficient of performance predicted for the square-prism. Subplot (b) shows a flow visualisation of the square-prism at its zero displacement, hence maximum velocity position, while a flow visualisation at the maximum displacement position is shown in subplot (c). Reduced velocity $U^* = 8.4$.

The square-prism geometry was considerably outperformed by curved-blades of all

considered curvatures. The flow visualisations demonstrate the flow to separate at both front edges of the square without reattachment on the sides parallel to the freestream flow direction the maximum velocity and maximum displacement positions. The flow pattern in the case of the square-prism is hence highly separated and therefore differs fundamentally from the attached flows observed with the 35°, 45° and 65° half-arc angle curved-blade geometries.

4.6 Summary

In this chapter the effect of the curved-blade curvature on its energy harvesting performance has been investigated by application of the method developed in Chapter 3. The geometries with curvatures in the medium range, corresponding to half-arc angles of 35°, 45° and 65°, are found to considerably outperform the 25° and 90° geometries. Flow visualisations have demonstrated that in these cases, the flow becomes attached at the maximum velocity position. The higher performance in these cases can hence be attributed to the attachment of the flow to the rear surface of the blade when the velocity is close to its maxima. This mechanism has also been demonstrated by observing flow patterns with the same geometry but at different oscillation amplitudes, with the performance of the 45° geometry observed to be considerable greater at oscillation amplitudes at which the flow becomes attached.

A maximum coefficient of performance of 0.08 was obtained with the 65° half-arc angle geometry. The optimal operating amplitude of a wind energy harvester is defined by the amplitude of the coefficient of performance maximum. For the curved-blades investigated, the tip speed ratio at the coefficient of performance maximum ranged from 0.32 to 0.74.

By consideration of Kelvin's circulation theorem, the flow visualisations across an oscillation cycle in which the flow becomes attached have suggested that the leading edge vortex forms to balance the falling bound circulation as the curved-blade decelerates, while it is periodically shed every half-oscillation. The formation of small vortices in the wake has been clearly observed in some cases, which provides a mechanism to balance the growth of the bound circulation during each half-period.

For the purpose of benchmarking, experiments were also performed with a square-prism geometry. This was chosen as a comparator as it has been widely investigated in previous studies [108, 111, 48] and is considered to be a high performing geometry. The curved-blade was found to provide an order of magnitude higher performance than the square-prism within the considered range of reduced velocities, while the flow around the square-prism has been shown to be highly separated in nature.

5

Conclusions

5.1 Conclusions

In this thesis an alternative geometry for a galloping energy harvester has been presented, which was initially inspired by the trembling of Aspen leaves in barely noticeable winds. The geometry, known as the curved-blade, has been investigated in the context of galloping energy harvesting and insight has been gained into the underlying fluid mechanisms behind its oscillations. The work is broadly partitioned by the structure of the chapters. In Chapter 2 an initial analysis of a galloping oscillator with the curved-blade geometry was set out with the aim of developing an understanding of the mechanism by which its oscillations occur. To aid in the later experimental analysis of the influence of the curved-blade geometric parameters on the harvesting performance, a method was developed which enabled the characterisation of performance from the free oscillation transient. This method was described in Chapter 3. Finally, the application of the developed method to the investigation of the influence of the blade curvature on its performance was laid out in Chapter 4.

The method developed in Chapter 3 allowed the performance of different galloping geometries to be characterised without the requirement of implementing a harvesting mechanism. The simulations demonstrated the region in which the method could be applied accurately to be relatively wide with the main requirement being the existence of timescale separation between the conservative and nonconservative forces acting on a system. Although simple, the concept of characterising energy transfer from the fluid by the

measurement of the growth of conservative energy within a system has many applications outside of the narrow field of galloping energy harvesters.

The requirement of timescale separation for the application of the method described in Chapter 3 is limiting when the approach is applied to devices operating in much denser fluids, such as water. In these cases the transient becomes short, containing only a few oscillation cycles, and can be far from sinusoidal in nature. However, the influence of the fluid forces on the short timescale trajectory provides another opportunity for the extraction of the fluid forces in these cases. If the acceleration of the tip geometry can be accurately measured and the force produced by the cantilever beam characterised, the time dependant fluid forces can be determined. Developing and demonstrating this approach would be advantageous as the study of the curved-blade galloping oscillator in denser fluids would not only illustrate that it could be used to harvest energy in a wider range of applications, but would also enable mass ratio regimes which are practically unobtainable in air to be investigated.

Motion tracking was utilised extensively in chapters 2 and 4 for the measurement of the dynamics of the galloping oscillator. This differed from most other experimental studies, where the measurement of displacement with a laser vibrometer is more common [34, 6]. Aside from the difficulties associated with the much larger volume of data captured when recording images and the subsequent limits on sampling rates, motion tracking allowed the kinematics of the galloping oscillator to be extracted in a way that would not be possible when measuring the displacement of the tip geometry along a single axis. These kinematics demonstrated the maximum slope angle of the cantilever beam to maintain close to sinusoidal behaviour at much greater oscillation amplitudes than the linear displacement of the tip geometry. This observation has important consequences for the comparison of single degree of freedom models for galloping oscillators to experimental results, as nonlinearity caused by the motion of the tip geometry along a curved path, rather than a single axis as assumed in many modelling approaches, can cause significant differences between model and experiment.

The observation of flow attachment has formed a key aspect of the analysis in Chapter 2 and 4. The discovery of two distinct branches of oscillations separated significantly in amplitude in the wind tunnel experiment described in Chapter 2 was suggestive of the existence of two different mechanisms of fluid-structure interaction, one corresponding to each branch. This suggestion was confirmed by flow visualisations as the flow was found to become attached to the rear face of the curved-blade when the velocity was near its maximum in the case of the high amplitude branch, however remained detached when in the low amplitude branch. The aerodynamic performance and subsequently the power transferred from the flow was enhanced in the attached regime, which can be considered as similar to

the attached flow found around aerofoils at low angle of attack. In Chapter 4 a similar observation is made, but rather than comparing different branches of oscillations, geometries with curvatures that enabled the flow to become attached were found to have considerably improved performances. Further to this, evaluating the performance of a single curvature over a range of oscillation amplitudes demonstrated that the occurrence of flow attachment again coincided with an increase in the characterised performance. These observations are illustrative of the potential for a new direction in the design of galloping geometries, which differs significantly from the bluff bodies which have dominated previous investigations.

The flow field developed around the curved-blade was by no means a steady flow phenomenon as demonstrated by the visualisation of the cyclic formation and shedding of a leading edge vortex in Chapter 4. Some interpretation of the unsteady flow phenomena has been made with the application of Kelvin's circulation theorem, suggesting that the formation of the leading edge vortex arises to balance the falling bound vorticity around the curved-blade as it decelerates from its maximum velocity position, while the growth of the bound vorticity during the acceleration of the curved-blade was balanced by the shedding of smaller vortices into the curved-blade wake.

5.2 Future Work

The observation of the potential for significantly improved harvesting performance by designing galloping geometries to promote flow attachment underpins a large proportion of the suggestions for future work which can be taken from this thesis. The study of how geometries can be designed or modified to promote flow attachment has a broad and long history with relation to the development of aerofoils. Hence, for devices designed to produce energy at transition Reynolds numbers or greater, well developed structures such as vortex generators [15] and other boundary layer control technologies [61] may be applicable to improve the harvesting performance.

Leading edge vortices have been shown to provide a sizeable lift enhancement in many low Reynolds number flows, including the flapping of insect wings and small birds [31, 72], and also at higher Reynolds numbers on the sails of yachts [10]. Although the cyclic formation and shedding of a leading edge vortex has been observed in the flow visualisations, how it relates to the harvesting performance still requires further investigation. Quantitative particle image velocimetry measurements of the flow field with high enough accuracy for force estimation by a method such as that developed by Li and Wu [62] may demonstrate whether this unsteady flow structure can provide a performance enhancement and how best to design geometries to benefit from it.

In almost all considerations of galloping energy harvesters, the flow field is assumed

to be close to two-dimensional with devices being constructed with relatively high aspect ratios. Yet, low aspect ratio geometries have been shown to have preferable stall characteristics at high angles of attack [95, 64], making them well suited for galloping energy harvesters by providing attached flow at lower oscillation amplitudes. A useful avenue for further work may hence be to explore different low aspect ratio geometries and compare their performances to comparable high aspect ratio geometries.

Much of the work on galloping energy harvesters, including that presented in this thesis, corresponds to the oscillation of weakly nonlinear structures where oscillations are close to sinusoidal and with only one active degree of freedom. The consequent kinematics of the galloping geometry may hence be far from optimal, especially if a system is to be designed to promote flow attachment or the favourable formation of a leading edge vortex. Investigating the influence of alternative oscillatory kinematics on the performance of galloping energy harvesters could therefore form a fruitful aspect of their development.

Tip geometries investigated for galloping energy harvesters are typically considered to be rigid. However, incorporating flexible materials into designs may result in improved performance by similar mechanisms to as has been observed with flapping aerofoils [45, 74]. In the case of the curved-blade geometry, flexibility may be able to passively adjust the shape of the blade cross section during an oscillation and improve the aerodynamic performance by pushing the separation point closer to the trailing edge, hence resulting in improved harvesting efficiencies. The dynamics of the blade deformation will likely depend on the regime in which the harvester operates. In a case when the fluid forces are significant in relation to the inertial forces, the pressure distribution generated by the flow will play a key role in defining the deformation during an oscillation cycle. However, in a regime in which the inertial forces on the blade are much greater than those generated by the fluid flow, these will dominate the dynamics. Considering different flexible designs for these two distinct regimes could yield significant improvements to the efficiencies of galloping energy harvesters.

During the process of undertaking the work presented in this thesis, initial results were obtained investigating the interaction of multiple curved-blade galloping oscillators. The results demonstrated that phase locking synchronisation can occur between two devices when their natural frequencies are close and the interaction can have a considerable influence on the oscillation amplitudes of the individual devices. However, the flow phenomena underlying these interactions were not uncovered and hence form part of the suggested future work.

In applications where the curved-blade operates in water and is in close proximity to the free surface, there can be a strong interaction between the flow field around the blade and the free surface. Initial experiments performed by the author and collaborators from the

University of Hokkaido with the direction of motion of the blade aligned to the gravity vector have shown this interaction to result in significant free surface deformation and an altered blade trajectory, however it is unclear whether it is beneficial to the operation of the device as an energy harvester. Further consideration of this interaction may yield opportunities of improved performance or demonstrate the minimum proximity that a prototype device should be positioned from a free surface.

References

[1] Abdelkefi, A. (2016). Aeroelastic energy harvesting: A review. *International Journal of Engineering Science*, 100:112–135.

[2] Abdelkefi, A., Hajj, M. R., and Nayfeh, a. H. (2013). Piezoelectric energy harvesting from transverse galloping of bluff bodies. *Smart Materials and Structures*, 22(1):015014.

[3] Abdelkefi, A., Nayfeh, A. H., and Hajj, M. R. (2012a). Design of piezoaeroelastic energy harvesters. *Nonlinear Dynamics*, 68(4):519–530.

[4] Abdelkefi, A., Nayfeh, A. H., and Hajj, M. R. (2012b). Modeling and analysis of piezoaeroelastic energy harvesters. *Nonlinear Dynamics*, 67(2):925–939.

[5] Abdelkefi, A., Yan, Z., and Hajj, M. R. (2014). Performance analysis of galloping-based piezoaeroelastic energy harvesters with different cross-section geometries. *Journal of Intelligent Material Systems and Structures*, 25(2):246–256.

[6] Alhadidi, A. H., Alhussein, H., and Daqaq, M. F. (2020). Improving the sensitivity of galloping energy harvesters to flow fluctuations. *Applied Physics Letters*, 116(26):2–7.

[7] Alhadidi, A. H. and Daqaq, M. F. (2016). A broadband bi-stable flow energy harvester based on the wake-galloping phenomenon. *Applied Physics Letters*, 109(3):3–8.

[8] Alonso, G., Meseguer, J., and Pérez-Grande, I. (2007). Galloping stability of triangular cross-sectional bodies: A systematic approach. *Journal of Wind Engineering and Industrial Aerodynamics*, 95(9-11):928–940.

[9] Anton, S. R. and Inman, D. J. (2008). Vibration energy harvesting for unmanned aerial vehicles. In Ahmadian, M., editor, *Active and Passive Smart Structures and Integrated Systems 2008*, volume 6928, pages 621–632. International Society for Optics and Photonics, SPIE.

[10] Arredondo-Galeana, A. and Viola, I. M. (2018). The leading-edge vortex of yacht sails. *Ocean Engineering*, 159(February):552–562.

[11] Bacon, D. and Stephens, R. (1990). Dynamic Similarity. In Kundu, P. K., Cohen, I. M., and Dowling, D. R., editors, *Fluid Mechanics (Sixth Edition)*, chapter 8, pages 279–294. Academic Press, Boston, sixth edit edition.

[12] Bae, J. S. and Inman, D. J. (2013). Aeroelastic characteristics of linear and nonlinear piezo-aeroelastic energy harvester. *Journal of Intelligent Material Systems and Structures*, 25(0):401–416.

[13] Barrero-Gil, A., Alonso, G., and Sanz-Andres, A. (2010). Energy harvesting from transverse galloping. *Journal of Sound and Vibration*, 329(14):2873–2883.

[14] Barrero-Gil, A., Pindado, S., and Avila, S. (2012). Extracting energy from Vortex-Induced Vibrations: A parametric study. *Applied Mathematical Modelling*, 36(7):3153–3160.

[15] Barrett, R. and Farokhi, S. (1996). Subsonic aerodynamics and performance of a smart vortex generator system. *Journal of Aircraft*, 33(2):393–398.

[16] Bibo, A. and Daqaq, M. F. (2014). On the optimal performance and universal design curves of galloping energy harvesters. *Applied Physics Letters*, 104(2).

[17] BP (2019a). BP Energy Outlook 2019. Technical report.

[18] BP (2019b). BP Statistical Review of World Energy 2019. Technical report.

[19] Bruun, H. H. (1996). Hot-Wire Anemometry: Principles and Signal Analysis. *Measurement Science and Technology*, 7(10).

[20] Bryant, M. and Garcia, E. (2009). Development of an aeroelastic vibration power harvester. *Active and Passive Smart Structures and Integrated Systems*, 7288:728812–728812–10.

[21] Chadha, J. and Jaster, W. (1975). Influence of turbulence on the galloping instability of iced conductors. *IEEE Transactions on Power Apparatus and Systems*, 94(5):1489–1499.

[22] Cottrill, A. L., Liu, A. T., Kunai, Y., Koman, V. B., Kaplan, A., Mahajan, S. G., Liu, P., Toland, A. R., and Strano, M. S. (2018). Ultra-high thermal effusivity materials for resonant ambient thermal energy harvesting. *Nature Communications*, 9(1):1–11.

[23] Cunningham, H. J., Batina, J. T., and Bennett, R. M. (1988). Modern wing flutter analysis by computational fluid dynamics methods. *Journal of Aircraft*, 25(10):962–968.

[24] Dai, H. L., Abdelkefi, A., Javed, U., and Wang, L. (2015). Modeling and performance of electromagnetic energy harvesting from galloping oscillations. *Smart Materials and Structures*, 24(4).

[25] Dai, H. L., Abdelkefi, A., and Wang, L. (2014). Piezoelectric energy harvesting from concurrent vortex-induced vibrations and base excitations. *Nonlinear Dynamics*, 77(3):967–981.

[26] de Langre, E. (2008). Effects of wind on plants. *Annual Review of Fluid Mechanics*, 40:141–168.

[27] Den Hartog, J. P. (1956). *Mechanical Vibrations*. McGraw-Hill, New York, 4th edition.

[28] Deng, X., Schenato, L., and Sastry, S. S. (2006). Flapping flight for biomimetic robotic insects: Part II - Flight control design. *IEEE Transactions on Robotics*, 22(4):789–803.

[29] Eckersley-Carr, F. M. (2013). Energy Harvesting from an Oscillating Leaf. Technical report.

[30] Eldredge, J. D. and Jones, A. R. (2019). Leading-Edge Vortices: Mechanics and Modeling. *Annual Review of Fluid Mechanics*, 51(1):75–104.

[31] Ellington, C. P., den Berg, C. V., and Willmott, A. P. (1990). Leading-edge vortices in insect flight. *Nature*, 384(December):626–630.

[32] Erturk, A., Bilgen, O., Fontenille, M., and Inman, D. J. (2008). Piezoelectric energy harvesting from macro-fiber composites with an application to morphing-wing aircrafts. In *19th International Conference on Adaptive Structures and Technologies 2008, ICAST 2008*, pages 339–359.

[33] Erturk, A., Vieira, W. G. R., De Marqui, C., and Inman, D. J. (2011). On the energy harvesting potential of piezoaeroelastic systems. 184103(May 2010).

[34] Ewere, F., Wang, G., and Cain, B. (2014). Experimental investigation of galloping piezoelectric energy harvesters with square bluff bodies.

[35] Facchinetti, M. L., de Langre, E., and Biolley, F. (2004). Coupling of structure and wake oscillators in vortex-induced vibrations. *Journal of Fluids and Structures*, 19(2):123–140.

[36] Farokhi, H., Gholipour, A., and Ghayesh, M. H. (2020). Efficient Broadband Vibration Energy Harvesting Using Multiple Piezoelectric Bimorphs. *Journal of Applied Mechanics*, 87(4):1–12.

[37] Farshidianfar, A. and Dolatabadi, N. (2013). Modified higher-order wake oscillator model for vortex-induced vibration of circular cylinders. *Acta Mechanica*, 224(7):1441–1456.

[38] Feldman, M. (2011). *Hilbert transform applications in mechanical vibration*. John Wiley & Sons.

[39] Gaskell, J. (2017). Increasing the Power Output of an Aspen Leaf Wind Energy Harvester by Altering its Mechanical Properties. Technical report.

[40] Gholikhani, M., Roshani, H., Dessouky, S., and Papagiannakis, A. T. (2020). A critical review of roadway energy harvesting technologies. *Applied Energy*, 261(July 2019):114388.

[41] Halim, M. A., Rantz, R., Zhang, Q., Gu, L., Yang, K., and Roundy, S. (2018). An electromagnetic rotational energy harvester using sprung eccentric rotor, driven by pseudo-walking motion. *Applied Energy*, 217(February):66–74.

[42] Hamlehdar, M., Kasaeian, A., and Safaei, M. R. (2019). Energy harvesting from fluid flow using piezoelectrics: A critical review. *Renewable Energy*, 143:1826–1838.

[43] Harb, Y. (2018). Wind Energy Harvesting: Synchronization of two identical oscillating harvesters. Technical report.

[44] He, X., Yang, X., and Jiang, S. (2018). Enhancement of wind energy harvesting by interaction between vortex-induced vibration and galloping. 033901.

[45] Heathcote, S. and Gursul, I. (2007). Flexible flapping airfoil propulsion at low reynolds numbers. *AIAA Journal*, 45(5):1066–1079.

[46] Helfman Cohen, Y. and Reich, Y. (2016). *Biomimetic Design Method for Innovation and Sustainability*.

[47] Hover, F. S., Techet, A. H., and Triantafyllou, M. S. (1998). Forces on oscillating uniform and tapered cylinders in crossflow. *Journal of Fluid Mechanics*, 363:97–114.

[48] Hu, G., Tse, K. T., and Kwok, K. C. S. (2016). Enhanced performance of wind energy harvester by aerodynamic treatment of a square prism. *Applied Physics Letters*, 108(12).

[49] Hu, G., Tse, K. T., Wei, M., Naseer, R., Abdelkefi, A., and Kwok, K. C. (2018). Experimental investigation on the efficiency of circular cylinder-based wind energy harvester with different rod-shaped attachments. *Applied Energy*, 226(June):682–689.

[50] Huynh, B. H. and Tjahjowidodo, T. (2017). Experimental chaotic quantification in bistable vortex induced vibration systems. *Mechanical Systems and Signal Processing*, 85(September 2016):1005–1019.

[51] Isaev, S. A., Baranov, P. A., Zhukova, Y. V., Kalinin, E. I., and Miau, J. J. (2016a). Verification of the Shear-Stress Transfer Model and its Modifications in the Calculation of a Turbulent Flow Around a Semicircular Airfoil with a Zero Angle of Attack. *Journal of Engineering Physics and Thermophysics*, 89(1):73–89.

[52] Isaev, S. I., Baranov, P. A., Sudakov, A. G., and Usachev, A. E. (2016b). Control of the Periodic Turbulent Flow over a Semicircular Airfoil with the Use of the Slot Suction of the Air from a Circular Vortex Cell at Small Angles of Attack. *Journal of Engineering Physics and Thermophysics*, 89(6):1500–1504.

[53] Jafferis, N. T., Helbling, E. F., Karpelson, M., and Wood, R. J. (2019). Untethered flight of an insect-sized flapping-wing microscale aerial vehicle. *Nature*, 570(7762):491–495.

[54] Javed, U. and Abdelkefi, A. (2017). Impacts of the aerodynamic force representation on the stability and performance of a galloping-based energy harvester. *Journal of Sound and Vibration*, 400(April):213–226.

[55] Jia, H., Cheng, X., Zhu, J., Li, Z., and Guo, J. (2018). Mathematical and experimental analysis on solar thermal energy harvesting performance of the textile-based solar thermal energy collector. *Renewable Energy*, 129:553–560.

[56] Jones, A. R. and Babinsky, H. (2010). Unsteady lift generation on rotating wings at low reynolds numbers. *Journal of Aircraft*, 47(3):1013–1021.

[57] Kalmikov, A. (2017). Wind Power Fundamentals. In *Wind Energy Engineering: A Handbook for Onshore and Offshore Wind Turbines*, pages 17–24. Elsevier Inc.

[58] Katz, J. and Plotkin, A. (2001). *Low-speed aerodynamics*, volume 13. Cambridge university press.

[59] Kishore, R. A. and Priya, S. (2018). A Review on low-grade thermal energy harvesting: Materials, methods and devices. *Materials*, 11(8).

[60] Kuznetsov, Y. A. (1998). *Elements of Applied Bifurcation Theory*. Springer.

[61] Leschziner, M. A. and Lardeau, S. (2011). Simulation of slot and round synthetic jets in the context of boundary-layer separation control. *Philosophical Transactions of the Royal Society A: Mathematical, Physical and Engineering Sciences*, 369(1940):1495–1512.

[62] Li, J. and Wu, Z. N. (2018). Vortex force map method for viscous flows of general airfoils. *Journal of Fluid Mechanics*, 836:145–166.

[63] Li, J., Yu, H., Wong, S. M., Zhang, G., Sun, X., Lo, P. G. Q., and Kwong, D. L. (2009). Si nanopillar array optimization on Si thin films for solar energy harvesting. *Applied Physics Letters*, 95(3).

[64] Liu, Y. C. and Hsiao, F. B. (2012). Aerodynamic investigations of low-aspect-ratio thin plate wings at low reynolds numbers. *Journal of Mechanics*, 28(1):77–89.

[65] Luo, S. C., Chew, Y. T., Lee, T. S., and Yazdani, M. G. (1998). Stability to translational galloping vibration of cylinders at different mean angles of attack. *Journal of Sound Vibration*, 215:1183–1194.

[66] Luo, S. C., Chew, Y. T., and Ng, Y. T. (2003). Hysteresis phenomenon in the galloping oscillation of a square cylinder. *Journal of Fluids and Structures*, 18(1):103–118.

[67] Mackowski, A. W. and Williamson, C. H. (2013). An experimental investigation of vortex-induced vibration with nonlinear restoring forces. *Physics of Fluids*, 25(8).

[68] Mannini, C., Marra, A. M., Massai, T., and Bartoli, G. (2016). Interference of vortex-induced vibration and transverse galloping for a rectangular cylinder. *Journal of Fluids and Structures*, 66:403–423.

[69] Mannini, C., Massai, T., Maria Marra, A., and Bartoli, G. (2017). Interference of Vortex-Induced Vibration and Galloping: Experiments and Mathematical Modelling. In *Procedia Engineering*, volume 199, pages 3133–3138.

[70] Massey, T. (2014). Harvesting Energy from an Underwater Array of Fluttering Plates. Technical report.

[71] Matsumoto, M., Yagi, T., Hatsuda, H., Shima, T., Tanaka, M., and Naito, H. (2010). Dry galloping characteristics and its mechanism of inclined/yawed cables. *Journal of Wind Engineering and Industrial Aerodynamics*, 98(6-7):317–327.

[72] Muijres, F. T., Johansson, L. C., Barfield, R., Wolf, M., Spedding, G. R., and Hedenström, A. (2008). Leading-Edge Vortex Improves Lift in. *Science*, 319(February):1250–1253.

[73] Murdock, J. A. (1999). *Perturbations: theory and methods*. SIAM.

[74] Nakata, T., Liu, H., Tanaka, Y., Nishihashi, N., Wang, X., and Sato, A. (2011). Aerodynamics of a bio-inspired flexible flapping-wing micro air vehicle. *Bioinspiration and Biomimetics*, 6(4).

[75] Novak, M. and Tanaka, H. (1974). Effect of turbulence on galloping instability. *Journal of the engineering mechanics division*, 100(1):27–47.

[76] Novak, M., Tanaka, H., and Davenport, A. G. (1978). Vibration of towers due to galloping of iced cables. *Journal of the Engineering Mechanics Division*, 104(2):457–473.

[77] Nozariasbmarz, A., Collins, H., Dsouza, K., Polash, M. H., Hosseini, M., Hyland, M., Liu, J., Malhotra, A., Ortiz, F. M., Mohaddes, F., Ramesh, V. P., Sargolzaeiaval, Y., Snouwaert, N., Özturk, M. C., and Vashaee, D. (2020). Review of wearable thermoelectric energy harvesting: From body temperature to electronic systems. *Applied Energy*, 258(October 2019):114069.

[78] Oeffner, J. and Lauder, G. V. (2012). The hydrodynamic function of shark skin and two biomimetic applications. *Journal of Experimental Biology*, 215(5):785–795.

[79] Parkinson, G. V. and Smith, J. D. (1964). The Square Prism as an Aeroelastic Nonlinear Oscillator. *Quart. Jonrn. Mech. and Applied Math.*, XV(3).

[80] Parkinson, G. V. and Sullivan, P. P. (1979). Galloping response of towers. *Journal of Wind Engineering and Industrial Aerodynamics*, 4(3):253–260.

[81] Peters, D. A., Karunamoorthy, S., and Cao, W.-M. (1995). Finite state induced flow models. I - Two-dimensional thin airfoil. *Journal of Aircraft*, 32(2):313–322.

[82] Rostami, A. B. and Armandei, M. (2017). Renewable energy harvesting by vortex-induced motions: Review and benchmarking of technologies. *Renewable and Sustainable Energy Reviews*, 70(November):193–214.

[83] Seyed-aghazadeh, B. and Carlson, D. W. (2017). Vortex-induced vibration and galloping of prisms with triangular cross-sections. pages 590–618.

[84] Shin, Y. H., Jung, I., Noh, M. S., Kim, J. H., Choi, J. Y., Kim, S., and Kang, C. Y. (2018). Piezoelectric polymer-based roadway energy harvesting via displacement amplification module. *Applied Energy*, 216(November 2017):741–750.

[85] Silva-Leon, J., Cioncolini, A., Nabawy, M. R., Revell, A., and Kennaugh, A. (2019). Simultaneous wind and solar energy harvesting with inverted flags. *Applied Energy*, 239(February):846–858.

[86] Smits, A. J. (2012). *Flow visualization: techniques and examples*. World Scientific.

[87] Strogatz, S. H. (2018). *Nonlinear Dynamics and Chaos with Student Solutions Manual*. CRC Press.

[88] Sun, W., Jo, S., and Seok, J. (2019). Development of the optimal bluff body for wind energy harvesting using the synergetic effect of coupled vortex induced vibration and galloping phenomena. *International Journal of Mechanical Sciences*, 156(November 2018):435–445.

[89] Tadrist, L., Saudreau, M., Hémon, P., Amandolese, X., Marquier, A., Leclercq, T., and de Langre, E. (2018). Foliage motion under wind, from leaf flutter to branch buffeting. *Journal of the Royal Society Interface*, 15(142).

[90] Tan, T. and Yan, Z. (2016). Analytical solution and optimal design for galloping-based piezoelectric energy harvesters. *Applied Physics Letters*, 109(25).

[91] Theodorsen, T. (1949). naca-report-496 General Theory of Aerodynamic Instability and the Mechanism of Flutter.

[92] Theodorsen, T. and Garrick, I. E. (1940). *Mechanism of flutter: a theoretical and experimental investigation of the flutter problem.* US Government Printing Office.

[93] Thielen, M., Sigrist, L., Magno, M., Hierold, C., and Benini, L. (2017). Human body heat for powering wearable devices: From thermal energy to application. *Energy Conversion and Management*, 131:44–54.

[94] Tong, W. P. Q., Muhammad Ramadan, B. M., and Logenthiran, T. (2018). Design and Simulation of a Piezoelectric Cantilever Beam for Mechanical Vibration Energy Harvesting. *International Conference on Innovative Smart Grid Technologies, ISGT Asia 2018*, pages 1245–1250.

[95] Torres, G. E. and Mueller, T. J. (2004). Low-aspect-ratio wing aerodynamics at low reynolds numbers. *AIAA Journal*, 42(5):865–873.

[96] Tu, J., Zhou, D., Bao, Y., Han, Z., and Li, R. (2014). Flow characteristics and flow-induced forces of a stationary and rotating triangular cylinder with different incidence angles at low Reynolds numbers. *Journal of Fluids and Structures*, 45(800):107–123.

[97] Tucker Harvey, S., Khovanov, I. A., and Denissenko, P. (2019). A galloping energy harvester with flow attachment. *Applied Physics Letters*, 114(10).

[98] Wang, N., Zou, J., Yang, Y., Li, X., Guo, Y., Jiang, C., Jia, X., and Cao, X. (2019). Kelp-inspired biomimetic triboelectric nanogenerator boosts wave energy harvesting. *Nano Energy*, 55(November 2018):541–547.

[99] Wei, C. and Jing, X. (2017). A comprehensive review on vibration energy harvesting: Modelling and realization. *Renewable and Sustainable Energy Reviews*, 74(November 2016):1–18.

[100] Wen, L., Weaver, J. C., and Lauder, G. V. (2014). Biomimetic shark skin: Design, fabrication and hydrodynamic function. *Journal of Experimental Biology*, 217(10):1656–1666.

[101] Williamson, C. and Govardhan, R. (2004). Vortex-Induced Vibrations. *Annual Review of Fluid Mechanics*, 36(1):413–455.

[102] Williamson, C. H. and Roshko, A. (1988). Vortex formation in the wake of an oscillating cylinder. *Journal of Fluids and Structures*, 2(4):355–381.

[103] Wright, J. R. and Cooper, J. E. (2015). *Introduction to Aircraft Aeroelasticity and Loads: Second Edition*.

[104] Wu, J., Yang, S. C., Shu, C., Zhao, N., and Yan, W. W. (2015). Ground effect on the power extraction performance of a flapping wing biomimetic energy generator. *Journal of Fluids and Structures*, 54:247–262.

[105] Wu, Y., Li, D., Xiang, J., and Da Ronch, A. (2016). A modified airfoil-based piezoaeroelastic energy harvester with double plunge degrees of freedom. *Theoretical and Applied Mechanics Letters*, 6(5):244–247.

[106] Xiao, Q. and Zhu, Q. (2014). A review on flow energy harvesters based on flapping foils. *Journal of Fluids and Structures*, 46:174–191.

[107] Yan, Z. and Abdelkefi, A. (2014). Nonlinear characterization of concurrent energy harvesting from galloping and base excitations. *Nonlinear Dynamics*, pages 1171–1189.

[108] Yang, Y., Zhao, L., and Tang, L. (2013). Comparative study of tip cross-sections for efficient galloping energy harvesting. *Applied Physics Letters*, 102(6).

[109] Yates Jr, E. C. (1966). Modified-strip-analysis method for predicting wing flutter at subsonic to hypersonic speeds. *Journal of Aircraft*, 3(1):25–29.

[110] Zabek, D. and Morini, F. (2019). Solid state generators and energy harvesters for waste heat recovery and thermal energy harvesting. *Thermal Science and Engineering Progress*, 9(November 2018):235–247.

[111] Zhao, L., Tang, L., and Yang, Y. (2013). Comparison of modeling methods and parametric study for a piezoelectric wind energy harvester. *Smart Materials and Structures*, 22(12).

[112] Zhao, L. and Yang, Y. (2015). Analytical solutions for galloping-based piezoelectric energy harvesters with various interfacing circuits. *Smart Materials and Structures*, 24(7).